UNIVERSITY OF CALIFORNIA
RIVERSIDE

The Evolution of Stellar Velocity Dispersion in Galaxy Mergers

A Dissertation submitted in partial satisfaction
of the requirements for the degree of

Doctor of Philosophy

in

Physics

by

Nathaniel Roland Stickley

December 2013

Dissertation Committee:
Dr. Gabriela Canalizo, Chairperson
Dr. Gillian Wilson
Dr. José Wudka

The Dissertation of Nathaniel Roland Stickley is approved:

_____

_____

_____

Committee Chairperson

University of California, Riverside

Acknowledgements

I am grateful to everyone who made this Ph.D. dissertation possible. A comprehensive list of people who played an essential role in the process is not feasible, however, a few people immediately come to mind.

My advisor, Gabriela Canalizo, provided me with a tremendous degree of freedom and many opportunities over the years. She also nominated me for several awards and provided me with a salary that allowed me to focus on research after my grant funds were exhausted.

I thank my wife, Melissa, for supporting me through the very stressful final year of my dissertation research. I thank my son, Lev for providing me with extra motivation and brightening the final months of my research with his wonderful smile and contagious laugh. Without my amazing mother, I would not have been capable of pursuing an advanced degree and without the encouragement of my sister, Svonne, I may have never attended a university.

Additionally, Gillian Wilson provided me with the computer hardware that made this research possible. The research also benefited from feedback and suggestions provided by Desika Narayanan, Mike Boylan-Kolchin, Jong-Hak Woo, Barry Rothberg, and Joshua Barnes.

This work used the Extreme Science and Engineering Discovery Environment (XSEDE), which is supported by National Science Foundation grant number OCI-1053575. Financial support for this work was provided by NASA through a grant from the Space Telescope Science Institute (Program numbers AR-12626 and GO-11557), which is operated by the Association of Universities for Research in Astronomy, Incorporated, under NASA contract NAS5-26555. Additional support was provided by the National Science Foundation, under grant number AST-0507450

The text of this dissertation, in part, is a reprint of the material as it appears a journal article entitled *The Evolution of Stellar Velocity Dispersion During Dissipationless Galaxy Mergers*, which appeared in volume 747 (page 33) of The Astrophysical Journal, February 13th, 2012. The co-author (Gabriela Canalizo) listed in that publication directed and supervised the research which forms the basis for this dissertation.

ABSTRACT OF THE DISSERTATION

The Evolution of Stellar Velocity Dispersion in Galaxy Mergers

by

Nathaniel Roland Stickley

Doctor of Philosophy, Graduate Program Physics
University of California, Riverside, December 2013
Dr. Gabriela Canalizo, Chairperson

Stellar velocity dispersion is a key measurable quantity in galactic astronomy, yet its variation during galaxy mergers is not well-understood theoretically. Thus, while it is fairly common to measure velocity dispersion in galaxies that are in the process of merging, it is unclear how these measurements should be interpreted. In this dissertation, I provide a theoretical analysis of the evolution of stellar velocity dispersion during galaxy mergers. This is done using a set of numerical simulations. The temporal and directional evolution of velocity dispersion are examined in detail for a variety of merger simulations. I also examine the effects that dust attenuation and star formation have on measurements of velocity dispersion by creating detailed, Doppler broadened galaxy spectra. Velocity dispersions are measured from the synthetic spectra using the same technique that is employed for observations of real galaxies.

I find that velocity dispersion increases rapidly and significantly as two galaxies pass through one another. As galaxies recede from a collision, their velocity dispersions rapidly decrease and nearly return to their pre-collision values. Velocity dispersion increases in all directions during collisions, however the enhancement is most significant along the collision axis. After the nuclei of the progenitor systems coalesce, the velocity dispersion of the remnant system oscillates around its final equilibrium value for several dynamical timescales.

I also find that the mean velocity dispersion of young stars tends to be lower than the velocity dispersion of the galaxy as a whole; the younger populations become dynamically heated with time. In most cases, the youngest stars are found in dusty environments. Thus, dust preferentially obscures these stars, partially removing them from the flux-weighted velocity dispersion measurement. This causes flux-weighted velocity dispersion measurements to be elevated with respect to mass-weighted measurements. On the other hand, since young stellar populations are brighter, per unit mass, than older stellar populations, the low dispersion of young stars tends to weight measurements of velocity dispersion downward when the young stars are not more significantly obscured by dust than the older populations.

Contents

List of Figures

List of Tables

Chapter 1

Introduction

The line-of-sight, central stellar velocity dispersion of a galactic spheroid (hereafter simply referred to as "stellar velocity dispersion" or σ_*) is a fundamental measurable quantity in galactic astrophysics because it correlates with other observable and non-observable properties of the galaxy. The reason σ_* correlates with other observable quantities is primarily due to its relationship with the gravitational potential of the galaxy, Φ, which is a decidedly non-observable quantity. In order to fully appreciate the content of this dissertation, one must first understand the physical meaning of σ_* as well as the relationship between σ_* and Φ. Thus, a short primer is provided in Section 1.1. The details of the correlations between σ_* and observable quantities are then discussed in the introductions to Chapters 2, and 3.

1.1 A Brief Introduction to Velocity Dispersion

In 1915, James Jeans published a set of equations describing stellar dynamics in an arbitrary potential (Jeans, 1915). These equations, now known as "The Jeans Equations," can be written concisely as

$$\nu \frac{\partial \bar{u}_j}{\partial t} + \nu \bar{u}_i \frac{\partial \bar{u}_j}{\partial x_i} = -\nu \frac{\partial \Phi}{\partial x_j} - \frac{\partial (\nu \sigma_{ij}^2)}{\partial x_i}. \tag{1.1}$$

The scalar fields ν and $\bar{u}_j$ respectively represent the number density and the streaming (mean) velocity of stellar particles along direction j,

$$\nu = \int f \, \mathrm{d}^3\mathbf{u} \qquad \text{and} \qquad \bar{u}_i = \frac{1}{\nu} \int f u_i \mathrm{d}^3\mathbf{u}$$

where $\mathbf{u}$ is velocity, $f = f(\mathbf{x}, \mathbf{u}, t)$ is phase space density, x_i are spatial coordinates, and t is time. The gravitational potential is Φ and the quantity σ_{ij}^2 is defined as the covariance of (u_i, u_j),

$$\sigma_{ij}^2 \equiv \overline{(u_i - \bar{u}_i)(u_j - \bar{u}_j)}.$$

This quantity is typically referred to as the *velocity dispersion tensor*. The Jeans equations are essentially fluid equations, where the quantity $\nu\sigma_{ij}^2$ acts as the stress tensor. In this fluid analogy, σ_{ij}^2 is temperature. The projection of σ_{ij}^2 along a line of sight in the direction of $\hat{\mathbf{n}}$ can be computed via,

$$\sigma_*^2 = \hat{n}_i \sigma_{ij}^2 \hat{n}_j$$

The square root of this projection is the quantity examined in the remaining chapters of this dissertation[1]: σ_*. Since σ_{ij}^2 is analogous with temperature, the square root of its projection (σ_*) is a temperature-like quantity; systems with large values of σ_* are commonly referred to as *dynamically hot*, while systems with smaller σ_* are *dynamically cold*.

Note that, in the absence of streaming motion, the left side of Eq. (1.1) vanishes. The remaining two terms are the gravitational force per unit volume and the gradient of the stress tensor. Thus, velocity dispersion supports the system against gravitational collapse. For this reason, systems with little rotation are said to be pressure-supported. Using this observation, it is easy to see that, in the absence of streaming motion, σ_* must be larger in systems with deeper gravitational potential wells. Of course, the presence of streaming motion (i.e., bulk flow and

[1] More precisely, the quantity I examine is the square root of the mean value of σ_*^2 in a small volume of a galaxy. See Appendix A1 for more details.

rotation) can also support the system against gravitational collapse. Systems for which rotation is more significant than velocity dispersion are referred to as rotationally-supported systems.

While the Jeans equations can be solved analytically in special cases, the general solution requires the use of numerical methods. The most powerful of these methods is N-body simulation, whereby a computer is used to evolve a system of particles forward in time according to Newtonian dynamics. The quantities appearing in Eq. (1.1) are then measured from the simulation data.

1.2 σ_* in Galaxy Mergers

Stellar velocity dispersion can be measured by analyzing the spectra of galaxies (see 4.2.3 for details). Quite often, σ_* is measured in galaxies that are either in the process of merging or have clearly merged recently. It is not at all obvious how σ_* should vary with time or direction during mergers. Without an understanding of this evolution, measurements of σ_* in merging systems cannot be interpreted properly. The primary goal of the following chapters is to provide the context needed in order to interpret observations of σ_* in non-equilibrium, merging galaxies.

Unfortunately, observing the evolution of a galaxy merger on a time-scale as short as a human lifetime is hopeless, since galaxy mergers take place over millions of years. We also lack the technology needed to set up a scaled-down model of a galaxy in order to perform experiments in a laboratory. Thus, I have resorted to using virtual experiments using N-body simulations of galaxy mergers in order to study the evolution of σ_*.

In Chapter 2, I present the results of dissipationless (i.e., gas-free) mergers of very simple galaxies. In Chapter 3, I examine the more complicated (and more realistic) case of dissipative mergers that include the approximate effects of star formation. Chapter 4 focuses on examining the differences between the mass-weighted measurements of σ_* that I used in the second and third chapters and the flux-weighted measurements which are used to measure σ_* in real galaxies. Finally, Chapter 5 summarizes the most important findings.

Chapter 2

Dissipationless Galaxy Mergers

Abstract

Using N-body simulations, we studied the detailed evolution of central stellar velocity dispersion, σ_*, during dissipationless binary mergers of galaxies. Stellar velocity dispersion was measured using the common mass-weighting method as well as a flux-weighting method designed to simulate the technique used by observers. A toy model for dust attenuation was introduced in order to study the effect of dust attenuation on measurements of σ_*. We found that there are three principal stages in the evolution of σ_* in such mergers: oscillation, phase mixing, and dynamical equilibrium. During the oscillation stage, σ_* undergoes damped oscillations of increasing frequency. The oscillation stage is followed by a phase mixing stage during which the amplitude of the variations in σ_* are smaller and more chaotic than in the oscillation stage. Upon reaching dynamical equilibrium, σ_* assumes a stable value. We used our data regarding the evolution of σ_* during mergers to characterize the scatter inherent in making measurements of σ_* in non-quiescent systems. In particular, we found that σ_* does not fall below 70% nor exceed 200% of its final, quiescent value during a merger and that a random measurement of σ_* in such a system is much more likely to fall near the equilibrium value than near an extremum. Our toy model of dust attenuation suggested that dust can systematically reduce observational measurements of σ_* and increase the scatter in σ_* measurements.

2.1 Introduction

The central stellar velocity dispersion, σ_*, of a galaxy is a key observable quantity in galactic astronomy. Its importance is primarily due to the fact that σ_* can be used as a proxy for the gravitational potential when interpreted using the Jeans equations (Jeans, 1915) or the Virial theorem. In particular, there are two important galaxy scaling relations involving σ_* which are of great importance to the study of galaxy formation and evolution: the fundamental plane (FP) of elliptical galaxies (Dressler et al., 1987; Davies et al., 1987; Bender et al., 1992) and the $M_{\rm BH}$–σ_* relation (Ferrarese and Merritt, 2000; Gebhardt et al., 2000; Tremaine et al., 2002).

The FP can be expressed in various forms, most commonly $L \propto \sigma_*^{8/3}\Sigma_{\rm e}^{-3/5}$ where L is the luminosity of the galaxy and $\Sigma_{\rm e}$ is the average surface brightness within the half-light radius ($R_{\rm e}$), or alternatively $R_{\rm e} \propto \sigma_*^{1.4} I_{\rm e}^{-0.9}$ where the intensity, $I_{\rm e} = I(R_{\rm e})$. The relation is significant because it can be used to estimate the distance to an elliptical galaxy, but perhaps more importantly, because its existence yields clues to how elliptical galaxies are formed. Some studies have suggested that ongoing mergers and recent merger remnants do not fit well onto the FP relation, while other studies show that late- stage mergers (i.e., mergers containing a single nucleus) can fit near or directly on the FP relation if several complicating factors are properly taken into account (for detailed discussions, see Shier and Fischer, 1998; Bender et al., 1992; Dasyra et al., 2006; Rothberg and Joseph, 2006; Rothberg et al., 2013, and references therein). The two primary complicating factors that arise when studying the FP relation in ongoing and recent mergers are (1) the presence of dust obscuration and (2) enhanced star formation, which temporarily increases the relative abundance of O and B stars. Therefore, to gain a better understanding of the FP relation—especially in merger remnants—stellar dynamics must be disentangled from these complicating factors.

The $M_{\rm BH}$–σ_* relation is a tight relation between the mass of the central black hole ($M_{\rm BH}$) and σ_*, of the form $M_{\rm BH} \propto \sigma_*^{\alpha}$. There is evidence that black hole (BH) activity may play a role in galaxy formation and evolution, e.g., by regulating star formation through winds and outflows. To understand galaxy formation, we therefore need to understand how super-massive BHs and

galaxies co-evolve. The $M_{\rm BH}$–σ_* relation is one of the most important tools available in this endeavor. In order to fully understand the origin and implications of the $M_{\rm BH}$–σ_* relation, we must determine how the relation evolves with cosmological time (i.e., redshift). Active galactic nuclei (AGN) have become instrumental in studying the evolution of the $M_{\rm BH}$–σ_* relation with redshift because AGN hosts are the only galaxies for which we can measure $M_{\rm BH}$ in the non-local universe. Unfortunately, limiting the study of $M_{\rm BH}$–σ_* to AGN hosts may introduce a bias or significantly increase the observed scatter. This is because AGN activity has often been linked with galaxy merger activity (Canalizo and Stockton, 2001). Many modern numerical simulations that successfully reproduce present-day properties of early-type galaxies, such as the color-magnitude or the $M_{\rm BH}$–σ_* relations, presuppose that AGN activity is triggered by mergers of gas-rich galaxies (Hopkins et al., 2006; Robertson et al., 2006a,b). These gas-rich mergers also trigger star formation. Star formation, in turn, adds dust to the ISM; the dust attenuates star light. Therefore, in order to understand the $M_{\rm BH}$–σ_* relation for these objects, as well as any other objects which are not dynamically relaxed, we need a better understanding of the evolution of σ_* during the merger process as well as an understanding of how star formation and dust-attenuation may influence this measurement.

In the present chapter, we have taken the first steps toward a theoretical understanding of the evolution of σ_* *during* mergers of galaxies. We have also made initial steps toward understanding how dust-attenuation might influence the measurement of σ_*. Traditionally, simulation work involving σ_* has involved making measurements of σ_* after the merger is complete (e.g., Cox et al., 2006a; Robertson et al., 2006a,b). We only know of one study in which σ_* was plotted as a function of time *during* a merger (Johansson et al., 2009) and, in that case, the measurement interval for σ_* was 200 Myr, which (by the Nyquist sampling theorem) implies that the simulations could only capture the presence of fluctuations in σ_* having a period of 400 Myr or more. To put this in context, we note that the dynamical timescales of the systems in these simulations were less than 100 Myr. Furthermore, in simulations, σ_* is often based on the velocities of the stars falling within the half-mass radius, $r_{\rm h}$, rather than on the velocities of stars appearing in a slit placed across the center of the system, as is the case in

observational measurements of σ_* (a notable exception is the work of Cox et al. (2006a), which *did* employ a slit). The value of σ_* that is typically reported is the mean value measured along 100-250 random lines of sight; the standard deviation of σ_* over the set of viewing directions is typically not reported. Finally, to our knowledge, no simulation study has attempted to measure the effect of dust-attenuation on determinations of σ_*. The work presented here is different in all of these regards. In our simulations, the mass-weighted and flux-weighted σ_* were measured based upon the velocities of all stars appearing within a simulated diffraction slit centered on the nucleus of the galaxy. The flux-weighted measurement incorporated a toy model for dust attenuation. We measured σ_* in this way along 10^3 lines of sight and performed a statistical analysis on the directional distribution of σ_*. We were particularly interested in identifying the time-variation of σ_* during the merger process, thus these measurements were performed at very short time intervals during the merger.

The chapter is organized as follows. In section 2, we describe the numerical simulations that were performed as well as the automated analysis algorithm that was used. In section 3, we present the results of the numerical simulations and perform some additional analysis. In section 4, we conclude by discussing our findings, their implications, and their limitations.

2.2 Numerical Simulations

In order to study the evolution of σ_* with high time-resolution during the merger process, we designed a simulation code that performs a statistical analysis of the particle velocity data at short intervals during run-time. We chose to keep the simulations as simple as possible so that we could identify the purely dynamical aspects of the evolution of σ_*. The simulated galaxies were composed only of gravitationally-bound, collisionless star particles. There was no separate dark matter component nor a gas component. At fixed intervals, the code computed mass-weighted and flux-weighted values of σ_* along 10^3 random lines of sight. The measurements of σ_* were based on the velocities of stars appearing in a rectangular "diffraction slit" centered on the projected center of mass of the system. This method allowed all stars along the line

of sight to contribute to the measured value of σ_*—just as in the case of an observational measurement of σ_*. Flux-weighted values of σ_* were determined from the intrinsic luminosities of star particles, coupled with a toy model for dust attenuation. Using the values of σ_* measured along 10^3 directions, the code computed the mean, minimum, maximum, standard deviation, skewness, and kurtosis of σ_* during the merger process.

2.2.1 Code Description

Dynamics

Our N-body simulation code utilized the direct (i.e., all pairs) method to calculate the gravitational forces on each particle. The particles were softened in order to minimize the effects of two-body relaxation (White and Rees, 1978). This ensured that the stellar systems were collisionless for the duration of the simulations. The acceleration of each particle, i, was computed using a truncated Plummer softening scheme, given by

$$\ddot{\mathbf{r}}_i = -G \sum_{j \neq i} m_j \mathbf{r}_{ij} \times \begin{cases} r_{ij}^{-3} & r_{ij} > \epsilon \\ \left(r_{ij}^2 + \epsilon^2\right)^{-3/2} & r_{ij} \leq \epsilon \end{cases}$$

where $\mathbf{r}_{ij} = \mathbf{r}_i - \mathbf{r}_j$ and ϵ is the softening length. Using this scheme, particles interact as Plummer spheres when overlapping significantly and as point particles otherwise. The density profile implied by this is a Plummer sphere enclosed in a spherical surface-mass density distribution of radius ϵ. The system was integrated forward in time using the kick-drift-kick form of the leap-frog integrator (Quinn et al., 1997) with global, adaptive time stepping.

Galaxy Construction

In constructing progenitor galaxies, our code first initialized the stellar population. A list of stellar masses was made with relative abundances determined by an approximation to the Kroupa IMF (Kroupa, 2001). Stars with masses $M \geq 3M_\odot$ were then removed from the list in order to simulate the effect of an aged stellar population. Each of the N gravitationally-softened

particles in the simulation represented a population of n stars, thus the mass of each particle was determined by randomly selecting n entries from the stellar population list. The luminosity of each particle was determined from the sum of the luminosities of the n constituent star particles, which were, in turn, computed from the mass-luminosity relation (Salaris and Cassisi, 2006).

Once the particles were initialized, they were distributed in space according to the Hernquist density profile (Hernquist, 1990),

$$\rho(r) = \frac{M}{2\pi} \frac{D}{r(r+D)^3} \tag{2.1}$$

where M is the total mass of the system, and the size scale, D, of the distribution is the "Hernquist radius." The velocity distribution was chosen to reproduce the analytic result obtained from the Jeans equations, assuming an irrotational system with an isotropic dispersion tensor and Hernquist density profile (see Appendix A1). The resulting system, having been constructed stochastically, exhibited a small net linear momentum, implying a small drift velocity. All particle velocities were adjusted to remove the net linear momentum. Our newly-constructed system was then evolved forward in time. The density profile and central velocity dispersion of the newly-constructed system varied for approximately 2.5 dynamical timescales before reaching a steady configuration. This period of adjustment was apparently necessitated by the mismatch between the smooth analytic distribution used to initialize the system and the granular approximation that was actually produced. The final density profile of the progenitor system fit the Hernquist profile perfectly—within the limits of particle noise. After the initial 2.5 dynamical timescales, no evolution was observed during the subsequent ≈ 290 dynamical times for which the system was studied. Based on this analysis, we evolved each progenitor spheroid passively for 3.0 dynamical times before using it in a merger simulation.

Dust Attenuation

In order to determine how measurements of σ_* might depend on dust attenuation, a toy model for dust attenuation was included in the code. A cylindrical slab of gray attenuating material of radius, r, thickness, δ, and extinction coefficient, κ was placed concentric with the center of mass of the merging system. The flux of the ith star in the system, f_i, was then calculated according to,

$$f_i = L_i e^{-\kappa d_i} \tag{2.2}$$

where L_i is the luminosity of the ith star particle and d_i is the distance that light from the ith star traveled through the attenuating slab on its way to the virtual observer.

Measuring σ_*

The process used to measure σ_* in our code resembled the common observational technique, in that a rectangular slit of width w and length ℓ was centered on the system and the measurement of σ_* was based on the line-of-sight components of the velocities of stars within the slit. This method is different from the one often employed in many numerical simulations; simulators typically base σ_* measurements on the velocities of stars within the half-mass radius or projected half mass radius of the system (Johansson et al., 2009; Robertson et al., 2006a,b).

The measurement of σ_* proceeded as follows. First, a random viewing direction (θ, ϕ) was chosen, then the system was rotated such that the new $+z$-axis coincided with the (θ, ϕ) direction. The set of particles within the observing slit was identified using the new x- and y-coordinates. The line-of-sight velocity of each particle was then given by the new z-component of velocity. From the line-of-sight velocity distribution within the slit, the mass-weighted and flux-weighted versions of σ_* were computed as follows

$$m\sigma_* = \sqrt{v_i^2 m_i/M - (v_i m_i/M)^2} \tag{2.3}$$

$$f\sigma_* = \sqrt{v_i^2 f_i/F - (v_i f_i/F)^2} \tag{2.4}$$

with

$$M = \sum_i m_i \qquad F = \sum_i f_i$$

where the standard summation convention has been utilized; repeated indices imply a sum over that index. We use the notation $m\sigma_*$ and $f\sigma_*$ to denote mass-weighted and flux-weighted σ_*, respectively. This process was repeated for 10^3 random directions.

Directional Statistics

Once $m\sigma_*$ and $f\sigma_*$ were measured for 10^3 directions, statistical quantities were computed in order to determine the degree of anisotropy of the merger system. Specifically, the mean, minimum, maximum, standard deviation, skewness, and kurtosis of $m\sigma_*$ and $f\sigma_*$ were computed for the set of directions. Since the definitions of skewness and kurtosis vary among authors, we present the definitions that we used below

$$\text{skew}(x) = n^{-1} \sum_i (x_i - \mu)^3 / \sigma^3 \tag{2.5}$$

$$\text{kurt}(x) = n^{-1} \sum_i (x_i - \mu)^4 / \sigma^4 \tag{2.6}$$

where μ and σ are the mean and standard deviation of x, respectively and n is the sample size. The directional statistics, combined with time-evolution data, enabled us to estimate the intrinsic scatter in observations of σ_* for randomly-oriented active mergers and merger remnants.

Collisions

The code was specifically designed to study the simplest type of mergers: binary mergers of equal-mass systems (i.e., 1:1 mergers). Once a model galaxy was constructed, as described above, the galaxy was replicated and placed on a collision course with its clone. The relative position and velocity vectors (**R** and **V**) were specified, then the code adopted the zero-linear-

momentum reference frame and set the origin of the coordinate system coincident with the center of mass. This ensured that the final merger remnant would be centered at the origin.

2.2.2 Precision

Particle noise was by far the main source of uncertainty in our measurement of σ_*. We quantified the precision in the primary measurement of interest—the directional mean of σ_*—through experimentation. First, we noted that our newly constructed galaxies were perfectly spherically symmetric and isotropic—except for the statistical noise introduced by using a finite number of particles, N. In the limit as $N \to \infty$, the measurement of σ_* should be independent of the direction from which the measurement was made. This implies that the standard deviation of σ_* over the set of all viewing directions ($\sigma_{\rm d}$) should vanish in this limit. Based on this insight, we performed measurements of the standard deviation of σ_* in newly-constructed systems, measured from 10^3 random directions, for various N ranging from 10^2 to 10^5. We found the expected behavior: $\sigma_{\rm d} \propto N^{-1/2}$. Upon determining the constant of proportionality associated with our simulation parameters (namely, the system density and slit dimensions), we were able to quantify the degree of particle noise in our measurements of σ_*.

The uncertainty introduced by the error in the numerical integration scheme was negligible in comparison with the particle noise. All non-integer quantities in the code were stored as double precision floating point numbers. We used a very stringent step-size criterion in which no particle was allowed to move more than 1.1ϵ during a time-step. The total momentum of the system was conserved to within a small multiple of the machine precision and the total energy fluctuated by less than 0.1%.

2.2.3 Simulation Units & Parameters

Internally, the code used a system of units in which mass was measured in solar masses, distance was measured in parsecs, the gravitational constant $G = 1$, and time was a derived unit. However, in order to make our results easier to interpret, we have re-scaled the simulation parameters. All quantities will be presented in terms of the characteristics of the progenitor

galaxies. Our unit of distance is the half-mass radius, $r_{\rm h}$, of the progenitor, which can be written in terms of the Hernquist radius, D, as $r_{\rm h} = (1+\sqrt{2})D$. For a system with constant mass-to-light ratio, the projected half-light radius, $R_{\rm e}$, is related to $r_{\rm h}$ by $r_{\rm h} \approx 1.33R_{\rm e}$ (Hernquist, 1990). Our unit of time is the dynamical time-scale of the progenitor, given by

$$1\, t_{\rm dyn} = \sqrt{\frac{3\pi}{16G\bar{\rho}_{\rm h}}} = \sqrt{\frac{\pi^2(1+\sqrt{2})^3 D^3}{2GM}} \tag{2.7}$$

where $\bar{\rho}_{\rm h}$ is the mean density within $r_{\rm h}$. The unit of velocity is then given by

$$1\, \frac{r_{\rm h}}{t_{\rm dyn}} = \sqrt{\frac{2GM}{\pi^2(1+\sqrt{2})D}} \tag{2.8}$$

where M is the total mass of the system. In terms of these units, the gravitational constant is,

$$G = \frac{\pi^2}{2}\frac{r_{\rm h}^3}{M\, t_{\rm dyn}^2} \tag{2.9}$$

To gain a better understanding of this unit system, consider a spheroid of mass 1.0×10^{10} $\rm M_\odot$ with an effective radius of $R_{\rm e} = 2.0$ kpc. For this spheroid, the time unit is 37 Myr and the velocity unit is 70 km $\rm s^{-1}$.

After studying a large variety of initial orbital parameters, we found that the general behavior of all of the merger simulations fell between two extreme cases: head-on collisions and orbital decay mergers. In a head-on collision, the progenitors are initially separated by some distance, R, and given an initial relative speed, V, directly toward one another. In the orbital decay scenario, the two galaxies begin on circular or nearly circular orbits. As they interact through tidal forces and dynamical friction, angular momentum is redistributed and the galaxies gently merge. We analyzed these two extreme cases, as well as a representative intermediate case, in detail. For all simulations, the radius, thickness, and attenuation coefficient of the cylindrical attenuating slab were $r = 3.36\ r_{\rm h}$, $\delta = 1.24\ r_{\rm h}$, and $\kappa = 1.8\ r_{\rm h}^{-1}$, respectively. The slit width and length were $w = 0.14\ r_{\rm h}$ and $\ell = 0.70\ r_{\rm h}$, respectively. Table 2.1 summarizes the parameters that were varied in our simulations.

Table 2.1: Summary of Parameters Used

Simulation Type	N	ϵ ($r_{\rm h}$)	V ($r_{\rm h} t_{\rm dyn}^{-1}$)	R ($r_{\rm h}$)	θ (degrees)	τ ($t_{\rm dyn}$)
Head-on, short	50 000	0.0233	1.55	1.66	180	0.00942
Head-on, long	35 000	0.0262	1.55	1.66	180	0.0942
Intermediate, short	50 000	0.0233	1.60	1.69	153.2	0.00942
Intermediate, long	35 000	0.0262	1.60	1.69	153.2	0.0942
Orbital decay, short	50 000	0.0233	1.55	1.66	90	0.00942
Orbital decay, long	35 000	0.0262	1.55	1.66	90	0.0942

The qualifiers "short" and "long" refer to the duration of the simulation and the interval between measurements of σ_*. All "short" simulations were evolved forward for $\approx 8\ t_{\rm dyn}$ while the "long" were allowed to evolve for $\approx 290\ t_{\rm dyn}$. The number N is the number of particles in each progenitor system; the *total* number of particles in the merger simulation is $2N$. The initial relative speed of the galaxies is $V = |\mathbf{V}|$, their initial separation distance is $R = |\mathbf{R}|$, and the angle between $\mathbf{R}$ and $\mathbf{V}$ is θ. The interval between measurements of σ_* is τ.

2.3 Results

2.3.1 Measurement Techniques

Slit σ_* vs. Half-mass σ_*

Using our slit-based method of measuring σ_*, with the slit dimensions given in section 2.2.3, we found that σ_* in our progenitor systems was $\sigma_* = 1.07 \pm 0.01\ r_{\rm h}\, t_{\rm dyn}^{-1}$ while the value of σ_* measured within the central spherical region of radius $r_{\rm h}$ was $1.0047 \pm 0.0026\ r_{\rm h}\, t_{\rm dyn}^{-1}$. For comparison, the result obtained by analytically computing the mass-weighted mean of the line-of-sight velocity dispersion within a sphere of radius $r_{\rm h}$ for an isotropic Hernquist profile is $\approx 1.0035\ r_{\rm h}\, t_{\rm dyn}^{-1}$ while the same quantity computed within $r_{\rm h}/2$ is $\approx 1.0693\ r_{\rm h}\, t_{\rm dyn}^{-1}$ (see Appendix A1). Evidently, measuring σ_* using a narrow slit placed on the center of the galaxy yielded values that were closer to the velocity dispersion within a region smaller than $r_{\rm h}$. As the width of the slit was increased, the difference between the two measurement techniques diminished. In quiescent, isotropic systems, the two measurement techniques agreed within 2% when the width of the slit $w = r_{\rm h}$ and the methods agreed to within the measurement uncertainty when $w = 2r_{\rm h}$. As the width of the slit approached zero, particle noise made the measurement highly unreliable. For non-quiescent and non-isotropic systems, the two meth-

ods sometimes differed significantly—even when the slit was quite large. This disagreement was due to the motion of particles lying outside of the spherical half-mass region, which were included in the slit-based measurement, but absent from the spherical half-mass measurement.

Flux Weighting vs. Mass Weighting

The presence of an attenuating slab placed concentric with the galaxy had the effect of reducing the flux received from stars in the central region of the galaxy. Using the properties of the attenuating slab presented in section 2.2.3, along with Eq. (2.2), we see that the flux received from a star particle at the center of the galaxy was $f = 0.3275L$ when viewed through the thinnest portion of the slab (face-on), where L is the intrinsic luminosity of the star particle. When viewed through the thickest portion of the slab (edge-on), $f = 0.0025L$. When velocity dispersions were computed using the flux-weighting technique, the velocities of stars in the central region of the galaxy were therefore weighted less heavily. Since the stellar velocity dispersion was largest near the central region of our simulated galaxies, the flux-weighted measurement, $f\sigma_*$, was smaller than its mass-weighted counterpart, $m\sigma_*$. Using a simulation with 10^5 particles, we found that $f\sigma_* = (0.875 \pm 0.015)m\sigma_*$. In general, increasing the attenuation coefficient or the dimensions of the attenuating slab caused $f\sigma_*$ to decrease monotonically.

The presence of the cylindrical attenuator also destroyed the spherical symmetry of the system; when the mass-weighted velocity distribution was isotropic, the flux-weighted velocity distribution was not. As mentioned in section 2.2.2, the standard deviation of σ_* over the set of random viewing directions (σ_d) can be used as a measure of the anisotropy of the system's velocity distribution. Using the same 10^5 particle simulation mentioned above, the standard deviation of $f\sigma_*$ over the set of 10^3 random viewing directions was $f\sigma_\mathrm{d} = (0.123 \pm 0.017)\sigma_*$ while $m\sigma_\mathrm{d} = (0.006 \pm 0.001)\sigma_*$.

Additionally, we found that changing the radius-to-thickness ratio of the attenuating slab (r/δ) caused the anisotropy of the flux-weighted velocity distribution, $f\sigma_\mathrm{d}$ to change. The minimum value of $f\sigma_\mathrm{d}$ was found when $r/\delta \approx 0.5$, of course $f\sigma_\mathrm{d}$ also tended toward zero if either $\delta/r_\mathrm{h} \to 0$ or $r/r_\mathrm{h} \to 0$, regardless of the ratio r/δ. The value of r/δ leading to

maximum isotropy occurred in the interval $1 < r/\delta < \infty$; the exact ratio r/δ that maximized $f\sigma_{\rm d}$ depended on the relative size of the slab compared with that of the galaxy.

2.3.2 Merger Evolution

The dissipationless mergers that we studied proceeded in three primary stages: *oscillation* then *phase mixing*, and finally completion or *dynamical equilibrium*. Figures (2.1), (2.2), and (2.3) respectively illustrate the early stages of the "Head-on, short", "intermediate, short", and "orbit-decay, short" simulations from Table 2.1.

Oscillation

The oscillatory stage is characterized by the bulk motion of the two progenitor galaxies as they coalesce. As the progenitor nuclei become superimposed significantly for the first time, the density, gravitational potential, and σ_* increase rapidly. The progenitor nuclei then typically pass through one another. The density, gravitational potential, and σ_* of the central region of the merging system is then temporarily reduced. The nuclei of the systems eventually change directions and fall back onto one another, while some of the star particles that were initially less tightly bound continue on their original paths—only slightly perturbed by the motion of the nuclei. The process then repeats several times until the coherent oscillations decay away. The evolution of σ_* then becomes dominated by phase mixing. In the Head-on merger shown in Fig. (2.1) and the Intermediate merger shown in Fig. (2.2), the transition between the oscillatory and phase mixing stages occurred at approximately 1.5 $t_{\rm dyn}$ and 2.3 $t_{\rm dyn}$, respectively. In the less violent Orbital decay merger shown in Fig. (2.3), the oscillatory stage was much less pronounced because the galaxies gently spiraled into one another, but oscillations were still visible between 2.0 $t_{\rm dyn}$ and 4.0 $t_{\rm dyn}$.

Phase Mixing

The phenomenon of phase mixing arises because of the dispersion in the oscillation (or orbital) periods of the particles composing a system. Due to this dispersion, an initially coherent os-

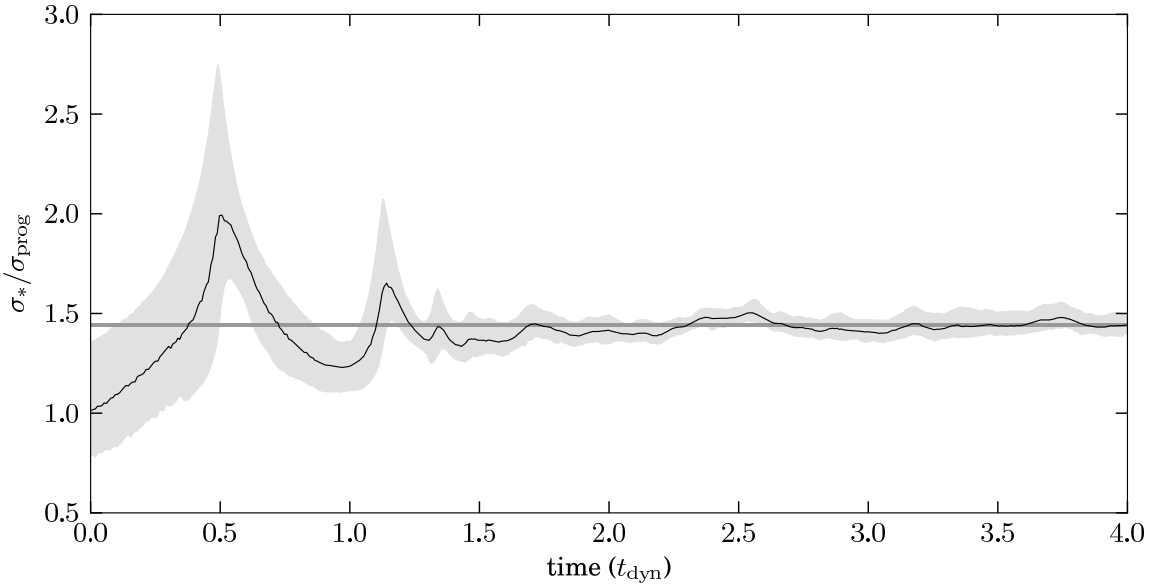

Figure 2.1: The evolution of σ_* with time during the "Head-on, short" merger of Table 2.1. We have scaled σ_* by the value of velocity dispersion of the progenitor galaxies ($\sigma_{\rm prog}$). The black curve represents the directional mean of the mass-weighted line-of-sight velocity dispersion ($m\sigma_*$) measured using the slit-based method. The upper and lower limits of the gray region are, respectively, the maximum and minimum values of $m\sigma_*$ for the set of 10^3 random viewing directions. The gray horizontal stripe is centered on the final equilibrium value of $m\sigma_*$of the merger remnant. The half-thickness of the stripe illustrates the one-sigma uncertainty due to particle noise. Thus the gray stripe is $(m\sigma_{*,\rm final} \pm \sigma_{\rm d,noise})/\sigma_{\rm prog} = 1.440 \pm 0.008$. The centers of the two progenitor galaxies first coincide at $t \approx 0.5\ t_{\rm dyn}$. The oscillation stage ends at $t \approx 1.5\ t_{\rm dyn}$. The velocity dispersion continues to fluctuate, although less significantly, in the phase mixing stage. Note: Although this simulation was evolved forward for $\approx 8\ t_{\rm dyn}$, the plot only shows the first 4 $t_{\rm dyn}$ in order to highlight the oscillatory stage of the merger.

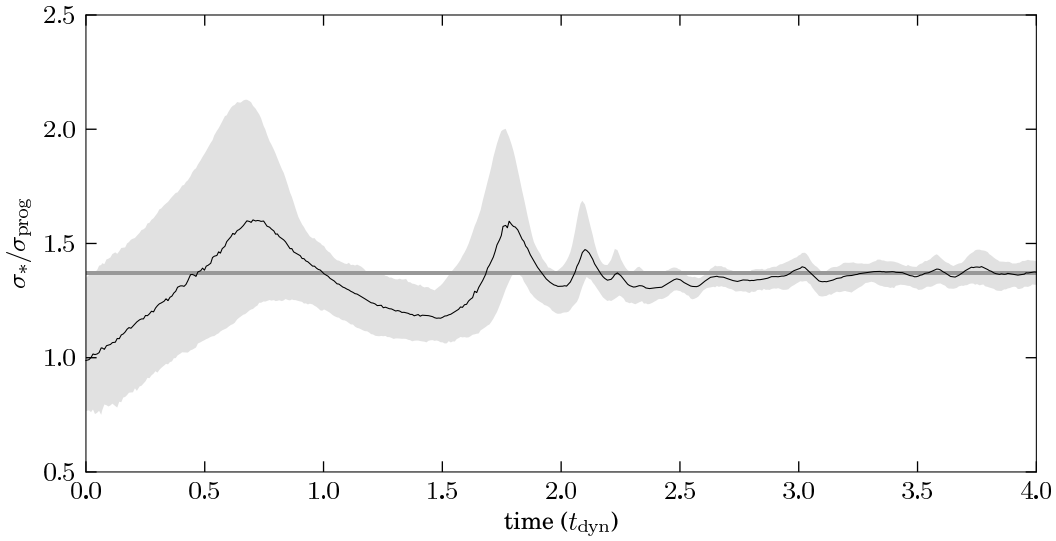

Figure 2.2: The evolution of σ_* with time during the "Intermediate, short" merger of Table 2.1. The black line, shaded region, and gray horizontal stripe are defined the same as in Fig. (2.1). The position and thickness of the gray stripe are $(m\sigma_{*,\rm final} \pm \sigma_{\rm d,noise})/\sigma_{\rm prog} = 1.373 \pm 0.008$. The centers of the two progenitor galaxies first coincide at $t \approx 0.7\ t_{\rm dyn}$. The oscillation stage ends at $t \approx 2.3\ t_{\rm dyn}$.

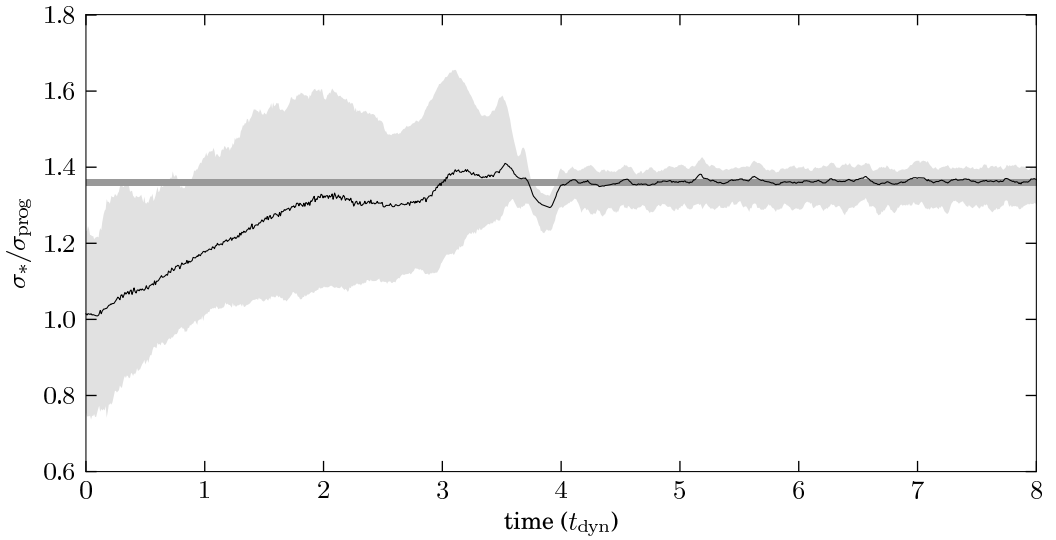

Figure 2.3: The evolution of σ_* with time during the "Orbit decay, short" merger of Table 2.1. The black line, shaded region, and gray horizontal stripe are defined the same as in Fig. (2.1). The position and thickness of the gray stripe are $(m\sigma_{*,\rm final} \pm \sigma_{\rm d,noise})/\sigma_{\rm prog} = 1.361 \pm 0.008$. The centers of the two progenitor galaxies first coincide at $t \approx 3.1\ t_{\rm dyn}$. The oscillation stage ends at $t \approx 4.0\ t_{\rm dyn}$.

cillation becomes incoherent with time and eventually vanishes. For a system consisting of a finite number of particles, this sort of phase mixing *alone* cannot be fully responsible for the termination of the oscillation stage described above because the differences between the orbital periods are necessarily finite. A finite system of uncoupled, undamped, undriven oscillators will periodically return to its initial state, meaning that episodes of coherent oscillation would recur periodically. Phase mixing plays an important role in ending the oscillation stage, but *particle interactions* are essential in preventing the recurrence of coherent oscillations. The stars in a galaxy interact indirectly through a time-varying global potential. This sort of interaction, which is most obvious during the oscillatory stage of a merger, is known as "violent relaxation" Lynden-Bell (1967). Stars also interact through close encounters with other stars, however this mode of interaction is insignificant compared with violent relaxation for most stars in a typical galaxy during the timescale of a merger. These interactions cause the period of each particle to vary with time in a non-periodic way which modifies the pure phase-mixing mechanism and prevents the return of coherent oscillations.

Visually, the process of phase mixing causes the particles of the two progenitor systems in a merger to lose their identities; it gradually becomes impossible to distinguish the distribution of particles that initially belonged to progenitor A from the distribution of particles that originally belonged to progenitor B. This is illustrated particularly clearly in figure 5 of Funato et al. (1992a).

In our Head-on and Intermediate merger simulations we observed many statistically significant variations in σ_* during the phase mixing stage of evolution. These fluctuations can be seen in Figures (2.1), (2.2), (2.4) and (2.5). We define the end of the phase mixing stage as the time after which the directional mean of σ_* can be found within the one-sigma particle noise of the equilibrium value, $\sigma_{*,\mathrm{final}} \pm \sigma_{\mathrm{d,noise}}$, with 75% confidence (note that the *process* of phase mixing continues to occur ad infinitum—only the phase mixing *stage* has an end). This is admittedly a somewhat arbitrary criterion. For the Head-on collision shown in Fig. (2.4), the phase mixing stage ended at $\approx 17\, t_{\mathrm{dyn}}$. In the Intermediate simulation, shown in Fig. (2.5), the end of the stage occurred at $\approx 11\, t_{\mathrm{dyn}}$. The Orbital decay simulation, shown in Fig. (2.3) did not have

a clearly distinct phase mixing stage. In Figures (2.4) and (2.5) a small number of two-sigma fluctuations in σ_* can be seen *after* the stated end of the phase mixing stage. Relatively large fluctuations, such as these, occurred very infrequently after the end of the stage compared with their frequency before the end of the stage.

During the phase mixing stage, fluctuations in the mean value of σ_* were accompanied by corresponding fluctuations in the minimum and maximum values of σ_*. This finding is consistent with the work of Merrall and Henriksen (2003), which found that the virial ratios, $2T/W$ oscillated with time as the systems progressed toward dynamical equilibrium (T and W are the kinetic and potential energy, respectively). Similar oscillations were also discussed by Funato et al. (1992a,b). These oscillations appear to be due to the presence of small subsets of particles in the merging system with very similar orbital periods. The rate of phase mixing depends monotonically on the difference between periods, thus particles with very similar periods mix slowly, which explains why these smaller oscillations survive longer than the bulk oscillations in the initial oscillatory stage (Funato et al., 1992b). Merrall and Henriksen (2003) found that such oscillations diminished in the continuum limit, as $N \rightarrow \infty$, but they noted that the fluctuations are indeed statistically significant and represent a physical phenomenon that occurs in systems consisting of a *finite* number of particles.

Notice that the only differences between our "short" and "long" simulations (from Table 2.1) were the number of particles, the gravitational softening length, and the σ_* measurement interval, τ. The initial orbital parameters, total mass, size, and shape of the density profile were identical. This enabled us to determine whether the fluctuations during the phase mixing stage differed for systems having the same macrostate, but different microstates. We compared the evolution of σ_* during the interval shared by both the "long" and "short" simulations (i.e., the first 8 $t_{\rm dyn}$ of each simulation) and found that the variations in σ_* were in perfect agreement within the noise limits and sampling frequency. Notably, every fluctuation in the "long" simulation was accompanied by a corresponding fluctuation in the "short" simulation. Of course not every fluctuation present in the "short" simulations could be detected in the "long" simulations because the sampling frequency in the "long" simulations was a factor of 10 lower and the noise

threshold was slightly higher. Furthermore, the pseudorandom number generator function that was used in the galaxy construction algorithm was initialized with a different random seed each time a new spheroid was constructed. This caused the particles to be arranged differently each time a new system was constructed. Therefore, the similarity between the "short" and "long" simulations implies that the statistically significant fluctuations observed during the first 8 $t_{\rm dyn}$ of the "long" simulations were evidently not artifacts of the detailed microstates of the particle systems. The fluctuations depended on the macrostate—the density profile, velocity distribution, and initial orbital parameters.

As noted previously, the phase mixing stage in the Head-on collision lasted longer than the phase mixing stage in the Intermediate collision. The Orbital decay merger lacked a distinct phase mixing stage. It appears that the duration of the phase mixing stage is inversely related to the duration of the oscillation stage. The magnitude of the time derivative of the mean gravitational potential in the early stages of the merger may be responsible for this relationship, however much more analysis would be required to verify this hypothesis. The efficiency of the mixing process may also play a role in determining the duration of the phase mixing stage. It is clear that the merger with the largest angular momentum (Orbital decay) exhibited the most short-lived phase-mixing stage, while the merger with zero angular momentum (Head-on) exhibited the longest-lived phase mixing stage. The (differential) rotation due to the presence of angular momentum, combined with dynamical friction may have accelerated the mixing process.

Dynamical Equilibrium

Once the phase mixing stage was complete, we observed no significant evolution in the mean value of σ_* in the remnant systems during the course of the $\approx 290\ t_{\rm dyn}$ that the simulations were allowed to evolve. We determined the relaxed values of the mass-weighted velocity dispersion ($m\sigma_{*,\rm final}$) by computing the time average of σ_* during the final $\approx$ 200 $t_{\rm dyn}$ of the "long" simulations. The mean value remained approximately constant—only rarely exceeding the one-sigma noise limit. For the Head-on merger, $m\sigma_{*,\rm final} = 1.54 \pm 0.01\ r_{\rm h}\, t_{\rm dyn}^{-1}$. The Intermediate and

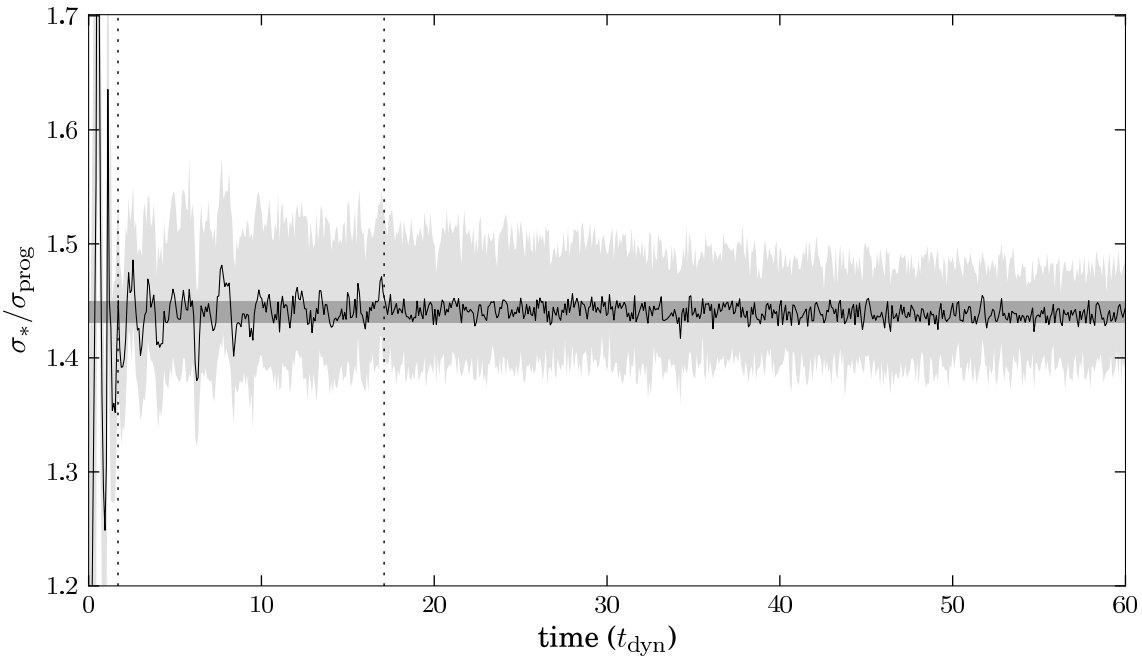

Figure 2.4: The evolution of σ_* with time during the "Head-on, long " merger of Table 2.1. The black line, shaded region, and gray horizontal stripe are defined the same as in Fig. (2.1). The position and thickness of the gray stripe are $(m\sigma_{*,\rm final} \pm \sigma_{\rm d,noise})/\sigma_{\rm prog} = 1.4399 \pm 0.0096$. The phase mixing stage ends at $t \approx 17\ t_{\rm dyn}$. The vertical dotted lines mark the approximate boundaries between the oscillation, phase mixing, and dynamic equilibrium stages. Note that the maximum value of σ_* (the upper boundary of the shaded region) continues to evolve until $\approx 45\ t_{\rm dyn}$. Although this simulation was evolved forward for $\approx 290\ t_{\rm dyn}$, the plot only shows the first 60 $t_{\rm dyn}$ because there was no visible evolution beyond 60 $t_{\rm dyn}$.

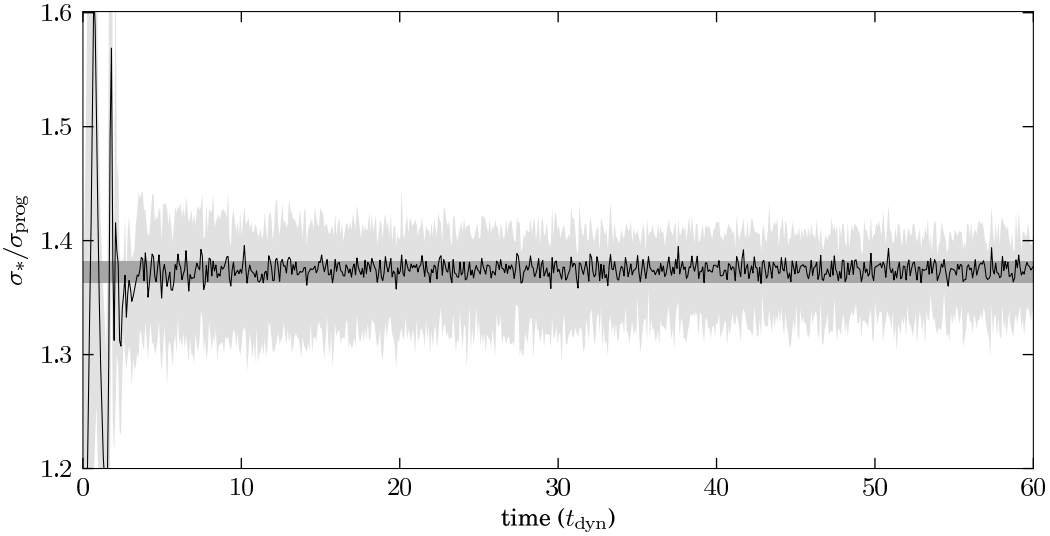

Figure 2.5: The evolution of σ_* with time during the "Intermediate, long " merger of Table 2.1. The black line, shaded region, and gray horizontal stripe are defined the same as in Fig. (2.1). The position and thickness of the gray stripe are $(m\sigma_{*,\rm final} \pm \sigma_{\rm d,noise})/\sigma_{\rm prog} = 1.3730 \pm 0.0096$. The phase mixing stage ends at $t \approx 11\ t_{\rm dyn}$.

Orbital decay mergers had identical velocity dispersions within the measurement uncertainty, with $m\sigma_{*,\rm final} = 1.469 \pm 0.010\ r_{\rm h}\, t_{\rm dyn}^{-1}$ and $m\sigma_{*,\rm final} = 1.456 \pm 0.010\ r_{\rm h}\, t_{\rm dyn}^{-1}$ respectively. As expected from the initial conditions, the Head-on merger remnant exhibited no net rotation; it was entirely supported by pressure. The Intermediate and Orbital decay remnants were supported by both rotation and pressure.

We observed the same general remnant properties described by Villumsen (1982) and González-García and van Albada (2005). In particular, for the Head-on collision remnant, the velocity dispersion was largest along the collision axis and smallest perpendicular to the axis. For the rotating remnants, the mean velocity dispersion in the orbital plane of the collision was larger than the velocity dispersion perpendicular to the orbital plane.

Figures (2.6), (2.7), and (2.8) show the evolution of $m\sigma_*$ and $f\sigma_*$ along with their corresponding directional standard deviations $m\sigma_{\rm d}$ and $f\sigma_{\rm d}$ for our three merger simulations. While there was no evolution in the *mean* of σ_*, the directional distribution of σ_* and the maximum value of σ_* over the set of directions did evolve somewhat during the dynamical equilibrium

stage. This evolution is particularly evident in Figures (2.4), (2.6), and (2.7). The anisotropy ($\sigma_{\rm d}$) and the maximum value of σ_* decreased and eventually reached stable values a few tens of dynamical timescales after the end of the phase mixing stage.

2.3.3 Additional Statistics

Suppose a non-quiescent galaxy is observed and a careful measurement of σ_* is made. With what probability will the measured σ_* fall within a specified range $\pm\Delta\sigma_*$ of the system's eventual equilibrium value of σ_*, (i.e., the value of σ_* nominally used in the $M_{\rm BH}$–σ_* and FP relation studies)? In other words, what degree of scatter is expected when measuring σ_* in a non-quiescent system and is there an offset in σ_* during dynamically non- quiescent times? The results presented above provide the first pieces of information needed to answer these questions. For instance, in Fig. (2.1), we see that, even in the most violent of the 1:1 mergers that we studied, the maximum value of σ_* that would ever be measured is less than a factor of two greater than the final equilibrium value. Neglecting the effect of flux-weighting, the minimum value of σ_* measured in an apparently coalesced system was about 70% of the equilibrium value. We expect that σ_* varies most significantly in 1:1 mergers, therefore this work suggests that a measurement of σ_* made in a non-quiescent galaxy would fall between 70% and 200% of the quiescent value. Furthermore, a random measurement of σ_* is much more likely to fall near the equilibrium value than near an extremum; in order to obtain a measurement of σ_* near an extremum, the system would have to be observed from a fortuitous viewing angle during a fairly short epoch.

The standard deviation of σ_* for the set of viewing angles in each merger is shown in the lower panels of Figures (2.6), (2.7) and (2.8). In these plots, we see that—in all three simulations—$m\sigma_{\rm d}$ was largest during the oscillatory stage with an absolute maximum value of about 25% of the equilibrium value of σ_*. After the oscillatory stage was complete, $m\sigma_{\rm d}$ was typically less than 3% of the equilibrium value of σ_*. The flux-weighted quantity, $f\sigma_{\rm d}$ was larger than $m\sigma_{\rm d}$ due to the anisotropy introduced by the slab of attenuating material.

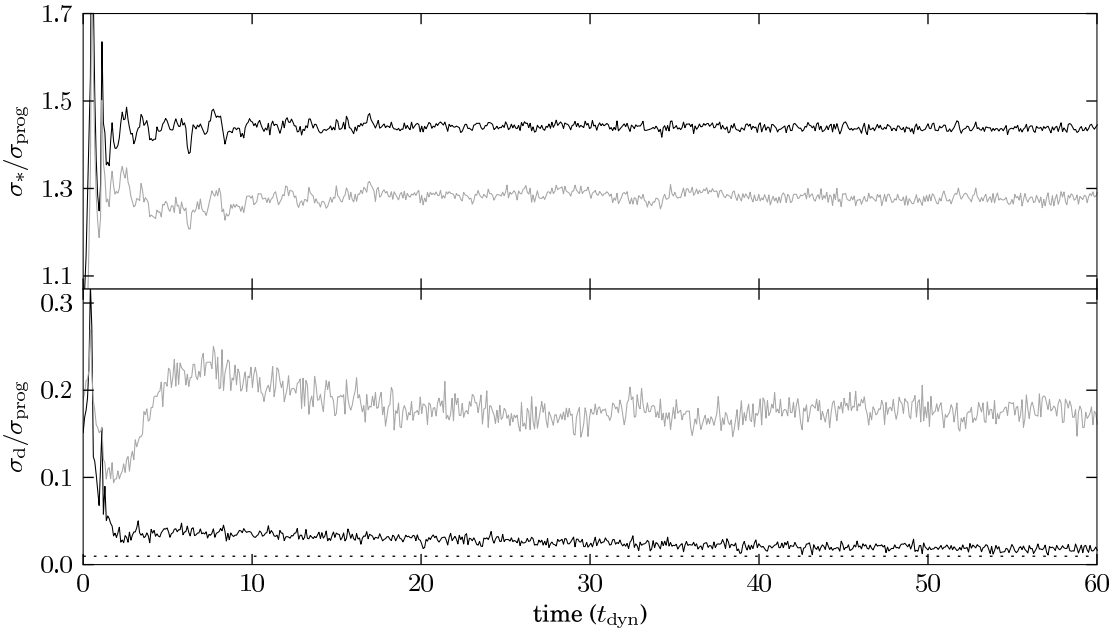

Figure 2.6: The evolution of σ_* with time during the "Head-on, long " merger of Table 2.1. **Upper panel:** The black and gray lines show the evolution of $m\sigma_*$ and $f\sigma_*$ with time, respectively. The flux-weighted quantity is systematically lower than its mass-weighted counterpart. **Lower panel:** The black and gray lines show the dispersion in the mass-weighted and flux-weighted values of σ_* for a set of 10^3 random viewing directions ($\sigma_{\rm d}$). This is effectively a measure of the anisotropy of the system. The lower dotted line shows the particle noise threshold which represents a lower limit on $\sigma_{\rm d}$; a perfectly isotropic system composed of 7×10^4 particles would have a value of $\sigma_{\rm d}/\sigma_{\rm prog} = 0.0096$, which is the position of this line. From this plot, we can see that flux-based measurements would indicate that the system is much less isotropic than it actually is. This means that flux-based measurements of σ_* from different viewing directions could differ significantly. The mass-weighted measurement shows that the system continued evolving toward a more isotropic state well after the end of the phase mixing stage.

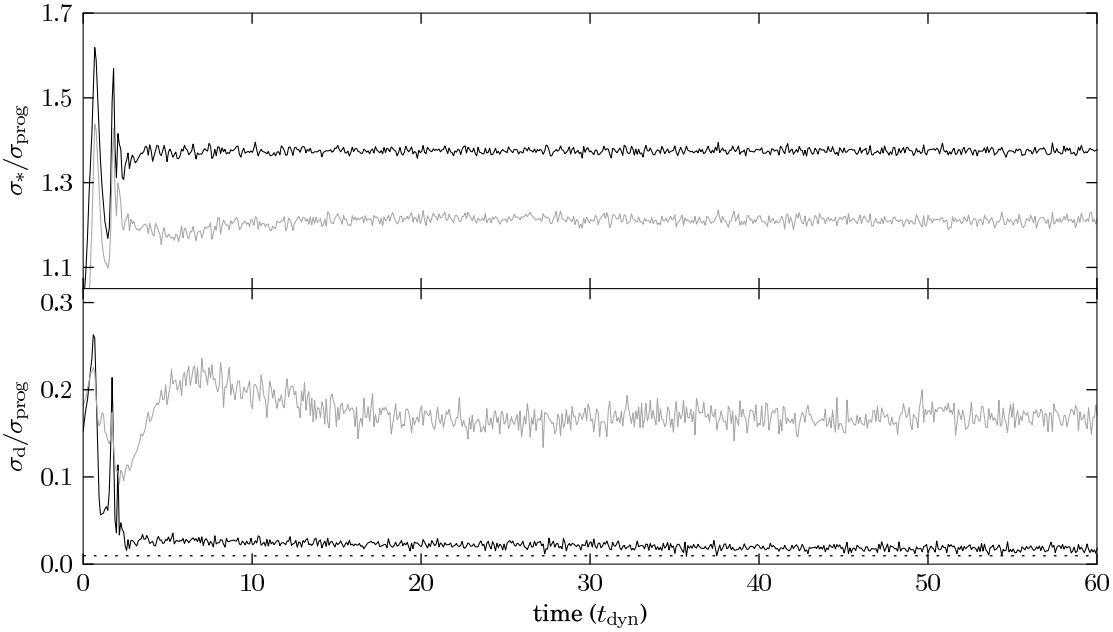

Figure 2.7: The evolution of σ_* with time during the "Intermediate, long " merger of Table 2.1. See the caption of Fig. 2.6 for a description of the plotted quantities. The effects of flux-weighting are the same as in the Head-on merger.

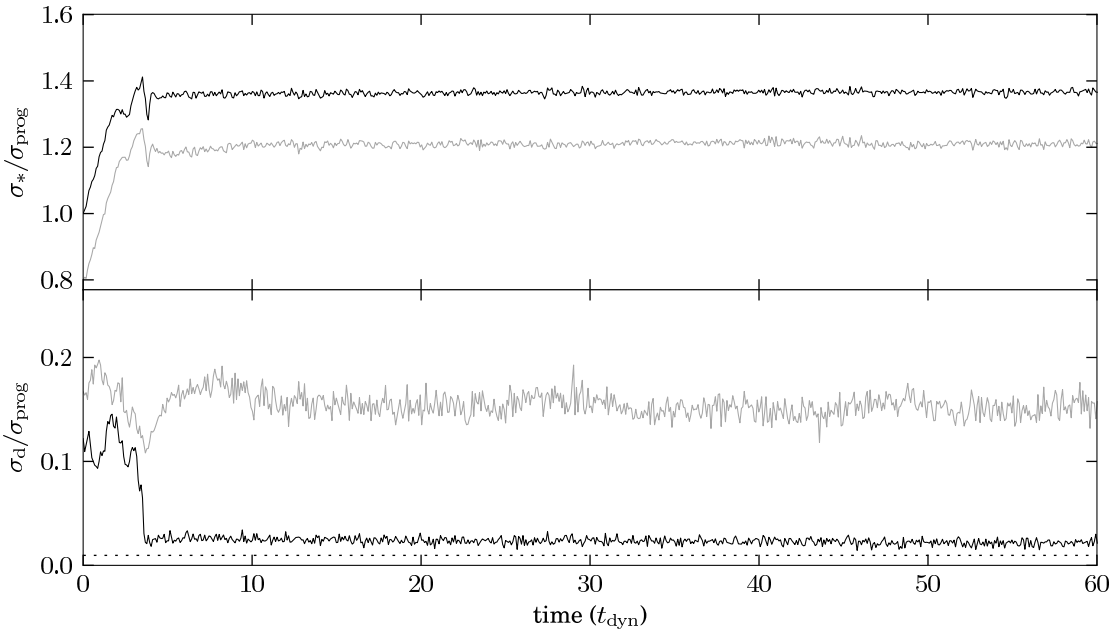

Figure 2.8: The evolution of σ_* with time during the "Orbital decay, long " merger of Table 2.1. See the caption of Fig. 2.6 for a description of the plotted quantities. Note that the remnant system shown here is less isotropic than the Head-on and Intermediate merger remnants. This is because the system is somewhat flattened due to rotation.

We have not presented plots of the skewness or kurtosis of the directional distribution of σ_* as a function of time because the large amount of noise present in these quantities prevented us from detecting any trends with time. There was, however, a clear difference between the mass-weighted and flux-weighted measurements. These differences are summarized below.

The skewness of the directional distribution of $m\sigma_*$ in the isolated progenitor system was 0.01 ± 0.23, which is consistent with zero, as expected from the manifest symmetry of the progenitor. Its flux-weighted counterpart was -2.8 ± 0.2. The skewness of $m\sigma_*$ was 0.49 ± 0.23 for each of the three simulations during the oscillatory and early phase mixing stages of evolution, but the final quiescent values differed somewhat. The quiescent values of skewness for the Head-on, Intermediate, and Orbital decay merger remnants were respectively 0.07 ± 0.22, -0.37 ± 0.25, and -0.53 ± 0.23. In each simulation, the skewness of the flux-weighted distribution was -1.0 ± 0.2 during the oscillatory and early phase mixing stages and -3.1 ± 0.1 for each of the remnant systems—consistent with the skewness of $f\sigma_*$ in the progenitors. Thus, the skewness of the flux-weighted velocity dispersion depended more strongly upon the dust geometry than the actual stellar dynamics.

Merger evolution had no measurable effect on the kurtosis of the directional distribution of $m\sigma_*$. The kurtosis of $m\sigma_*$ was 2.5 ± 0.4 for the progenitors and remained fixed at this value, within the limits of noise, for the duration of all three merger simulations. The kurtosis of $f\sigma_*$ in the progenitors, as well in each merger simulation, was consistently 11.6 ± 1.9. This elevated kurtosis indicates that much of the variability in the directional distribution of $f\sigma_*$ was due to extreme outliers, which is a direct result of the geometry of the attenuating slab.

2.4 Discussion and Conclusions

By analyzing the evolution of σ_* during three collisionless, dissipationless, 1:1 mergers of spherically symmetric systems, we identified three primary stages of evolution. During the most dramatic, early stage of the merger, σ_* undergoes large damped oscillations of increasing frequency. Following the oscillation stage, the value of σ_* can fluctuate significantly in an

apparently chaotic way for more than ten dynamical timescales as the system becomes more mixed. We called this the phase mixing stage. The phase mixing stage is followed by the dynamical equilibrium stage during which the value of σ_* remains essentially fixed, while the system evolves toward a final equilibrium state. Using the statistics computed during the collisions, we identified the extreme limits of σ_* during such galaxy mergers and provided estimates of the scatter inherent in making measurements of σ_* at random times from random viewing angles during a merger. The work of Cox et al. (2006a) hints that the evolution of sig may be more complicated in mergers that contain a dissipative component (i.e., gas). If a similar analysis were performed on a large variety of more realistic dissipative galaxy mergers with varying mass ratios, gas fractions, Hubble types, and initial orbital parameters, it would be possible to predict the scatter inherent in making measurements of σ_* in non-quiescent systems in general.

By measuring σ_* using a slit-based measurement method coupled with a toy model of dust attenuation, we found that the presence of dust in a galaxy can systematically decrease the flux-weighted value of σ_* relative to the mass-weighted measurement. Furthermore, the distribution of dust can increase the apparent anisotropy of a system. This increases the observed scatter in observational determinations of σ_*. In order to understand how dust influences measurements of σ_* in real galaxies, a more realistic model for dust attenuation is needed. We have begun a follow-up project that will use the radiative transfer code SUNRISE, (Jonsson, 2006; Jonsson et al., 2010; Jonsson and Primack, 2010) to create Doppler- broadened spectra of GADGET-2 (Springel, 2005) merger simulations at fixed time intervals. The synthetic spectra will be analyzed to determine the flux-weighted value of σ_*. This will allow us to compute σ_* in a way that is fully- consistent with the method used by observers; not only will the σ_* measurement be flux-based, but σ_* will be obtained by fitting spectral line profiles as opposed to using direct particle data as in the present work. In addition to providing us with a better understanding of how *dust* effects measurements of σ_*, the follow-up project should allow also investigate how *star formation* influences the measurement of σ_*. Rothberg & Fischer recently reported a systematic discrepancy between values of σ_* measured at different wavelengths, with lower σ_* measured for longer wavelengths (Rothberg and Fischer, 2010). Their proposed explanation for

this "σ_* discrepancy" is as follows: Stars for which σ_* was measured using near-IR CO lines are young stars located in a dusty rotating gaseous disk whereas stars measured using the shorter wavelength Ca III triplet were older. The young stars, having recently formed from collisional, dissipative, molecular gas, have lower velocity dispersion than the surrounding population of old stars because the clouds from which they formed had lower velocity dispersion than the older stellar population. These stars have not yet had time to mix with the older population and adopt the higher σ_*. This explanation seems consistent with the observations of Genzel et al. (2001) which found that the gas dynamics and stellar dynamics become decoupled during mergers. Our follow-up work should aid in understanding this "sigma discrepancy".

The merger simulations described in this work were intentionally kept simple in order to allow us to identify the most fundamental, purely dynamical aspects of the evolution of σ_* during a merger. The systems were spherical, isotropic, non-rotating, and contained no gas nor dark matter. In spite of the simplicity, we observed nontrivial aspects of the evolution. In order to identify how each additional bit of complexity effects the evolution of σ_*, we will compare these fundamental aspects of the evolution with the results of the more realistic simulations in our follow-up project. Even without performing further simulations, we can see that the time-scales and the set of possible initial orbital parameters will increase when we add a dark matter component. This is because systems of stars embedded in large dark matter halos are able to eventually merge as long as their parent halos interact sufficiently; the stellar systems themselves do not need to become superimposed during the earliest stages of the merger process because the earliest interactions primarily take place in the outer regions of the dark matter halos. The systems we modeled needed to *start out* on a collision course in order to merge. Therefore, our simulations only represented the later stages of the overall merger process—beginning with the stage at which a collision between the stellar components was imminent.

Chapter 3

Dissipative Galaxy Mergers

Abstract

In order to better understand stellar dynamics in merging systems, such as NGC 6240, we examine the evolution of central stellar velocity dispersion (σ_*) in dissipative galaxy mergers using a suite of binary disk merger simulations that include feedback from stellar formation and active galactic nuclei (AGNs). We find that σ_* undergoes the same general stages of evolution that were observed in our previous dissipationless simulations: coherent oscillation, then phase mixing, followed by dynamical equilibrium. The inclusion of gas dynamics and stellar formation in the simulations adds complexity to the σ_* evolution process, compared with dissipationless mergers. In particular, the formation of tidal dwarf galaxies introduces additional fine structure to the σ_* time series. We also find that measurements of σ_* that are based only upon the youngest stars in simulations consistently yield lower values than measurements based upon the total stellar population. This finding appears to be consistent with the so-called "σ_* discrepancy," observed in real galaxies. We note that quasar-level AGN activity is much more likely to occur when σ_* is near its equilibrium value rather than during periods of extreme σ_*. Finally, we provide estimates of the scatter inherent in measuring σ_* in ongoing mergers.

3.1 Introduction

Although measurements of σ_* are often made in merging systems, such as NGC 6240 (Oliva et al., 1999; Tecza et al., 2000; Engel et al., 2010; Medling et al., 2011), little theoretical work has been done toward understanding the detailed evolution of σ_* during the merger process. Instead, most theoretical work involving σ_* has focused on passively evolving galaxy merger remnants. It is unclear whether σ_* in a merging system is likely to be elevated or suppressed compared with its fiducial, equilibrium value; the variability of σ_* during the merger process is unknown. The time required for σ_* to reach a stable value is also unknown. These uncertainties impact any observational program in which σ_* is measured in potentially non-equilibrium systems. In particular, studies involving the $M_{\rm BH}$–σ_* relation (Ferrarese and Merritt, 2000; Gebhardt et al., 2000; Tremaine et al., 2002; Gültekin et al., 2009; McConnell and Ma, 2013) or the Fundamental Plane (FP) of elliptical galaxies (Djorgovski and Davis, 1987; Dressler et al., 1987; Davies et al., 1987; Bender et al., 1992) would benefit from a more complete understanding of σ_* in non-equilibrium systems.

The cosmological evolution of the $M_{\rm BH}$–σ_* relation, a tight relationship between the mass of the central supermassive black hole (SMBH) and σ_*, may provide insights into the formation and growth histories of galaxies and SMBHs. Several observational programs (e.g., Treu et al., 2004, 2007; Woo et al., 2006, 2008; Hiner et al., 2012; Canalizo et al., 2012) that study the cosmological evolution of the $M_{\rm BH}$–σ_* relation include measurements of σ_* in ongoing or recent mergers. Unfortunately, the general lack of knowledge regarding the proper interpretation of σ_* in such systems has cast some doubt on the validity of using these systems to study of $M_{\rm BH}$–σ_* evolution. For example, it is unknown whether these systems have unusual velocity dispersions compared with systems that are clearly in a state of dynamic equilibrium. Understanding the effect of measuring σ_* in apparently non-relaxed systems would allow for a more informed interpretation of these observations.

The FP is a relation among σ_*, the half-light radius of a spheroid, and the mean surface brightness within the half-light radius. It has been used to determine whether systems resemble

normal elliptical galaxies (Woo et al., 2004; Rothberg and Joseph, 2006), but the FP is perhaps more useful as a tool for estimating distances to galaxies. Since σ_* and surface brightness are both independent of distance, the angular size of the half-light radius can be compared with the size predicted by the FP to compute distance. As a distance estimator, the FP is accurate to within 15% (Saulder et al., 2013). A more complete understanding of the evolution of σ_* during mergers may allow the scatter in the FP relation to be better understood.

The evolution of stellar velocity dispersion during mergers has only been previously studied in detail for a set of highly idealized dissipationless merger simulations (Chapter 2 of this Dissertation). These simulations suggested that σ_* increases sharply whenever the nuclei of two progenitor galaxies pass through one another and declines as the nuclei separate. As dynamical friction and tidal effects drive the nuclei toward coalescence, the time between successive passes generally decreases. As a result, σ_* undergoes damped oscillations of increasing frequency preceding the final nuclear coalescence. After the nuclei coalesce, σ_* undergoes much smaller, chaotic oscillations as the system approaches a final state of equilibrium. However, the Chapter 2 simulations did not include gas dynamics, stellar formation, stellar evolution, rotating progenitors, disk galaxies, SMBHs, parent dark matter halos, nor any feedback mechanisms. Without including these effects, the results were not suitable for comparison to real galaxy mergers. In the present work, we address the deficiencies of the Chapter 2 simulations by performing a suite of galaxy merger simulations that include all of these missing effects.

The research described in this chapter was designed to aid in the interpretation of real galaxy mergers. When possible, we have used analysis methods inspired by observational techniques and we have refrained from using certain analysis techniques that are only possible or practical in numerical simulations. However, there is one major exception to this rule; we use mass-weighted rather than flux-weighted measurements of σ_*. In Chapter 2, we found that the presence of dust can, in principle, cause the flux-weighted value of σ_* (i.e., the quantity measured in real galaxies) to differ from its mass-weighted counterpart. We will characterize the difference between mass-weighted and flux-weighted measurements of σ_* in Chapter 4.

The present chapter is organized as follows. In Section 2, we describe the numerical simu-

lations that we performed and present details of the primary analysis routine. In Section 3, we present qualitative and quantitative results of the simulations, including the temporal evolution of σ_* and the evolution of σ_* in various stellar populations. In Section 4, we present additional statistical results regarding the intrinsic variability of σ_*. We then discuss the implications of our results and our planned future research in Section 5.

3.2 Numerical Methods

We performed a suite of binary galaxy merger simulations using the *N*-body, smoothed-particle hydrodynamics (SPH) tree code, GADGET-3 (Springel, 2005). Snapshots were saved at 5 Myr intervals, then each snapshot was analyzed automatically using the analysis and visualization code, GSNAP[1] (N.R. Stickley, in preparation), which was designed for measuring velocity dispersions, computing statistics, and creating detailed volume renderings of the gas and stars in *N*-body, SPH simulations of galaxies.

3.2.1 The Simulation Code

The stellar and dark matter particles in our simulations are simply treated as collisionless, gravitationally-softened particles. The treatment of the gas component is considerably more complicated. GADGET-3 simulates the hydrodynamics of the interstellar medium (ISM) using a formulation of SPH that simultaneously conserves energy and entropy (Springel and Hernquist, 2002). The ISM is modeled as a multi-phase medium in which cold clouds are assumed to be embedded in a hot, pressure-confining phase at pressure equilibrium (Springel and Hernquist, 2003). The gas is able to cool radiatively and become heated by supernovae. Consequently, the gas can convert between the hot and cold phases by condensing and evaporating. Supernova explosions pressurize the ISM according to an effective equation of state parameterized by $q_{\rm eos}$ such that $q_{\rm eos} = 0$ corresponds to an isothermal gas with an effective temperature of 10^4 K while $q_{\rm eos} = 1$ corresponds to the pure multi-phase model with an effective temperature of

[1] http://www.gsnap.org

10^5 K. In the intermediate cases, $0 < q_{\rm eos} < 1$, the equation of state is a linear interpolation between the isothermal and multi-phase extremes.

SMBH feedback is modeled by treating each SMBH as a sink particle that accretes gas according to the Bondi-Hoyle-Lyttleton parameterization,

$$\dot{M} = \frac{4\pi\alpha G^2 M_{\rm BH}^2 \rho_\infty}{(c_\infty^2 + v_\infty^2)^{3/2}}, \tag{3.1}$$

where ρ_∞ and c_∞ are, respectively, the density and speed of sound in the local ISM and v_∞ is the speed of the SMBH relative to the local bulk motion of the ISM. The dimensionless parameter, α, is a correction factor introduced in order to account for the fact that the Bondi radius of the SMBH is smaller than the resolution limit of the simulation. The bolometric luminosity of the accreting SMBH is $L = \epsilon_r \dot{M} c^2$, where $\epsilon_r = 0.1$ is the radiative efficiency. A small fraction of the luminosity (5% in our case) is assumed to couple with the nearby surrounding gas (i.e., the gas within the SMBH's smoothing kernel), causing it to become heated. The accretion rate is limited by the Eddington rate.

The star formation rate (SFR) depends on the density of the cool gas in the simulation. Specifically, SFR $\propto \rho_{\rm sph}^{1.5}$, where $\rho_{\rm sph}$ is the density of the cool gas. The constant of proportionality is chosen such that the simulated star formation rate surface density agrees with observations (Kennicutt, 1998; Cox et al., 2006b). In order to simulate basic stellar evolution, an instantaneous recycling approximation is used; a fraction of the newly-formed stars is assumed to explode immediately as supernovae, enriching and heating the surrounding ISM. Stellar wind feedback is simulated by stochastically applying velocity "kicks" to gas particles, removing them from the dense star-forming region (Springel and Hernquist, 2003). Mass is removed from the gas and used to create new stellar particles. Each newly-created star particle carries with it a formation time variable. This makes it possible to determine the age of each star particle that formed during the simulation.

Simulation Parameters

Our progenitor systems were constructed according to the method of Springel et al. (2005). In summary, each system contained a stellar bulge with a Hernquist density profile (Hernquist, 1990) of scale length, $R_{\rm bulge}$, and an exponential disk of stars and gas. Each disk-bulge system was embedded in a dark matter halo with a Hernquist density profile of scale length, $R_{\rm DM}$. A single SMBH particle was placed at the center of each system. In order to test for stability, candidate progenitors were evolved forward in isolation; only stable systems were used in our merger simulations. The details of each progenitor are presented in Table 3.1.

We designed our suite of merger simulations to span a broad range of possible merger scenarios (see Table 3.2 for details). Our standard merger, labeled S1 in Table 3.2, was a tilted disk, prograde-prograde, 1:1 merger in which the gas fraction in the disk of each progenitor was 0.2. In simulations S2–S7, we independently varied the orbital parameters, mass ratios, and gas fractions in order to determine the effect of each property on the evolution of σ_*. In simulation S8, we varied the initial orbital parameters and increased the spatial and mass resolution of the stars and gas particles by decreasing the gravitational softening length (ϵ) and increasing the number of particles, respectively. The initial masses of the SMBH particles were chosen to fall within the 1σ scatter of the observed $M_{\rm BH}$–σ_* relation from Tremaine et al. (2002).

In all simulations, the gravitational softening length of the dark matter and SMBH particles was 90 pc, the accretion parameter, α, from Equation (3.1) was set to 25, and we used $q_{\rm eos} = 0.25$. The simulations were performed in a non-expanding space, rather than a fully cosmological setting.

Measuring σ_*

The primary quantity of interest, σ_*, is the standard deviation of the line-of-sight velocities of stars within the projected half-light radius of a galaxy's spheroidal component. In practice, observational measurements of σ_* are typically performed by placing a rectangular slit mask across the center of the system in question to approximately isolate the half-light radius. The

Table 3.1: Progenitor Galaxy Parameters

Model	$N^a_{\rm part}$ (10^5)	c^b	σ_* (km s^{-1})	$M^c_{\rm BH}$ (MM$_\odot$)	$R^d_{\rm DM}$ (kpc)	$R^d_{\rm bulge}$ (kpc)	$R^e_{\rm disk}$ (kpc)	$M_{\rm total}$ (GM$_\odot$)	$M_{\rm bulge}$ (GM$_\odot$)	$M_{\rm disk}$ (GM$_\odot$)	$f^f_{\rm gas}$
A	16.08 [8.04+1.13+4.50+2.41]	9.5	89.9 ± 1.7	5.41	27.75	1.16	3.87	865.9	13.0	30.3	0.2
B	8.03 [4.02+0.61+2.44+0.96]	10.5	68.5 ± 2.1	1.83	20.49	0.87	2.92	432.7	5.2	16.4	0.2
C	4.02 [2.01+0.36+1.45+0.20]	12.5	55.4 ± 2.5	0.51	14.30	0.64	2.12	216.2	1.1	9.7	0.2
D	16.07 [8.04+0.56+5.06+2.41]	9.5	89.9 ± 1.7	5.41	27.75	1.16	3.87	865.9	13.0	30.3	0.1
E	16.08 [8.04+2.25+3.38+2.41]	9.5	89.9 ± 1.7	5.41	27.75	1.16	3.87	865.9	13.0	30.3	0.4
F	25.17 [12.58+1.88+7.50+3.21]	9.5	89.9 ± 1.7	5.41	27.75	1.16	3.87	865.9	13.0	30.3	0.2

a The total number of particles [dark matter + gas + disk stars + bulge stars] in multiples of 10^5.
b The concentration of the dark matter halo.
c The mass of the central black hole, measured in mega solar masses.
d Scale length of the Hernquist profile.
e Radial scale length of the stellar disk. The scale length of the gas disk is a factor of six larger in each progenitor.
f The fraction of $M_{\rm disk}$ in the form of gas.

Table 3.2: Merger Simulation Parameters

Simulation	Progenitors	Mass Ratio	r_0^a (kpc)	$r_{\rm min}^b$ (kpc)	θ_1^c (deg)	ϕ_1^c (deg)	θ_2^d (deg)	ϕ_2^d (deg)	ϵ^e (pc)
S1	A+A	1:1	150	5	25	-20	-25	20	25
S2	A+A	1:1	150	5	205	-20	-25	20	25
S3	A+A	1:1	150	5	205	-20	155	20	25
S4	B+A	1:2	150	5	25	-20	-25	20	25
S5	C+A	1:4	150	5	25	-20	-25	20	25
S6	D+D	1:1	150	5	25	-20	-25	20	25
S7	E+E	1:1	150	5	25	-20	-25	20	25
S8	F+F	1:1	120	10	-30	0	30	60	20

a The initial nuclear separation distance.
b The nuclear pericentric distance of the initial orbit.
c The initial orientation of galaxy 1. The angles θ and ϕ are spherical coordinates measured in degrees, where $\theta = \arctan\left[(x^2+y^2)^{1/2}/z\right]$ is the inclination angle of the disk with respect to the orbital plane, $\phi = \arctan(y/x)$, and the orbital plane is $z = 0$.
d The initial orientation of galaxy 2.
e The gravitational softening length of stars and SPH particles. The softening length of dark matter particles and SMBHs was 90 pc in all simulations.

light passing through this slit mask is then analyzed spectroscopically. In our analysis, σ_* was measured using a method intended to mimic this common observational technique. The σ_* measurement algorithm, implemented within GSNAP, began by centering a virtual rectangular slit mask of width w and length ℓ on the galaxy of interest. A viewing direction, (θ, ϕ) and slit position angle α, were then chosen and the system was rotated such that the old (θ, ϕ) direction corresponded with the new z-axis. The system was then rotated by α around the z-axis so that the new x- and y-axes were parallel with the width and length of the slit, respectively. All stars appearing in the slit were identified and stored in a list. Finally, the masses, m_i, and the line-of-sight component of the velocities, v_i of all stars in the list were used to compute the mass-weighted stellar velocity dispersion, σ_*,

$$\sigma_* = \sqrt{v_i^2 m_i/M - (v_i m_i/M)^2} \tag{3.2}$$

with

$$M = \sum_i m_i$$

where the standard summation convention has been utilized; repeated indices imply a sum over that index.

No attempt was made to separate rotation from purely random motion. Consequently, measurements of σ_* in a dynamically cold rotating disk of stars yields larger values when measured along the plane of the disk than when measured perpendicular to the disk. This choice was motivated by the fact that many observational measurements of σ_* are unable distinguish rotation from pure dispersion.

Directional Statistics

At 5 Myr intervals, σ_* was computed along 10^3 random directions, uniformly (i.e., isotropically) chosen from the set of all possible viewing directions. For each viewing direction, a random slit mask position angle was chosen uniformly from the interval $0 \leq \alpha \leq \pi$ in order to simulate the effect of measuring σ_* in randomly oriented galaxies from random directions—just as is done when measuring σ_* in real galaxies. Using this interval potentially introduces a bias since slits oriented at $\alpha = 0$ and $\alpha = \pi$ are identical and are thus counted twice. In practice, this bias was not detectable. Once the measurements of σ_* were made, GSNAP computed the directional mean, maximum, minimum, and standard deviation of σ_* for the set of 10^3 directions. When two progenitor galaxies were present in the system, measurements of σ_* were performed on only one of the progenitors. In the two simulations containing progenitors of unequal mass, the measurements were centered upon the larger system.

Precision

Particle noise was the main source of uncertainty in our measurements of σ_*. We quantified the uncertainty by first constructing spherically symmetric particle distributions of the same size and mass as the galaxies that we were analyzing. These particle systems were perfectly spherically symmetric—except for the statistical noise introduced by using a finite number of particles, N. In the limit as $N \to \infty$, measurements of σ_* in such systems become independent of direction. Upon measuring the directional standard deviation of σ_* (denoted $\sigma_{\rm d}$) in these

spherical systems for various N ranging from 10^3 to 10^6, we found the expected behavior: $\sigma_{\rm d} \propto N^{-1/2}$. Determining the constant of proportionality associated with our simulation parameters allowed us to compute the noise threshold associated with each individual measurement of σ_* in each simulation. In our plots of σ_*, the uncertainty due to particle noise was comparable to the thickness of the plotted lines unless otherwise indicated in the plot itself.

Slit Size

As mentioned previously, σ_* is typically defined as the velocity dispersion of stars falling within the half-light radius of the spheroidal component of a galaxy. In a disk galaxy containing a bulge, the starlight originating within the half-light radius of the *central bulge* is typically analyzed to obtain σ_*. In elliptical systems, the relevant light originates within the half-light radius of the *entire system*. Of course, many systems do not have well-defined spheroidal components. The lack of a spheroid makes it difficult to rigorously define σ_*—particularly in irregular galaxies—since measurements of σ_* depend on the size of the slit. To simplify matters, we have used a fixed slit of width $w = 2$ kpc and length $\ell = 20$ kpc for all measurements of σ_* throughout this chapter. This rather large slit size, which corresponds to a slit of width $\approx 1''$ at a redshift of 0.1, allowed us to ensure that a large number of particles contributed to the measurement of σ_*, thereby minimizing particle noise. In our progenitor systems, this choice of slit size led to a systematic increase in the measured σ_* of $\approx 7\%$, compared with a slit that only included stars within the projected half-light radius of the bulge ($w = 0.3$ kpc, $\ell = 3$ kpc). In our merger remnants, no difference was detected between slits measuring 2×20 kpc and those measuring 0.3×3 kpc.

3.3 Results

3.3.1 Merger Evolution

In order to better understand the following discussion, it will be helpful to refer to Figures 3.1 and 3.2. In Figure 3.1, we present time series data for σ_* and the SMBH separation distance

Table 3.3: Summary of Merger Characteristics

Simulation	t_1^a (Gyr)	t_2^a (Gyr)	t_3^a (Gyr)	t_{nc}^b (Gyr)	t_{end}^c (Gyr)	σ_i^d ($km\,s^{-1}$)	σ_1^e ($km\,s^{-1}$)	σ_2^e ($km\,s^{-1}$)	σ_3^e ($km\,s^{-1}$)	σ_{final}^f, † ($km\,s^{-1}$)	$\sigma_d{}^g$, † ($km\,s^{-1}$)
S1	0.37	2.06	2.30	2.40	3.62	89.9 ± 10.1	127.98	215.28	188.34	151.34 ± 0.85	6.59 ± 0.30
S2	0.37	2.17	2.40	2.47	4.09	90.2 ± 10.3	155.02	198.91	183.90	146.38 ± 0.67	5.04 ± 0.23
S3	0.37	2.09	2.31	2.45	3.40	89.6 ± 9.7	161.00	201.36	189.36	156.72 ± 0.92	5.52 ± 0.19
S4	0.42	2.04	2.30	2.40	3.73	89.6 ± 9.3	111.37	200.03	174.92	136.57 ± 0.50	8.19 ± 0.26
S5	0.46	2.37	2.71	2.89	4.69	89.9 ± 9.2	101.57	164.86	155.24	118.40 ± 0.46	7.94 ± 0.31
S6	0.37	2.09	2.32	2.40	3.59	89.3 ± 10.3	127.69	206.70	182.75	149.42 ± 0.75	6.74 ± 0.29
S7	0.37	2.03	2.26	2.35	3.54	90.9 ± 8.5	129.66	206.76	187.24	146.85 ± 0.98	6.84 ± 0.61
S8	0.27	3.28	3.57	3.72	4.79	86.3 ± 5.1	95.5	224.37	189.71	152.42 ± 0.37	5.57 ± 0.25

a The time of the nth pass.
b The time of nuclear coalescence.
c The duration of the simulation. This indicates the time at which the snapshots in Figure 3.3 were saved. This is the only quantity in the table that does not depend upon the initial conditions of each merger.
d The velocity dispersion of the progenitor system. The reported uncertainty is the standard deviation of the set of 10^3 random measurements.
e The mean value of σ_* at the climax of the nth pass (i.e., the value at time t_n).
f The mean velocity dispersion of the remnant system.
g The standard deviation of the directional distribution of σ_*.
† This was obtained by averaging the time series over the final 500 Myr of the simulation. The reported uncertainty is the standard deviation of the time series during the 500 Myr interval.

during the 1:1 merger, S1. Vertical lines indicate key moments in the evolution of the system. Images of the system during these moments, or "snapshots," are shown in Figure 3.2. Note that whenever the word "nucleus" is used in this chapter, we are referring to the position of one of the local maxima in the density field of the system. Nuclei also coincide with local minima in the smoothed gravitational potential field, but nuclei do not necessarily coincide with the positions of SMBHs. When we say that nuclei have coalesced, we mean that two local minima in the gravitational potential field have combined to form a new, deeper global minimum that persists indefinitely.

As described above, each simulation began with two disk galaxy progenitors composed of a central bulge, a stellar disk, a thin disk of gas, a dark matter halo, and a central SMBH. The exact details of each merger, listed in Table 3.1, varied, but they all shared the following qualitative features: As soon as the simulations began, star formation commenced. A spiral density pattern developed in the gas component of each progenitor. Enhanced star formation in the dense regions of gas led to a spiral pattern in the distribution of new stars. As the density of the spiral arms increased, the preexisting population of older disk stars gradually began participating in the spiral pattern, but only slightly.

The parent dark matter halos of the progenitors initially overlapped somewhat, however the stellar components were initially significantly separated. The progenitors followed approximately parabolic orbits while approaching one another. Tidal forces grew stronger and began to visibly elongate and warp the progenitors as they prepared to collide. Shortly before reaching their pericentric distance, the galaxies began to overlap significantly and σ_* began increasing. Simultaneously, the standard deviation of the σ_* distribution ($\sigma_{\rm d}$) increased. The gas components of the progenitors collided and became compressed. A small fraction of the gas lost enough angular momentum in this initial collision to begin migrating toward the nuclei of the progenitors. As the nuclei reached the pericentric distance, σ_* reached a maximum value. This increase in σ_* was primarily due to the projected streaming motion of the progenitors rather than a true increase in σ_*; lines of sight perpendicular to the collision axis experienced very little enhancement in σ_*, while lines of sight coinciding with the collision axis (i.e., lines of

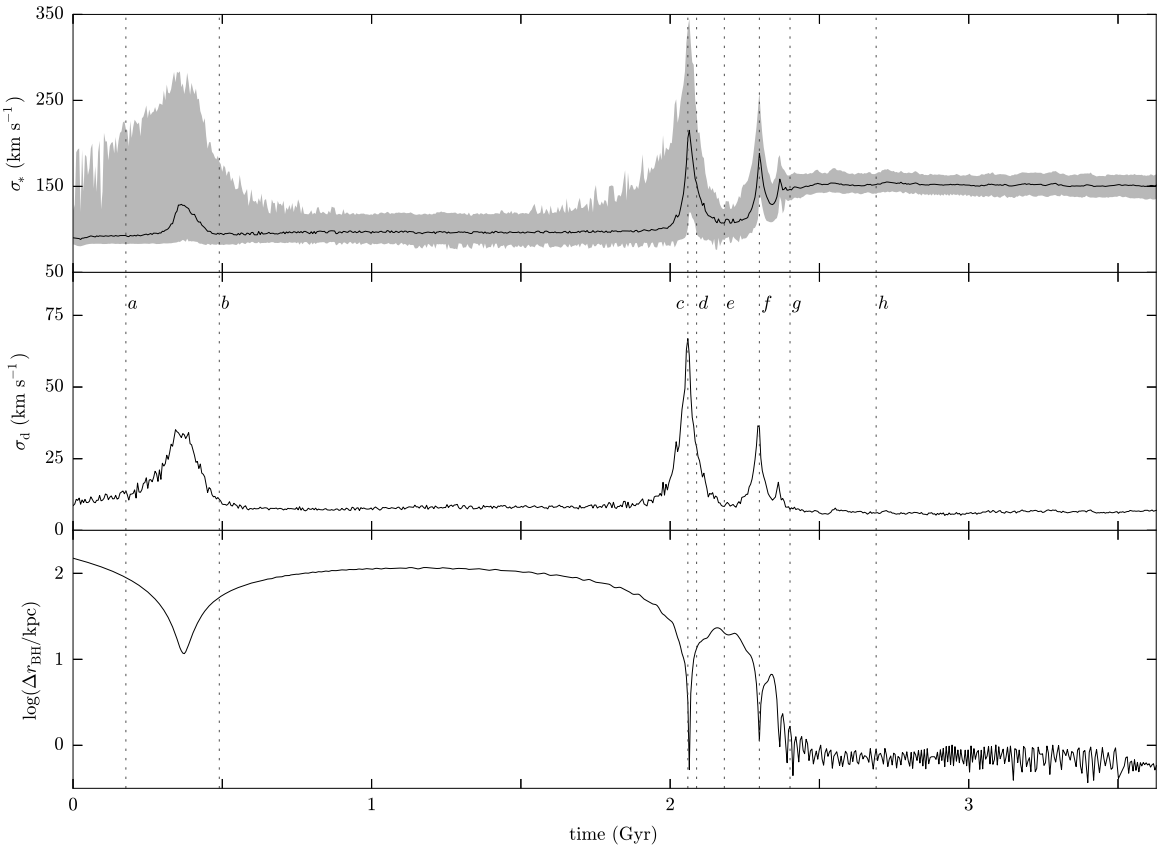

Figure 3.1: Merger evolution time series for simulation S1. Upper panel: The mean value of σ_* over the set of 1000 viewing directions is plotted in black. The upper and lower edges of the gray shaded region show the maximum and minimum values of σ_*. Middle panel: The standard deviation of the set of σ_* measurements. Lower panel: The distance between the two SMBH particles. This is a proxy for the distance between the nuclei of the two progenitors. The dotted vertical lines indicate the time coordinates of snapshots that are examined in further detail later in this chapter. Visual renderings of these snapshots are presented in Figure 3.2. The snapshots are located at $a = 0.177$ Gyr, $b = 0.490$ Gyr, $c = 2.060$ Gyr, $d = 2.089$ Gyr, $e = 2.181$ Gyr, $f = 2.299$ Gyr, $g = 2.401$ Gyr, and $h = 2.690$ Gyr.

sight along which stars of both bulges simultaneously fell within the measuring slit) yielded the largest values of σ_*.

While receding from the first encounter, the velocity dispersion of each progenitor quickly returned to its pre-collision value. Strong tidal tails and a bridge of stars and gas began forming. A small amount of gas finally reached the nuclei and triggered short, sporadic episodes of AGN activity upon reaching the SMBHs. Gas in the tidal tails collapsed to form thin filaments as the galaxies continued to recede. The filaments then fragmented to form clumps from which clusters of stars soon formed as discussed in Elmegreen et al. (1993), Barnes and Hernquist (1996), Wetzstein et al. (2007), and references therein. The approximate time of the fragmentation and cluster formation in merger S1 is marked by snapshot *b* in Figure 3.1. These clusters, which can be seen in Figure 3.2 and Figure 3.3 as bright compact spots, most likely represent tidal dwarf galaxies. With diameters of 50–300 pc and masses of 10^7–$10^9\,M_\odot$, these systems lie near the resolution limit of our simulations; some of the smaller ones may merely indicate the formation sites of small structures such as globular clusters. Observational evidence for such tidal dwarf galaxies is reviewed in Dabringhausen and Kroupa (2013). After receding from one another, the progenitors eventually reversed direction and began approaching one another on a trajectory that was much more nearly head-on than the first approach.

Upon the second approach, the interstellar gas of the two progenitors collided once again (snapshot *c*), losing considerably more angular momentum this time. In contrast with the first encounter, σ_* increased along all lines of sight; the minimum, maximum, mean, and standard deviation of σ_* increased sharply as the nuclei passed through one another and then decreased as the nuclei receded (see snapshots *d* and *e*). As the nuclei reversed direction again, σ_* nearly returned to its initial value. Simultaneously, in-falling clumps of low-angular momentum gas began reaching the central SMBHs, triggering significant episodes of AGN activity. The nuclei then began approaching one another while stars in the outer regions of the merging system, where the dynamical timescale was longer and the stars were less tightly bound, continued on nearly the same trajectories that they followed during the second approach—essentially unaffected by the motion of the nuclei.

As the nuclei began to overlap for the third time, AGN activity decreased significantly and σ_* increased once again (snapshot *f*). After passing through one another once more, the velocity dispersion of each nucleus decreased somewhat, but it did not return to its initial value. This process was repeated several more times in rapid succession, with more stars being shed from the nuclei during each reversal. The nuclear turnaround distance decayed until the two nuclei eventually coalesced (at snapshot *g*). Oscillations in the value of σ_* decayed away during this stage and the system adopted a new, stable σ_*. During the final stages of nuclear coalescence, gas and stars of low angular momentum began falling into the deep potential well of the new nucleus. This triggered a nuclear starburst which was soon followed by the highest SMBH accretion rates of the entire merger process. The accretion episodes during this stage were more frequent and more sustained than at any other time during the simulations (see images of snapshot *g* for the corresponding morphology). The surrounding gas became heated by the AGN, expanded, and drove significant gas outflows (see Hopkins et al., 2006, for a detailed discussion of these phenomena). The stars that fell toward the nucleus soon passed through the nucleus and emerged in spherical waves on the other side only to fall back onto the nucleus again. The effect of the stars falling toward the nucleus, overshooting, and then falling back caused small, statistically significant fluctuations in σ_*—the same oscillations that were observed in the "phase mixing" merger stage described in Chapter 2. The amplitude of these oscillations gradually decreased as the system became more throughly mixed. Stars that were ejected after the second and third passes gradually fell back toward the nucleus during the $\approx$ 1 Gyr following the final coalescence. In all of our simulations, clumps of gas that were ejected without being significantly heated earlier in the merger process also fell back toward the nucleus and formed a series of nuclear disks with diameters ranging from 100 pc to 10 kpc (disks smaller than 100 pc could not be resolved). The formation of similar disks is discussed in Barnes (2002). Gas of sufficiently low angular momentum was able to accrete onto the SMBH(s), causing another period of significant AGN activity $\gtrsim$1 Gyr after final coalescence. This late-stage accretion was observed in all of our mergers except for the lowest gas mass fraction merger, S1. In mergers that still contained two distinct SMBHs at this late stage, the formation of the nuclear disks

allowed for efficient angular momentum transfer from the SMBHs to the disk material, as discussed in Gould and Rix (2000) and Escala et al. (2005). In real galaxies, the SMBHs have most likely merged before this late stage; the spatial resolution of our simulations was insufficient to follow the details of the binary SMBH orbital decay (Escala et al., 2005), thus the SMBH merger timescale could not be accurately simulated. Images of the final remnant galaxies are presented in Figure 3.3.

3.3.2 Dependence upon Initial Parameters

The general shapes of the three time series shown in Figure 3.1 are shared by all of our mergers. Rather than presenting plots for each merger, we have summarized the basic features of each merger in Table 3.3. We report the time coordinates of the first three passes (t_1–t_3), the mean stellar velocity dispersion of the systems during each pass (σ_1–σ_3), the time at which the nuclei coalesced ($t_{\rm nc}$), the value of σ_* in the remnant, and the duration of each simulation.

Simulations S1, S2, and S3 tested the dependence of σ_* upon the spin-orbit configuration of the initial system. From the data, it appears that configurations of lower net angular momentum cause more significant increases in σ_* during the first encounter; the high angular momentum, prograde-prograde merger (S1) exhibited the lowest σ_1 value, while the merger of lowest angular momentum (S3) exhibited the highest value of σ_1. No other trends were observed with respect to the spin-orbit configuration.

The gas fraction of the disk component was varied from 0.1 to 0.4 in simulations S1, S6, and S7. The elapsed time between the first and second encounters was mildly dependent on the gas fraction, with higher gas fractions leading to shorter intervals. This was likely caused by the dissipative, collisional nature of the gas; when more gas was present, translational kinetic energy was more efficiently converted into internal energy, resulting in slightly lower recession velocities. The star formation rate was higher in mergers with larger gas fractions, since these systems contained more raw material from which to build stars. In Figure 3.3, we see that the number of tidal dwarf galaxies also increased with gas fraction. The presence of more dwarfs

made the time series data more noisy as the gas fraction increased, however, no trend was detected in the mean value of velocity dispersion in the remnant, σ_{final}.

In simulations S1, S4, and S5, the mass ratio of the progenitors was varied. Unsurprisingly, systems of comparable mass were able to disturb one another more effectively. This led to more significant enhancements in σ_* during the merger process. The other trends evident in S1, S4, and S5 can be attributed to the varying total masses of these systems; the systems of higher total mass merged more rapidly and produced systems of higher σ_*.

In simulation S8, as well as many low-resolution trial simulations, the orbital parameters were varied. Smaller pericentric distances lead to faster mergers and larger enhancements in σ_* during the first pass. In the case of nearly head-on initial encounters, σ_* reaches its absolute highest value during the first pass rather than the second pass.

3.3.3 The Distribution of σ_*

While the time series presented in Figure 3.1 are helpful for understanding the evolution of σ_* with time, they do not contain much information regarding the distribution of σ_* during the merger process. To supplement the time series data, we present, in Figure 3.4, the angular and probability distributions of σ_* in four snapshots during merger S1. For each of these four snapshots, σ_* was measured along 20,000 lines of sight.

In the progenitor galaxy, σ_* is distributed nearly isotropically. The presence of a stellar disk is evident from the symmetry about the equator of the system ($\theta = 90°$). Measurements of σ_* along lines of sight perpendicular to the disk are diminished by the presence of the disk stars while measurements made along the edge of the disk are enhanced somewhat because, from these sight lines, the disk's rotation can contribute to the velocity dispersion measurements.

The second snapshot of interest (snapshot *c*) was recorded shortly before the climax of the second encounter. It shows that the highest values of σ_* are measured along the collision axis (denoted by the star symbols) while the lowest values are measured perpendicular to the axis. Furthermore, the positive skew of the probability distribution indicates that a random measurement of σ_* during a collision is more likely to yield a value near the mean or minimum

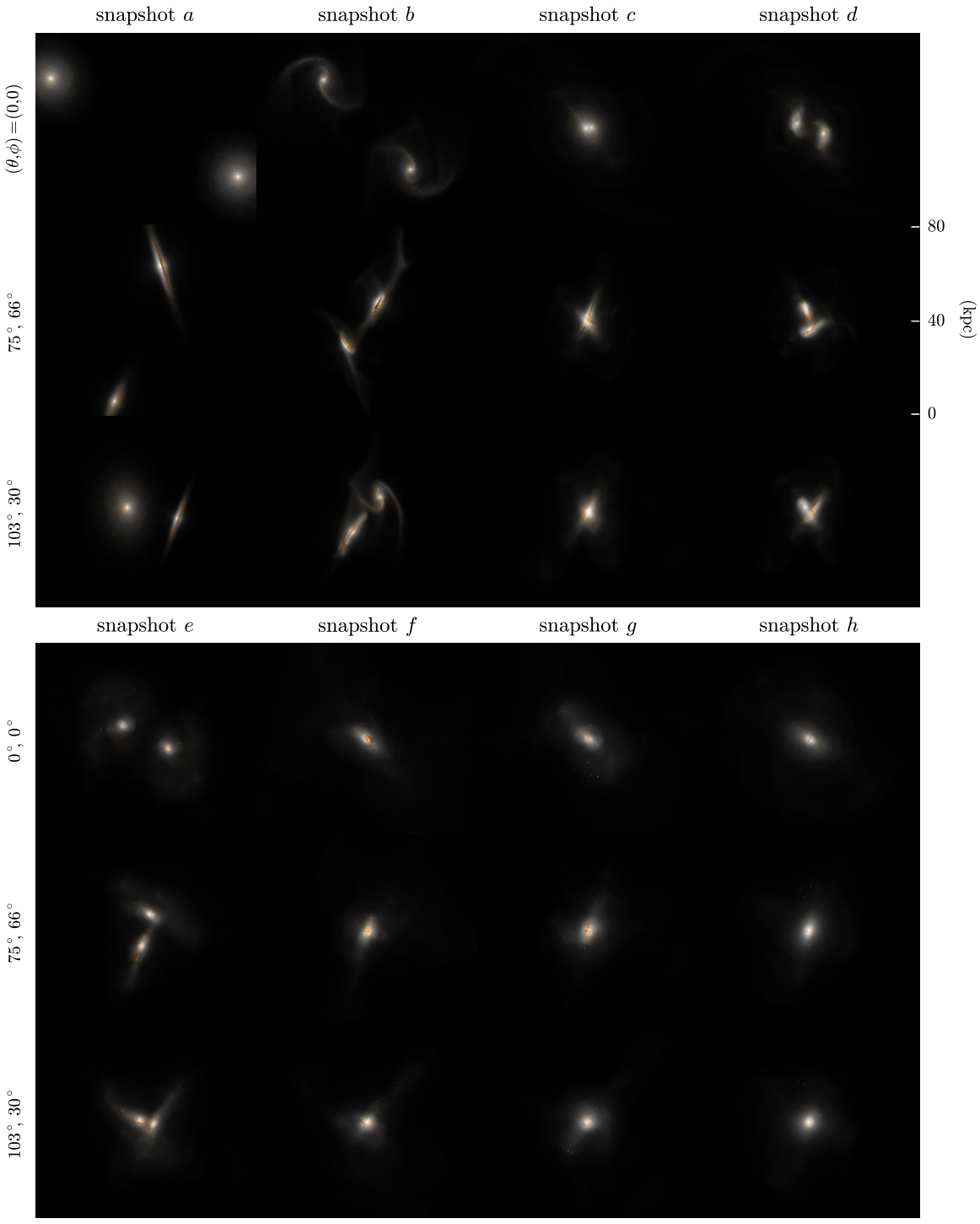

Figure 3.2: Visualizations of snapshots from simulation S1, created using GSNAP's volume rendering algorithm. The snapshot times correspond to the dotted vertical lines in Figure 3.1. Each snapshot is shown from three directions, indicated in spherical coordinates on the left. The width and height of each image is 93.75 kpc and 81.19 kpc, respectively.

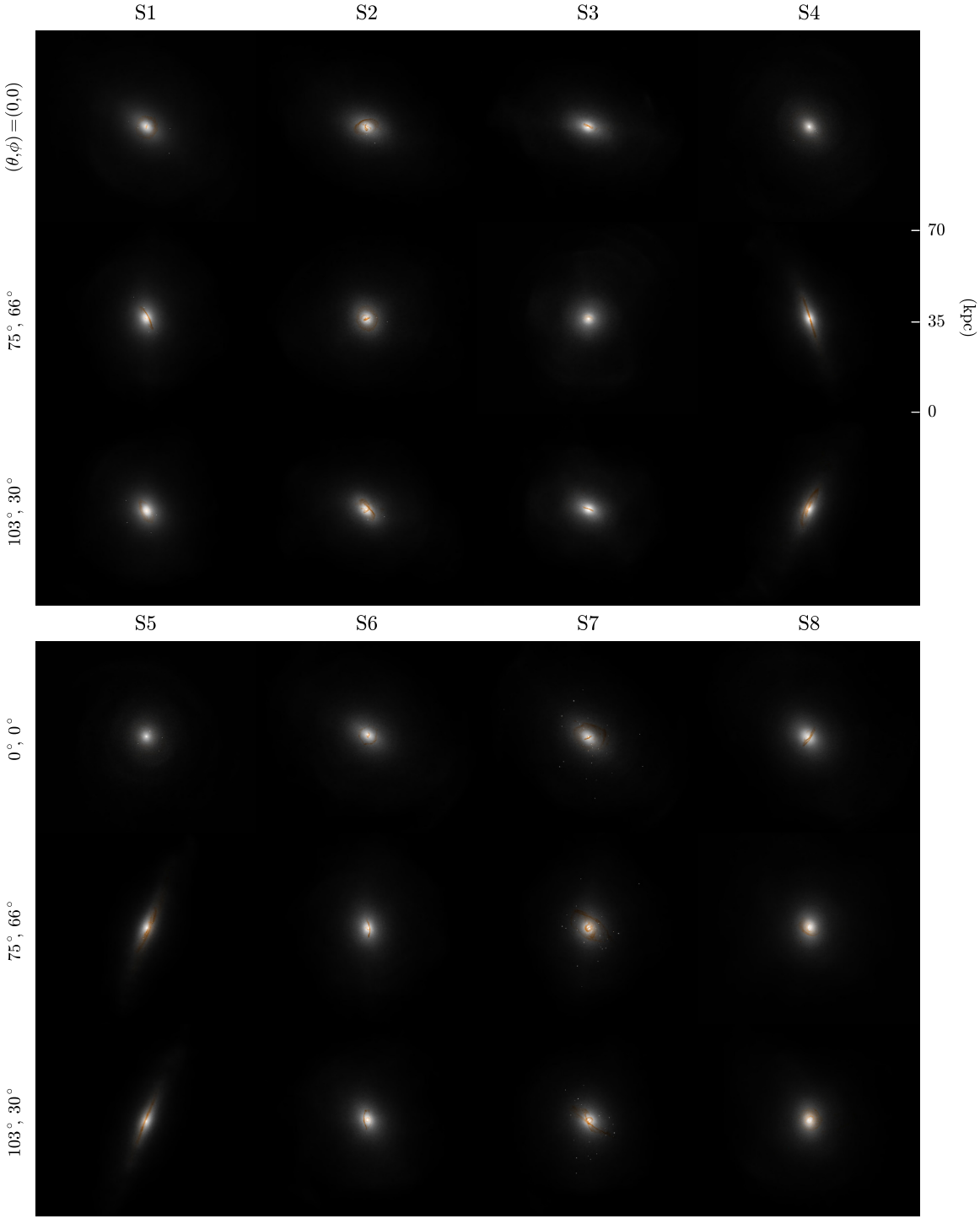

Figure 3.3: The remnants of merger simulations S1–S8, listed in Table 3.2. The simulation time of each snapshot is listed in Table 3.3, as $t_{\rm end}$. Each remnant is viewed from the same three directions as the images in Figure 3.2. Each field of view measures 84.38 kpc × 73.071 kpc. All remnants are elliptical except for S4 and S5—the unequal mass mergers. All systems contain nuclear disks.

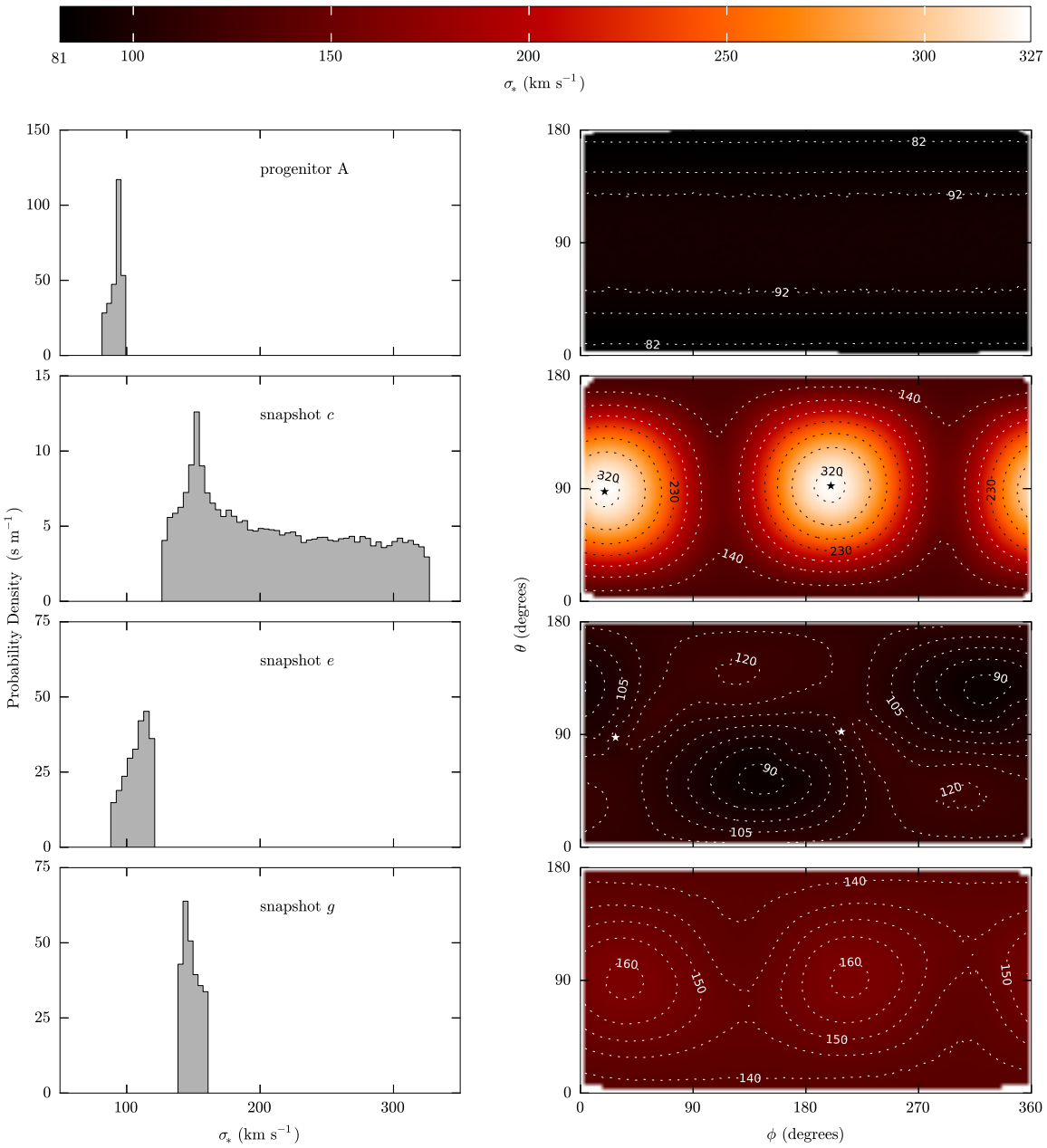

Figure 3.4: The angular and probability distributions of σ_* in progenitor galaxy A (upper panel), followed by snapshots *c*, *e*, and *g* of simulation S1 (see Figure 3.1 for more information on the meaning of these labels). For each snapshot, σ_* was measured along 20,000 random directions. The contour plots on the right show the directional variation of σ_*, while the histograms on the left show the corresponding probability distributions. The star symbols indicate the directions that lie along the instantaneous collision axis, where applicable. For a discussion of this figure, see section 3.3.3.

rather than near the maximum possible value ($\sigma_{*,\max}$). The reason σ_* is highest along the collision axis is twofold: (1) the two progenitors are moving with respect to each other along this axis; their combined bulk motion is mistaken for stellar velocity dispersion when the system is viewed along this direction, and (2) the actual velocity dispersion of each progenitor increases along the collision axis during collisions. These separate effects are discussed in more detail in the next section.

Midway between the second and third passes (snapshot *e*), the lines of sight yielding the maximum measurements of σ_* no longer coincide with the instantaneous collision axis. We can also see that a random measurement of σ_* is more likely to fall near the maximum value than near the minimum. However, the system is considerably more isotropic than it was during the climax of the second pass, so the difference between the minimum and maximum values of σ_* is much less significant here.

Immediately after nuclear coalescence (snapshot *g*), σ_* is already distributed quite uniformly; the difference between the maximum and minimum σ_* is much smaller than during snapshot *c*. The contours in the angular distribution plot for snapshot *g* indicate that the velocity dispersion is highest along a preferred axis—similar to the distribution in snapshot *c*. This axis corresponds to the collision axis during the last few encounters before coalescence, which is not necessarily the same as the collision axis during the second pass.

3.3.4 Random versus Streaming Motion

The measurements of σ_*, discussed above, have been based upon a straightforward application of Eq. (3.2) to all stars appearing in a slit mask centered on one of the nuclei of a merging system. Since this is the observationally accessible quantity, it would be more appropriate to refer to this version of σ_* as the *apparent* velocity dispersion. The apparent velocity dispersion includes the effects of rotation and bulk motion whereas the *intrinsic* velocity dispersion is due to the purely random motion of stars in the system.

Suppose two systems with intrinsic velocity dispersions σ_1 and σ_2 move toward or away from one another with speed v. Let m_1 and m_2 be the portions of the stellar masses of systems 1

and 2 that appear within a slit. Using Eq. (3.2), it is possible to show that the apparent velocity dispersion along the line of sight connecting the centers of two systems is given by,

$$\sigma_* = \sqrt{f_1\sigma_1^2 + f_2\sigma_2^2 + f_1 f_2 v^2}, \tag{3.3}$$

where f_i are the fractional masses,

$$f_i = \frac{m_i}{m_1 + m_2}.$$

For the special case of two identical systems of velocity dispersion σ_0 on a collision course, a measurement of σ_* along the collision axis will yield

$$\sigma_* = \sqrt{\sigma_0^2 + (v/2)^2}, \tag{3.4}$$

since $m_1 = m_2$ and $\sigma_1 = \sigma_2 = \sigma_0$.

In major mergers, the σ_* appearing on the left side of Equations (3.3) and (3.4) typically corresponds to the maximum measurement of velocity dispersion in the merging system. Thus, $\sigma_{*,\mathrm{max}}$ can be used as an approximation for this quantity. The relative radial speed of the two systems, v, can be approximated using the relative radial speed of the two SMBHs. More precisely, if $\mathbf{r}$ is a position vector pointing from one black hole to the other and $\mathbf{v}$ is the corresponding relative velocity vector, the speed v is given by $v = |\hat{\mathbf{r}} \cdot \mathbf{v}|$, where $\hat{\mathbf{r}} = \mathbf{r}/|\mathbf{r}|$.

In the special case of a merger of identical systems, measuring $\sigma_{*,\mathrm{max}}$ and v allows us to infer the intrinsic velocity dispersion (σ_0) of each system, using Equation (3.4). In Figure 3.5, we show the result of decomposing measurements of apparent velocity dispersion into streaming and intrinsic components. The analysis was performed on merger S1, which began as a merger of identical systems. The upper panel shows $\sigma_{*,\mathrm{max}}$ and $v/2$ while the lower panel shows the intrinsic velocity dispersion, σ_0, measured along the collision axis. The results suggest that the mean of σ_* over all directions (the dashed line in the lower panel) closely traces the intrinsic velocity dispersion (the solid line). The intrinsic velocity dispersion along the collision axis is only mildly elevated in comparison with the mean value of σ_*. However, there are several

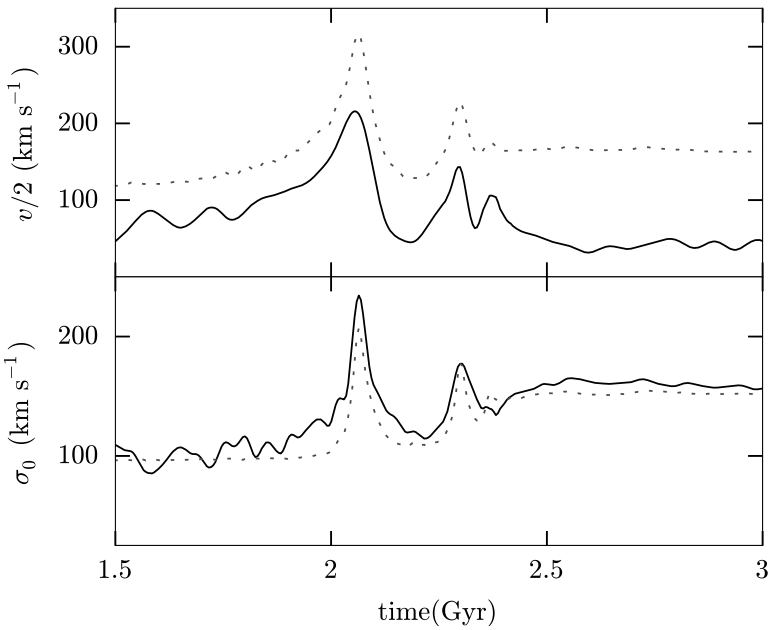

Figure 3.5: Separating the intrinsic and apparent velocity dispersions. Upper panel: The solid black line shows $v/2$, defined in Section 3.3.4. The gray dashed line shows the maximum apparent velocity dispersion ($\sigma_{*,\mathrm{max}}$) as a function of time during merger S1. Both quantities have been smoothed over time to remove high frequency fluctuations. Lower panel: The solid line shows the intrinsic velocity dispersion, σ_0, discussed in Section 3.3.4. The dashed line shows the mean value of σ_* over the set of 1000 viewing directions; it is a smoothed version of the plot in the upper panel of Figure 3.1. Note that the mean velocity dispersion closely traces the intrinsic velocity dispersion.

caveats: First, we note that the velocity of a SMBH does not trace the velocity of its parent nucleus perfectly. In general, each SMBH particle orbits the center of its parent nucleus. We have smoothed the ν time series in order to remove high frequency variations caused by this motion. For consistency, we also smoothed the $\sigma_{*,\mathrm{max}}$ time series. Secondly, the velocity of a nucleus does not always trace the bulk velocity of its parent progenitor galaxy. In fact, neither progenitor galaxy has a well-defined bulk velocity during a collision; as the progenitor systems become increasingly superimposed, the streaming velocity in each progenitor begins to vary with position. Finally, even though $\sigma_{*,\mathrm{max}}$ is usually a good approximation for the quantity on the left side of Equation (3.4), this is not necessarily true at the turnaround times when the streaming velocity is low. In such cases, the maximum velocity dispersion is not necessarily measured along the collision axis (see Figure 3.4). In light of these complexities, it would be best to interpret the resulting plot of σ_0 qualitatively rather than quantitatively.

3.3.5 Evolution with Stellar Age

It has long been known that the velocity dispersion of stars in the disk of the Milky Way increases with age. This so-called "age-velocity relation," along with the phenomena which cause it, have been studied for more than six decades (Spitzer and Schwarzschild, 1951, 1953; Barbanis and Woltjer, 1967; Hänninen and Flynn, 2002; Nordström et al., 2004). More recently, it has been shown that measurements of σ_* in more distant galaxies can depend upon the population of stars being measured (Rothberg and Fischer, 2010; Rothberg et al., 2013). Specifically, measurements of σ_* that are based upon the spectral features of younger stars yield lower values than measurements of σ_* which include all stars or only older K and M stars. To explain this "σ-discrepancy," Rothberg et al. argue that stars are born with low velocity dispersion, since the gas from which stars form is dynamically cold, due to its dissipative, collisional nature.

In order to investigate whether our simulations exhibited age-dependent σ_*, we performed the analysis described in sections 3.2.1 and 3.2.1 using only stars in specified age ranges. Before presenting our findings, though, we note that the results presented in this section necessarily depend strongly upon the less robust aspects of the simulation code—namely, the numerical

methods used to simulate the hydrodynamics, star formation, and SMBH feedback. These methods effect the timing, location, and rate of the star formation. Furthermore, the particles traced by our simulations do not represent individual stars. Instead, they represent small regions of star formation. This means that cluster evaporation and other small-scale effects are not included. Therefore, our results regarding the evolution of σ_* with stellar age are less robust than our age-independent analysis.

In Figure 3.6, we present the evolution of σ_* for stars in three age bins during simulation S1 by plotting the offset from the instantaneous global value of σ_* (i.e., the value of σ_* based on stars of all ages). The star formation rate is plotted in the same figure for reference.

Stars that formed during the first 0.5 Gyr of the simulation were located in the disks of the progenitor systems. These stars were born with $\sigma_* \approx 12\,\mathrm{km\,s^{-1}}$ lower than the global velocity dispersions of their parent galaxies. Immediately after the first pass, the offset was a mere $\approx 7\,\mathrm{km\,s^{-1}}$. These stars gradually mixed and became dynamically heated. By the end of the simulation, they were essentially dynamically indistinguishable from the system as a whole.

The evolution of stars that formed between 1.0 Gyr and 1.5 Gyr (i.e., between the first and second passes) after the beginning of the simulation was more complicated because approximately 70% of these stars formed in tightly-bound tidal tidal dwarf-like systems. The dwarf galaxies repeatedly passed near the nuclei of the larger systems. This lead to large fluctuations in the σ_* evolution time series. While the two primary galaxies were approaching one another, in preparation for their second encounter, σ_* in this age bin generally increased. However, after the second pass, σ_* began decreasing; the offset from the global σ_* increased while the global value remained essentially constant, as seen in Figure 3.1. This behavior is due to the orbital decay of the satellite galaxies in which these stars are primarily located.

Finally, stars that were born between 2.5 Gyr and 3.0 Gyr (i.e., immediately following nuclear coalescence) formed exclusively in the nuclear disks and satellite galaxies (in the case of simulation S1, 85% formed in the nuclear disks while the remaining 15% formed in the satellite galaxies). The behavior of σ_* in this group was similar to the 1.0 Gyr to 1.5 Gyr group, although the offset was larger by $\approx 10\,\mathrm{km\,s^{-1}}$.

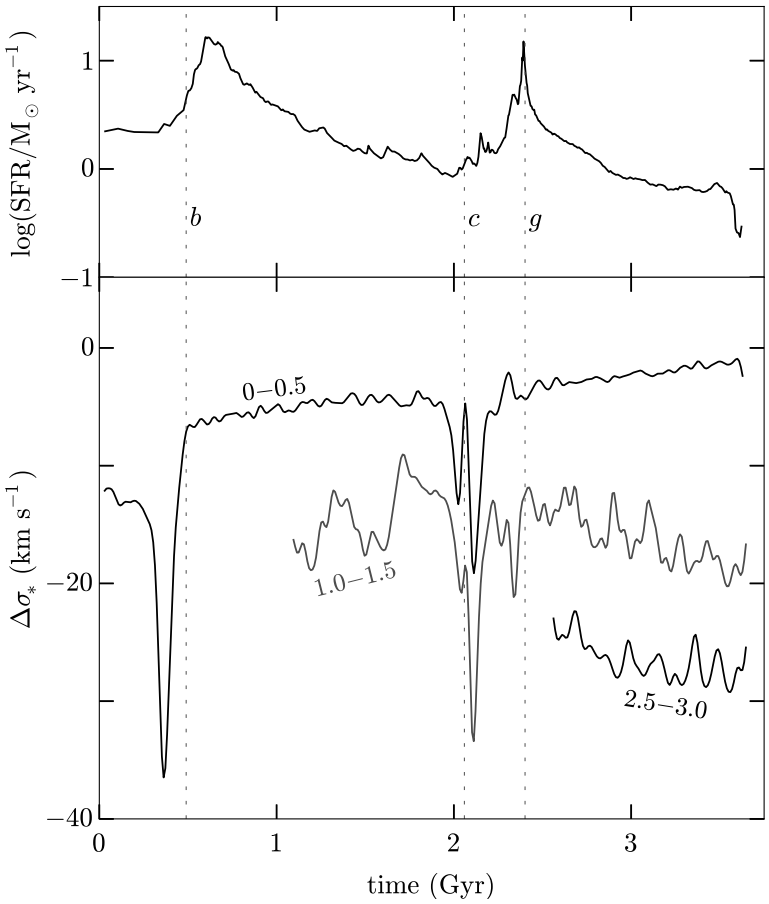

Figure 3.6: The evolution of σ_* for various stellar age bins. Upper panel: The star formation rate in simulation S1. Lower panel: The offset from the global, mean velocity dispersion that includes stars of all ages, $\Delta\sigma_* = \sigma_* - \sigma_{*,\mathrm{all}}$ for three stellar age bins of width 0.5 Gyr. Each line is labeled with its age bin. For example, the top line shows the evolution of $\Delta\sigma_*$ for all stars that were born between time $t = 0$ Gyr and $t = 0.5$ Gyr. The vertical dashed lines indicate snapshot times introduced in Figure 3.1.

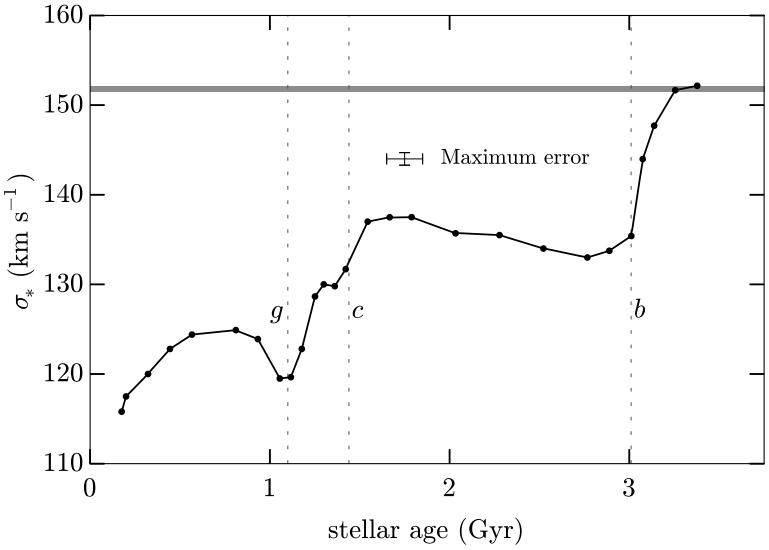

Figure 3.7: The relation between σ_* and stellar age in simulation S1. The snapshot examined here was saved at 3.5 Gyr (i.e., stars that formed at $t = 0$ Gyr are 3.5 Gyr old). The vertical dashed lines indicate the ages of stars that were born at the corresponding snapshot times shown in Figures 3.1 and 3.6. The horizontal bar indicates the global value of σ_* in the current snapshot.

In Figure 3.7, we have plotted σ_* as a function of stellar age in the remnant system in a simulation snapshot that was saved at $t = 3.5$ Gyr. From this, it is clear that younger stars tend to have lower σ_* than older stars, but there are complexities; the history of the merger has been imprinted onto the dynamics of the remnant. The stars that formed before the first pass (i.e., the stars older than 3.0 Gyr) have had time to become dynamically heated. As we saw in Figure 3.6, these stars were initially rapidly heated during the first pass and then gradually heated during the remainder of the merger. Stars that formed immediately after the first pass have had fewer opportunities to become mixed and heated. As mentioned in the discussion of Figure 3.6, many of these stars formed in tidal dwarf galaxies that underwent a decrease in σ_* after the second pass. Consequently, the oldest of these stars have the lowest value of σ_*, so the slope of the relation is inverted for stars between 1.7 Gyr and 2.7 Gyr old. Stars that formed during and after the second pass have had even fewer opportunities to become dynamically heated. All of the stars that were born during the second starburst (indicated by the vertical dashed line labeled *g*) formed either in the nuclear cluster of the newly-coalesced

system or the satellite galaxies, with the majority forming in the nuclear cluster. These stars cooled dynamically over time as the orbits of the satellite galaxies decayed. Finally, the majority (85%) of the stars with ages less than 0.5 Gyr, formed in nuclear disks with very low velocity dispersion and have not had time to become substantially heated.

3.4 Additional Statistics

3.4.1 AGN Activity

Observations examining the cosmic evolution of the $M_{\rm BH}$–σ_* relation (e.g., Treu et al., 2004, 2007; Woo et al., 2006, 2008; Hiner et al., 2012; Canalizo et al., 2012) appear to indicate that SMBHs formed more rapidly than their host galaxies; given a fixed value of σ_*, galaxies at redshifts of $z > 0.1$ have more massive black holes than local galaxies. Unfortunately, in order to measure $M_{\rm BH}$ in non-local galaxies, a SMBH must be actively accreting gas. Exclusively using AGN host galaxies in such studies raises the concern that the sample may be biased in various ways. For example, AGNs are often associated with galaxy merger activity (e.g., Canalizo and Stockton, 2013, and references therein). Depending on the timing of the AGN activity with respect to the merger activity, measuring σ_* in AGN hosts galaxies could introduce extra scatter in the resulting $M_{\rm BH}$–σ_* relation or it could systematically bias the value of σ_* to higher or lower values, leading to an artificial offset.

In order to determine whether σ_* differs statistically between AGN host galaxies and inactive galaxies, we examined the dynamical circumstances under which significant accretion occurred during each of our simulations. The characteristic SMBH accretion timescale in our simulations was shorter than, or comparable to, our resolution limit of 5 Myr; the accretion rate frequently changed by factors of 10–100 between consecutive snapshots. Consequently, we likely did not capture *all* of the enhanced accretion activity. Nevertheless, by examining all of our simulations, we were able to clearly identify periods during which significant accretion was likely to occur as well as periods during which significant accretion was not likely. For a detailed discussion of AGN lifetimes in hydrodynamic simulations similar to ours, as well as a

summary of observational evidence, see Hopkins et al. (2006), Hopkins and Hernquist (2009) and references therein. We found that accretion corresponding to a bolometric luminosity of 10^{44} erg s^{-1} appeared to be a natural threshold separating the most luminous AGN activity from the much more frequent periods of less significant accretion. Incidentally, 10^{44} erg s^{-1} is also commonly adopted as the threshold separating quasars and Seyfert galaxies, so we use the phrases "significant accretion" and "quasar-level accretion" interchangeably.

All significant (quasar-level) accretion occurred during four periods. In Figure 3.8, these periods are shown with gray shading along with generic merger time series plots of σ_*, star formation rate, and black hole separation. Period I occurred shortly after the first pass while the progenitors were receding from one another. Period II occurred between the second and third passes. Both progenitors hosted quasars during these periods, but usually not simultaneously; the quasars turned on and off independently of one another, as discussed in more detail by Van Wassenhove et al. (2012). This suggests that binary quasars with separations of 10–100 kpc are rare, relative to the occurrence of quasars in general. Period III began at the moment of nuclear coalescence and period IV occurred long after coalescence, when some of the gas that was not significantly heated during period III fell toward the nucleus. Periods III and IV were associated with the most luminous quasars observed during our mergers, with $L_{\rm bol} \sim 10^{45}$ erg s^{-1}. Interestingly, quasar-level accretion was never observed during the second or third passes when the velocity dispersion was substantially elevated. This may be due to the v_∞ term in the denominator of Equation (3.1), since the relative speed of the SMBH with respect to the surrounding gas tends to increase during the collisions. Accretion corresponding to bolometric luminosities of $L_{\rm bol} < 10^{44}$ erg s^{-1} occurred sporadically at all times after the first pass—including the second and third passes. We note that quasar-level accretion did not occur during all four periods in each simulation, however when quasar-level accretion was detected, it was always during one (or more) of the four periods identified in Figure 3.8. While this does not imply that quasar-level accretion never happens during other stages of the merger, it suggests that quasar activity is rare during other stages of merger evolution.

For each simulation, the mean offset of σ_* from the fiducial value was computed during

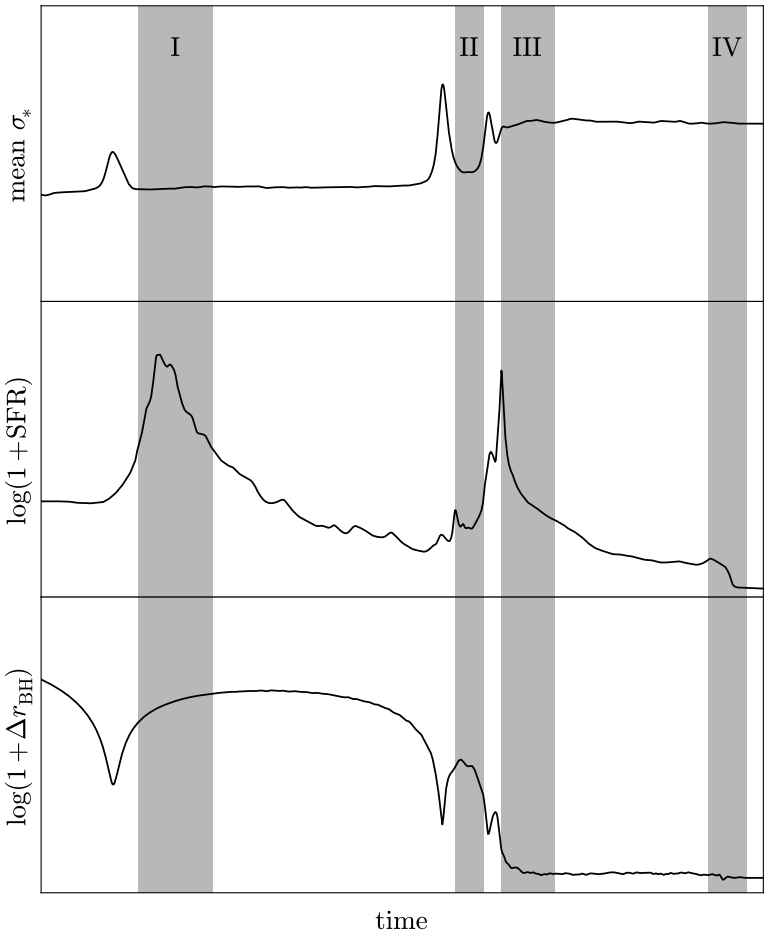

Figure 3.8: Periods of significant accretion during a generic merger. All significant accretion (with $L_{\mathrm{bol}} \gtrsim 10^{44}\,\mathrm{erg\ s^{-1}}$) occurred during one of four periods: (I) Shortly after the first pass, (II) between the second and third passes, (III) during and immediately following nuclear coalescence, and (IV) long after nuclear coalescence. Not all mergers exhibited significant SMBH accretion during all four periods.

each of the four quasar periods. There was no detectable offset in σ_* during periods I, III, and IV, however an offset was always present during period II. Since the fiducial value of σ_* during period II is somewhat ambiguous, we computed two mean fractional offsets: the offset from the progenitor system, $(\sigma_* - \sigma_{\rm prog})/\sigma_{\rm prog} = 0.11 \pm 0.05$, and the offset from the final remnant system, $(\sigma_* - \sigma_{\rm final})/\sigma_{\rm final} = -0.28 \pm 0.02$. Due to these offsets, the inclusion of period II quasar host galaxies in an observational sample could potentially introduce extra scatter, or an offset, in a plot of the $M_{\rm BH}$–σ_* relation. In Figure 3.8, we see that the SMBHs are significantly separated during period II. Therefore, a measurement of $M_{\rm BH}$ in such a system would correspond with the mass of a *progenitor* SMBH. The fiducial value of σ_* used in the $M_{\rm BH}$–σ_* relation would then be the *pre-merger* value of the progenitor spheroid. If we assume that progenitor systems generally fall within the scatter of the local $M_{\rm BH}$–σ_* relation, then observations of period II systems would tend to have high values of σ_* relative to their $M_{\rm BH}$. Stated differently, these systems would appear to have under-massive black holes when placed on the $M_{\rm BH}$–σ_* diagram. Thus, the overly massive black holes that are observed at high redshift cannot be due to measurements of period II systems. Furthermore, in our simulations, period II quasar activity accounted for only 16.1% of all quasar-level AGN activity; it is unlikely that a large fraction of randomly selected quasar hosts would consist of period II systems. Finally, from the images of the period II system (snapshot *e*) in Figure 3.2, it is evident that period II systems are composed of two distinguishable galaxies (when viewed along most lines of sight), so they should be relatively easy to identify.

When interpreting these results, one should be aware that the timing of quasar activity depends upon the treatment of hydrodynamics and SMBH feedback in our simulations. We have tried to make our results more robust by considering only the general periods of likely accretion, rather than the exact timing of the accretion. However, recent work by Hayward et al. (2013) suggests that the hydrodynamic evolution in the late stages of GADGET-3 simulations can differ significantly from the evolution observed in more realistic simulations when SMBH feedback is included. This casts some doubt on the timing and prevalence of Period IV quasars, but our general finding remains unchanged; during a period of quasar activity, σ_* is not likely

to be strongly offset from its fiducial value. Even if Period IV quasars *never* occur in nature, the majority of quasar activity still occurs during periods when σ_* is not significantly offset. Alternatively, if Period IV accretion is more likely in reality than our simulations suggest, then observing a quasar host with an elevated velocity dispersion would be more rare than our simulations suggest, since Period IV quasars occur after the σ_* has reached a stable value.

3.4.2 Intrinsic Scatter

Measurements of σ_* in real galaxies are necessarily made from random viewing directions at random times during galactic evolution. There is no way of observationally determining the intrinsic scatter of σ_* with respect to its quiescent, fiducial value. Using our simulation data, we are able to provide estimates of this intrinsic scatter. Since observed systems can broadly be categorized as either ongoing mergers or passively evolving (or simply "passive") systems, we present two intrinsic scatter estimates—one for passive systems and one for ongoing mergers. In this analysis, three conditions must be met for a galaxy to be considered passive:

1. The galaxy must be clearly distinguishable from neighboring galaxies.
2. The galaxy must contain only one nucleus.
3. The galaxy must contain at most one large disk structure.

If any of these general criteria are not met, then the system is considered an ongoing merger. Passive systems include all systems that appear to be non-interacting as well as systems that have clearly undergone recent interactions. For example, even though the progenitors in simulation S1 show strong signs of interaction after the first pass (see snapshot *b* in Figure 3.2), we classify them as passive galaxies between approximately 0.5 Gyr and 2.0 Gyr. The system is also classified as passive immediately after nuclear coalescence, at 2.4 Gyr, even though there are signs of recent interaction, such as stellar shells (see snapshots *g* and *h*). We classify simulation S1 as an ongoing merger between 2.0 Gyr and 2.4 Gyr (snapshots *c–f*) and also during the first pass, between approximately 0.25 Gyr and 0.4 Gyr. Admittedly, there are special circumstances

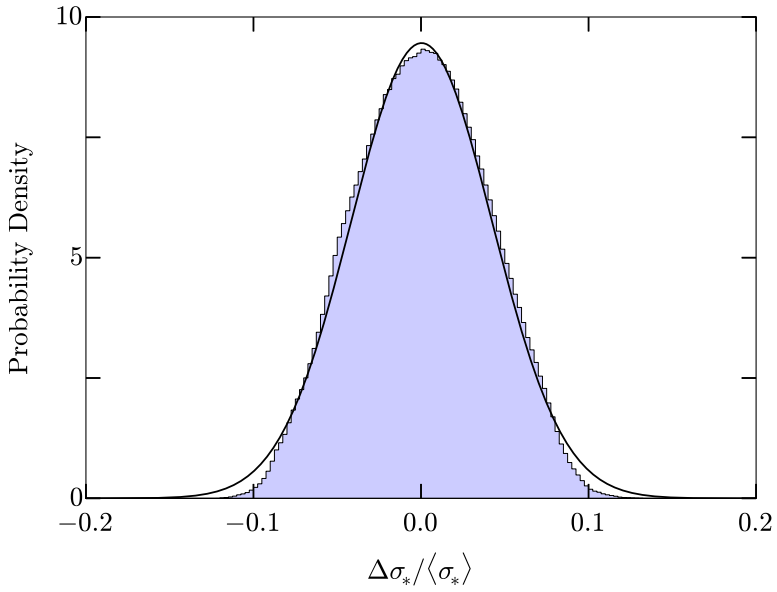

Figure 3.9: Scatter probability distribution for coalesced systems, where $\Delta\sigma_*$ is the offset from the mean value of stellar velocity dispersion, $\langle\sigma_*\rangle$. This plot includes data from all snapshots (i.e., from all simulations) saved during periods of passive evolution, as defined in section 3.4.2. The best-fitting Gaussian, with $\sigma = 0.042$ and $\mu = 1.25 \times 10^{-5}$ is over-plotted.

that can cause an ongoing merger to *appear* to be a passive system and vice versa. In this chapter, we have ignored these effects.

Upon separating each merger simulation into periods of ongoing merger activity and periods of passive evolution, we computed the probability distribution of the fractional offset, $\Delta\sigma_*/\langle\sigma_*\rangle$ from the fiducial value. The quantity $\Delta\sigma_* = \sigma_* - \langle\sigma_*\rangle$ is the offset from the current fiducial value, $\langle\sigma_*\rangle$. In the passive period after the first pass, the fiducial value is the time average of the mean σ_* time series during that period. In all other cases, the fiducial value is the time average of the mean σ_* time series in the remnant system, σ_{final}. In Figure 3.9, we present the probability distribution for passive systems. This plot contains data from all of our simulations. The best fitting elementary distribution (in the least squares sense) was the Gaussian,

$$\frac{dP}{ds} = \frac{1}{\sigma\sqrt{2\pi}} \exp\left[-\frac{(s-\mu)^2}{2\sigma^2}\right] \tag{3.5}$$

with $\sigma = 0.042$ and $\mu = 1.25 \times 10^{-5}$. The corresponding plot for ongoing mergers is presented in Figure 3.10. The best fitting elementary distribution in this case was the shifted log-normal

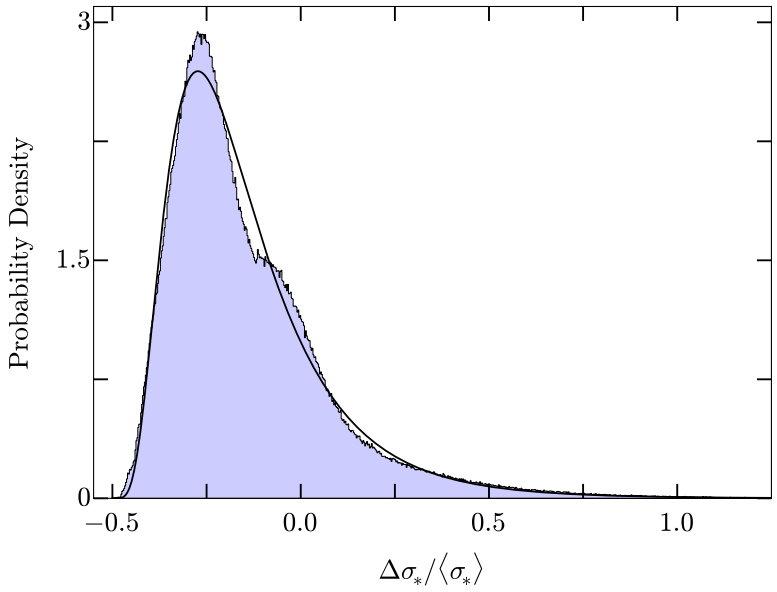

Figure 3.10: Scatter probability distribution for merging systems, where $\Delta\sigma_*$ is the offset from the mean value of stellar velocity dispersion of the final remnant, $\langle\sigma_*\rangle = \sigma_{\rm final}$. This plot includes data from all snapshots (i.e., from all simulations) saved between the onset of the second pass and nuclear coalescence. The best-fitting log-normal distribution, with $\sigma = 0.543$, $\mu = -1.150$, and $\delta = -0.509$, is over-plotted.

distribution,

$$\frac{dP}{ds} = \frac{1}{\sigma\sqrt{2\pi}(s-\delta)} \exp\left[-\frac{[\ln(s-\delta)-\mu]^2}{2\sigma^2}\right] \tag{3.6}$$

with $\sigma = 0.543$, $\mu = -1.150$, and $\delta = -0.509$. In both cases, the distribution is more closely fit by a linear combination of Gaussians; the above approximations are presented for simplicity. Using these densities, we can easily compute various probabilities. For example, in the absence of measurement error, the probabilities of measuring σ_* within 5% of the fiducial value (i.e., $\sigma_{\rm final}$) are, respectively, 0.77 and 0.10 for passive systems and ongoing mergers. Furthermore, the probability of measuring σ_* lower than the fiducial value ($\sigma_{\rm final}$) in an ongoing merger is 0.81.

While our approximation for the intrinsic scatter in passively evolving systems is likely fairly robust, the approximation for ongoing mergers likely depends more heavily upon our merger parameters. Given the characteristic directional distribution of σ_* during a merger

(see Figure 3.4) and the temporal evolution (see Figure 3.1), it is clear that the distribution is strongly skewed, like the log-normal distribution presented above. However, a greater variety of mergers would need to be examined in order to confidently compute the parameters of the distribution in ongoing mergers.

3.5 Discussion and Conclusions

In this chapter, we have expanded upon the work presented in Chapter 2 by examining the evolution of stellar velocity dispersion in a suite of eight binary disk galaxy merger simulations that included dissipation, dark matter, star formation, and AGN feedback. The analysis was designed, in part, to provide insight into observations of σ_* in systems that show signs of recent or ongoing merger activity. Our primary findings are as follows:

1. During each merger, before the galactic nuclei coalesced, σ_* underwent large, damped oscillations of increasing frequency. Once the nuclei coalesced, a series of small, statistically significant fluctuations continued until the remnant system became sufficiently mixed. Qualitatively, this behavior is consistent with the findings of Chapter 2, which examined the evolution of σ_* in more idealized mergers of spherically symmetric, dissipationless systems that did not contain a separate dark matter component.

2. Varying the gas fraction, and orbital parameters had no effect on the qualitative shape of the σ_* evolution time series. Increasing the gas fraction merely increased the noisiness of the time series, due to the formation of larger numbers of tidal dwarf galaxies; each tidal dwarf introduced fine structure to the σ_* time series, which appears as noise.

3. Mergers of larger mass ratio (i.e., major mergers) exhibited the most significant absolute fluctuations in σ_*. However, the *relative* size of the fluctuations was not sensitive to the mass ratio. To see this, refer to the data from simulations S1, S4, and S5 in Table 3.3. These were, respectively, 1:1, 1:2, and 1:4 mergers with otherwise identical initial pa-

rameters. The value of σ_* at the climax of the second pass (σ_2), was highest in S1 and lowest in S5, however, there was no trend in the fractional increase, $\sigma_2/\sigma_{\rm final}$.

4. When σ_* is measured in systems that contain two progenitors moving relative to one another along the line of sight, the resulting measurements are artificially elevated because the streaming motion of the progenitors is mistaken for velocity dispersion. Equation 3.3 relates the apparent velocity dispersion of the combined system with the relative line-of-sight velocity and instrinsic properties of the progenitor systems.

5. During galaxy collisions, σ_* increases in all directions. The enhancement in σ_* is greatest along the collision axis, partially because the bulk motion of the two progenitor systems can be mistaken for true velocity dispersion, as noted above. Conversely, the enhancement is lowest along lines of sight perpendicular to the collision axis. The mean of σ_* over the set of all possible viewing directions closely traces the intrinsic velocity dispersion of the system.

6. Stars in our simulations were born with lower σ_* than that of the system as a whole. The apparent velocity dispersion of the youngest stars in the nuclear disks of our remnant systems was lower than the global stellar velocity dispersion by an average of ≈ 30 km s^{-1}. New stars tended to become dynamically heated with time unless they were tightly bound into clusters or dwarf galaxies. The velocity dispersion of stars residing in dwarf galaxies *decreased* with respect to the global system as the orbits of their parent systems decayed due to dynamical friction.

7. Quasar-level accretion activity was not detected during times when σ_* was strongly enhanced. On the other hand, Seyfert-level accretion occurred sporadically at all times after the first pass. In general, AGN activity does not preferentially occur when σ_* is strongly offset from its fiducial, equilibrium value. This is consistent with recent observational evidence (Woo et al., 2013), indicating that active galaxies fall on the same $M_{\rm BH}$–σ_* relation as quiescent galaxies.

Given our findings, we would advise anyone who is interested in measuring σ_* in a dynamically questionable system to note the following:

- When σ_* is measured in systems which clearly contain two nuclei, the resulting value of σ_* in the individual nuclei depends upon the nuclear separation distance. Nuclei that are significantly separated (e.g., snapshot *e* in Figure 3.2) are likely to retain a value of σ_* that is only slightly elevated with respect to the pre-collision value of the progenitor (compare the histograms for progenitor A and snapshot *e* in Figure 3.4). As the distance between the nuclei decreases, σ_* increases. When the nuclei are strongly superposed, as in snapshot *c*, the measured value of σ_* is likely to be higher than the value of σ_* in the eventual remnant system. Of course, projection can also cause significantly separated nuclei to appear to be significantly superposed, so significant nuclear superposition is a weak diagnostic.

- A measurement of σ_* is likely to be elevated relative to the eventual remnant value if the system contains two or more disk-like structures, but only one visible nucleus, as seen in snapshot *c* of Figure 3.2 (viewed along the $\theta = 75°$, $\phi = 66°$ direction).

- Measurements of σ_* in systems that contain only one nucleus are likely robust if the system also contains stellar shells or exhibits a dynamically relaxed morphology (see snapshot *h*). Shells tend to form *after* σ_* has reached its stable post-merger value. More generally, if a system appears to be dynamically relaxed, a measurement of σ_* is likely robust; the presence of low-surface brightness debris in the region surrounding a galaxy that otherwise appears to be relaxed does not indicate that σ_* is enhanced.

- Measurements of σ_* in the bulge components of disk-like systems containing strong bridges or tidal tails (e.g., snapshot *b*) are not likely to differ from the value of σ_* measured in the bulge before the interaction took place.

- Systems with quasar-level luminosities ($L_{\rm bol} \gtrsim 10^{44}\,{\rm erg\ s^{-1}}$) are unlikely to have substantially elevated or suppressed values of σ_*, relative to the fiducial, equilibrium value.

For a concrete example, consider the prototypical ongoing merger, NGC 6240. This system contains two nuclei with a projected separation of $\sim$ 800 pc. Using the guidelines outlined above, we would expect the velocity dispersion of each progenitor nucleus to be mildly elevated with respect to its pre-merger value since two nuclei are visible, but they are not separated by a large distance. Medling et al. (2011) measured σ_* and $M_{\rm BH}$ in the southern nucleus of NGC 6240 and found that the nucleus lies within the scatter of the $M_{\rm BH}$–σ_* relation. Assuming that (1) the nucleus was on the relation before the merger began and (2) the SMBH has not grown substantially since the beginning of the merger, then this finding is consistent with what we expect. However, note that the measurement of $\sigma_* = 282 \pm 20$km s^{-1} by Medling et al. (2011) was based upon the dynamics of the CO bandheads of later-type giants and supergiants within 300 pc of the southern black hole, so the measurement may be lowered due to the presence of a dynamically cool nuclear disk. Also, if NGC 6240 were placed at sufficiently high redshift, or the observations were of lower resolution, the two nuclei would not have been distinguishable. In this situation, we would only be able to classify NGC 6240 as a generic ongoing merger. Based upon the scatter analysis of Section 3.4.2, we see that a measurement of σ_* in such a system is 81% likely to be lower than the value of σ_* in the relaxed remnant (with the most likely measurement being 27% lower than the final value). Oliva et al. (1999) measured σ_* of the entire merging system using the Si 1.59 μm, CO 1.62 μm, and CO 2.29 μm lines, obtaining measurements of 313 km s^{-1}, 298 km s^{-1}, and 288 km s^{-1}, respectively. These measurements of σ_* place the southern black hole, together with the σ_* of system as a whole, within scatter of the local $M_{\rm BH}$–σ_* relation. Once the two progenitor SMBHs merge, we would expect σ_* to increase in order for the system to remain on the $M_{\rm BH}$–σ_* relation; this is consistent with our expectation that a measurement of σ_* in NGC 6240 is likely to be lower than that of the eventual remnant.

The reader should be aware that the conclusions above were based upon a fairly small number of simulations which were performed using an imperfect simulation code. While several initial conditions were independently varied, extreme cases were not tested. The simulations did not have sufficient resolution to follow the evolution of individual stars or the detailed

structure of the multi-phase interstellar medium. It should also be noted that the recipes used for star formation and SMBH feedback were very crude and cannot be expected to faithfully represent reality. Furthermore, all measurements of σ_* in this chapter were mass-weighted. In order for this work to be more relevant to observational studies, we need to know whether mass-weighted determinations of σ_* are consistent with the flux-weighted measurements that are performed during observations of real galaxies. In Chapter 2, we showed that, in principle, flux-weighted σ_* can differ from mass-weighted σ_* in the presence of dust extinction. In the simulations of the present chapter, we have seen that the intrinsically more luminous new star particles tend to be dynamically cooler than the older population of less luminous particles. In the next phase of this research (N. R. Stickley et al., in preparation), we plan to characterize potential differences between flux-weighted and mass-weighted determinations of σ_* by creating synthetic Doppler-broadened spectra, generated using the kinematics feature of the radiative transfer code, SUNRISE (Jonsson, 2006; Jonsson et al., 2010; Jonsson and Primack, 2010). This will allow us to characterize the effect of dust attenuation on measurements of σ_* in a much more realistic manner than previously done in Chapter 2.

Chapter 4

Flux-Weighted Velocity Dispersion

Abstract

Using virtual observations of spectra emitted by simulated galaxies, we investigate the differences between flux-weighed and mass-weighted velocity dispersion measurements in systems with recent or ongoing star formation. We find that the presence of dust typically causes flux-weighted measurements of stellar velocity dispersion to be elevated with respect to mass-weighted measurements. This is because dust preferentially obscures young stars, which tend to be dynamically cooler than older stellar populations. On the other hand, flux-weighted measurements that do not include dust attenuation tend to be negatively offset with respect to mass-weighted measurements because the young stellar populations are more luminous per unit mass than older stellar populations. Exceptions to these trends are discussed. Additionally, we find that the total degree of dust attenuation is less important than the distribution of the dust with respect to the young stars in the system.

4.1 Introduction

In order to maximize the usefulness of any simulation, there must be reliable methods for comparing the simulation with reality. In this chapter, we work toward improving the techniques used to compare the simulated and real versions of an important quantity in galactic astronomy—the line-of-sight stellar velocity dispersion (σ_*).

Observationally, σ_* can only be measured by analyzing the light emitted by a galaxy. This is an inherently flux-weighted measurement method. In contrast, the natural way of measuring σ_* in a numerical simulation involves using the velocity and mass data in the simulation to compute a mass-weighted velocity dispersion. If real galaxies consisted of stars with a uniform mass-to-light ratio (Υ) and contained no gas nor dust, observations of σ_* should agree perfectly with the quantity computed from simulation data. In reality, galaxies are not so simple; they typically contain a broad variety of stars and at least a small amount of dust. In Chapter 2, we saw that including a toy model for dust attenuation—a uniformly dense slab of attenuating material—could cause a decrease in the flux-weighted velocity dispersion ($f\sigma_*$), relative to the mass-weighted velocity dispersion ($m\sigma_*$) in a simulated galaxy. Unlike our toy model, real interstellar dust is quite non-uniformly distributed; it occurs in clumps, sheets, and filaments as well as in a more diffuse state. It is not clear how a realistic dust distribution would effect the value of $f\sigma_*$.

In Chapter 3, we found that velocity dispersion measurements based upon newly-formed stars in numerical simulations were significantly lower than the velocity dispersion of the system as a whole. This is consistent with the observations of the so-called "σ_* discrepancy" (Rothberg and Fischer, 2010; Rothberg et al., 2013), in which different stellar populations in the a single galaxy yield discrepant values if σ_*. Since young stellar populations are more luminous per unit mass (i.e., have smaller Υ), the presence of young stars may weight the value of $f\sigma_*$ downward relative to $m\sigma_*$.

In this chapter, we examine the differences between measurements of $f\sigma_*$ and $m\sigma_*$ using a considerably more realistic technique than the one employed in Chapter 2. Beginning with the

detailed numerical simulations described in Chapter 3, we have generated synthetic, Doppler-broadened spectra that include the effects of dust attenuation and stellar evolution. We analyze the resulting spectra in order to measure $f\sigma_*$. By comparing $f\sigma_*$ with $m\sigma_*$, we are able to gain insights into the differences between the version of σ_* measured observationally and the version that is reported in the galaxy simulation literature.

4.2 Methodology

4.2.1 Numerical Simulations

For the present work, we have used simulation snapshots from merger S1 of Chapter 3. Since the details of this simulation have already been discuss in detail in Chapter 3, we will only summarize the key features here; refer to Chapter 3 for the full details of the simulation.

The simulation was a binary, 1:1 mass ratio, prograde-prograde merger of disk galaxies. It was performed using the N-body, SPH code, GADGET-3 (Springel, 2005). Each progenitor consisted of 1.6×10^6 particles. Eighty percent of the disk mass of each progenitor galaxy initially consisted of stars with the other 20% in the form of gas and dust. The gravitational softening length of stars was 25 pc, meaning that physical processes on scales smaller than 25 pc could not be resolved. Each stellar particle in the simulation represented a population of stars, rather than actual individual stars. The interstellar medium was modeled as a multi-phase gas with hot and cool phases. Hot gas was able to cool radiatively and cool gas was able become heated by stellar feedback and AGN feedback to become hot gas. A sub-resolution approximation was used to include stellar formation in the simulation; new stellar particles were spawned in cool, dense regions of gas at a rate designed to match observational evidence. As stars evolved and added metals to the ISM, the metallicity of the gas increased. Each stellar particle that formed during the simulation carried a variable specifying its creation time and metallicity. The latter was set equal to the metallicity of the gas from which the particle was spawned.

4.2.2 Mass-Weighted Velocity Dispersion

The mass-weighted velocity dispersion ($m\sigma_*$) was computed with GSNAP[1] (N.R. Stickley, in preparation), using the same technique described in Chapters 2 and 3. In summary, a virtual rectangular slit of width $w = 2$ kpc and length $\ell = 20$ kpc was placed on the galaxy of interest. A viewing direction, (θ, ϕ) and slit position angle α, were then specified. The masses and velocities of all stars appearing in the slit were used to compute $m\sigma_*$, according to

$$m\sigma_* = \sqrt{v_i^2 m_i/M - (v_i m_i/M)^2} \tag{4.1}$$

with

$$M = \sum_i m_i$$

where the standard summation convention has been utilized; repeated indices imply a sum over that index. Using this technique allowed us to directly compare the present work with the results presented in Chapter 3. The primary source of uncertainty in this measurement was particle noise, which never exceeded 0.9% of the measured value.

4.2.3 Flux-Weighted Velocity Dispersion

In order to perform flux-weighted measurements of σ_* in galaxy simulations, we first obtained synthetic Doppler-broadened spectra. We then analyzed these spectra to determine σ_*. In this section, we describe the process that was used to obtain and analyze the synthetic spectra.

Simulated Spectra

Synthetic, Doppler-broadened galaxy spectra were generated using the polychromatic, Monte Carlo, radiative transfer code, SUNRISE (Jonsson, 2006; Jonsson et al., 2010; Jonsson and Primack, 2010). The code is capable of creating realistic images of galaxies from arbitrary viewing directions. More importantly, SUNRISE can compute a high resolution spectrum for each pixel of each image that it generates.

[1] http://www.gsnap.org

Given a GADGET-3 snapshot file, SUNRISE began by discretizing the spatial domain of the simulation using an adaptive mesh. A Monte Carlo radiative transfer algorithm was then performed on the discretized volume. The algorithm assumed that the dust content of the ISM was proportional to the metallicity of the SPH particles in the simulation snapshot file. In this work, we assumed that 40% of the metals in the ISM occurred in the form of dust. Because the stellar particles in our galaxy simulation represented entire stellar populations, rather than individual stars, each stellar particle in SUNRISE emitted a spectrum corresponding to a population of stars. These spectra were pre-computed using STARBURST99 (Leitherer et al., 1999). Since GADGET-3 simulations only track the ages and metallicities of stellar particles that formed during the simulation, we manually assigned ages and metallicities to the pre-existing stellar particles; all particles were assumed to form instantaneously, 3 Gyr before the beginning of the simulation with a metallicity of $Z = 0.025$, which is approximately 1.25 $Z_{\odot}$. SUNRISE treats stellar particles younger than 10 Myr as active star forming regions containing enhanced dust concentrations and a photodissociation region. These star-forming regions are modeled using the code, MAPPINGSIII (Dopita et al., 2005; Groves et al., 2008). It is also possible to include AGN emission in the radiative transfer simulation, however we did not enable this feature.

Using the stellar spectra and the spatial distribution of stars and dust, SUNRISE computed dust attenuation and scattering of stellar radiation using 10^7 "photon bundles." Each photon bundle carried wavelength-flux data on a random walk through the simulated galaxy and accounted for Doppler shifts due to stellar motion. The bundles were eventually collected by a virtual integral field spectrograph. The individual Doppler shifts led to Doppler-broadened spectra. In addition to storing the dust-attenuated spectral information for each pixel of the generated image, SUNRISE stored the unattenuated spectra, which allowed us to clearly identify the effect of attenuation in each virtual observation.

Besides the galaxy simulation snapshot file and the input spectra, the other main user input to the code was the choice of dust model (i.e., the dust grain size distribution and albedo). For this work, we used the Milky Way dust model from Weingartner and Draine (2001). It should be noted that the dust model used by SUNRISE significantly effects the final spectrum of the

simulated galaxy (Jonsson et al., 2010).

The radiative transfer computation required a large amount of memory, partially owing to the fact each photon bundle carried a detailed spectrum. In order to reduce the memory requirement and accelerate the computation, we limited our spectral coverage to the Mg Ib region, from 5040 Å to 5430 Å. Our input stellar spectra contained 1170 wavelength bins in this region, logarithmically spaced. Once SUNRISE had finished generating synthetic spectra for the individual pixels of each image, we placed a rectangular slit, measuring 2×20 kpc, on the image. The spectra of all pixels appearing within the slit were then combined to form a single spectrum. This combined spectrum was analyzed in order to determine the flux-weighted velocity dispersion ($f\sigma_*$).

Measuring Velocity Dispersion from Spectra

Stellar velocity information is encoded in all galaxy spectra, since the light emitted by a galaxy consists of the sum of the Doppler shifted spectra of its constituent stars. Similarly, each of our synthetic spectra consisted of a sum of Doppler-shifted particle spectra. In order to decode the spectra and recover the velocity information, we used the penalized pixel-fitting code, pPXF, written by Cappellari (Cappellari and Emsellem, 2004; Cappellari, 2012). In general, the pPXF algorithm worked by fitting a parameterized model spectrum, $G_{\rm mod}(x)$, to an observed galaxy spectrum, $G(x)$. One of the parameters of $G_{\rm mod}(x)$ was $f\sigma_*$. Thus, $f\sigma_*$ was ultimately determined by finding the model spectrum that best fit each galaxy spectrum.

More specifically, the model spectrum was a linear combination of template spectra convolved with a parameterized line of sight velocity distribution (LOSVD):

$$G_{\rm mod}(x) = \sum_{k=1}^{K} w_k [B * T_k](x) + \sum_{l=0}^{L} b_l \mathbb{P}_l(x) \qquad (w_k \geq 0), \tag{4.2}$$

where w_k are weights, $B(x) = \mathbb{L}(cx)$ is a broadening function, with $\mathbb{L}(v)$ the LOSVD, c is the speed of light, T_k is a library of template spectra, and $*$ denotes convolution. The linear

combination of Legendre polynomials, $\mathbb{P}_l(x)$ (with weights b_l) was used to account for low-frequency differences between the shape of the templates and the shape of the galaxy spectrum.

The LOSVD was expanded as a Gauss-Hermite series,

$$\mathbb{L}(v) = \frac{\exp(-y^2/2)}{\sigma\sqrt{2\pi}} \left[1 + \sum_{m=3}^{M} h_m H_m(y)\right], \tag{4.3}$$

where H_m are Hermite polynomials, $y \equiv (v - V)/\sigma$, and $(V, \sigma, h_3, h_4, \ldots, h_M)$ are free parameters related to the moments of the velocity distribution. For example, V is the mean line-of-sight velocity, σ corresponds to the standard deviation (i.e., $f\sigma_*$), h_3 is related to the skewness, and h_4 is related to the kurtosis. Optimal values for these parameters, as well as the weights, w_k and b_l, were found using a nonlinear least-squares minimization algorithm.

The quantity minimized by the least-squares optimization routine was the objective function:

$$\chi^2_{\rm p} = \chi^2(1 + \lambda^2\mathbb{D}^2), \tag{4.4}$$

where χ^2 is given by

$$\chi^2 = \sum_{n=1}^{N} \left[\frac{G_{\rm mod}(x_n) - G(x_n)}{\Delta G(x_n)}\right]^2, \tag{4.5}$$

with $\Delta G(x_n)$ the measurement error on $G(x_n)$. The $\mathbb{D}^2$ in Eq. (4.4) is a penalty term, given by the integrated square deviation of $\mathbb{L}(v)$ from its best-fitting Gaussian, $\mathbb{G}(v)$,

$$\mathbb{D}^2 = \frac{\int_{-\infty}^{\infty} [\mathbb{L}(v) - \mathbb{G}(v)]^2 {\rm d}v}{\int_{-\infty}^{\infty} \mathbb{G}^2(v) {\rm d}v} \tag{4.6}$$

The penalty term clearly increases as $\mathbb{L}(v)$ deviates from a pure Gaussian, thus, it has the effect of forcing the fitting routine to favor LOSVDs that are more nearly Gaussian. The parameter, λ, was a user-specified quantity that allowed us to adjust the importance of the penalty term. Setting $\lambda = 0$ caused the best-fitting LOSVD to be a general Gauss-Hermite series. Increasing λ resulted in LOSVDs that were more nearly Gaussian. When dealing with noisy spectra, obtained observationally, non-zero values of λ are often used in order to force the fitting routine to favor

Gaussian LOSVDs. This helps pPXF to partially ignore the effect of noise in the spectra in cases for which the true LOSVD is Gaussian (Cappellari and Emsellem, 2004). Our spectra did not include the sort of noise that is present in real (i.e., observed) spectra, but we adjusted λ nonetheless in order to examine the full range of velocity dispersions that could be obtained using our spectra. Specifically, we set $\lambda = 0$ to determine the value of $f\sigma_*$ that would be measured by a researcher who prefers to approximate their LOSVDs using a Gauss-Hermite series. We also set $\lambda = 10^6$ in order to determine the value of $f\sigma_*$ that would be reported by a researcher who prefers to use simple Gaussian LOSVDs.

We constructed a template library using a subset of the raw spectra emitted by the stellar particles in the SUNRISE computation. The template library was gradually expanded to include more spectra until the effect of adding additional spectra no longer significantly effected the χ^2 of the resulting fits. In total, 67 template spectra were included in the library. For the measurement error, $\Delta G(x_n)$, we assumed a uniform value for each wavelength bin in the spectrum. Specifically, we set each entry equal to 1% of the mean signal strength (i.e., $\Delta G(x_n) = 0.01\langle G\rangle$, for all n). This had no effect on the resulting values $f\sigma_*$; it merely determined the magnitude of the formal measurement uncertainty.

4.2.4 The Comparison Technique

Each virtual observation was performed using a virtual integral field spectrograph with a resolution of 400×400 pixels. The field of view of each array was 200 kpc, thus each pixel represented a 0.5×0.5 kpc region of the simulation. In order to compare the mass-weighted and flux-weighted velocity dispersions, we first verified that we were measuring the same region of the simulation snapshot using our two methods. The verification process involved comparing detailed images, generated by SUNRISE, with images generated using GSNAP's interactive particle visualization feature.

Once the location and orientation of the slits had been calibrated, there remained a mismatch between the sizes of the flux slit and the mass slit, due to the pixelated nature of the flux data. Pixels falling on the border of the slit typically extended outside of the slit. Thus, flux from

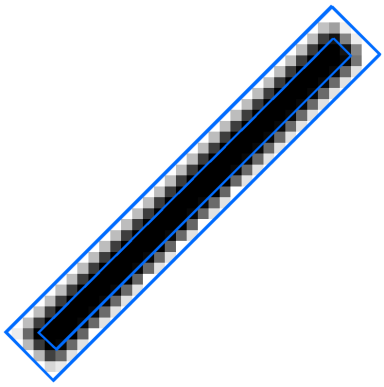

Figure 4.1: An illustration of the pixel-weighting scheme. White pixels indicate weights of zero while black pixels indicate weights equal to unity. Gray pixels on the edge of the slit are weighted intermediately. The blue rectangles indicate the smallest and largest slit sizes that were used when measuring $m\sigma_*$. The fiducial slit (not shown) lies mid-way between the blue rectangles.

a large region outside of the slit contributed to the measurement of $f\sigma_*$. To reduce this aliasing effect, we assigned weights to the pixels, depending on the degree of overlap with the slit. The result can be seen in Figure 4.2.4, where white corresponds to a weight of zero and black corresponds to a weight of unity. Edge pixels were weighted intermediately, so they appear as shades of gray. These weights were applied to the pixel spectra when the slit spectrum was computed. Furthermore, we varied the size of the mass slit in order to determine the maximum and minimum possible values of $m\sigma_*$ in the region that was measured by the flux-weighting method. The blue rectangles in Figure 4.2.4 indicate the smallest and largest slit sizes that were used during this process. In Section 4.3, we report the value of $m\sigma_*$ measured using the fiducial 2×20 kpc slit. We use the maximum and minimum values of $m\sigma_*$ over the full range of slit sizes as upper and lower bounds on the uncertainty whenever $m\sigma_*$ is compared with $f\sigma_*$.

4.2.5 Sample Selection

In general, our observations were chosen to include a mixture of extreme and ordinary situations. More precisely, snapshots that were known to exhibit extreme values of $m\sigma_*$ were included along with snapshots that were known to be in a dynamically relaxed state. Lines of sight known to have enhanced dust extinction (for instance, parallel to a disk of gas) were

included along with lines of sight with far less dust extinction (e.g., nearly perpendicular to disk structures). Intermediate cases were included as well.

A total of seven snapshots from the simulation were examined using our mass-weighted and flux-weighted velocity dispersion measurement methods. The first six of these were the snapshots labeled *c*–*h* in Chapter 3. These correspond to interesting points in the dynamical evolution of the merger. The seventh snapshot was the final snapshot of the simulation. For each snapshot, three virtual observations were performed using SUNRISE. Four slits were placed on each image—centered on the same pixel, but rotated uniformly about that pixel's center. In the remainder of this section we describe the 21 virtual observations.

Snapshot 1

This snapshot was recorded at $t = 2.06$ Gyr—immediately before the climax of the second pass. We knew from the analysis performed in Chapter 3 that the mass-weighted velocity dispersion reached its highest value during this stage of the merger. Consequently, this was a dynamically extreme system. The system contained two disks which were in the process of passing through one another. See Figure 4.2 for renderings of the system from the three camera positions.

Camera 1 was placed along a line of sight containing maximal dust attenuation. This line of sight fell approximately 27° away from the collision axis. Camera 2 was placed nearly perpendicular to the collision axis along a line of sight with minimal dust extinction. Camera 3 observed an intermediate configuration with a moderate amount of attenuation due to dust and a viewing angle 33° from the collision axis.

Snapshot 2

This snapshot was recorded at $t = 2.089$ Gyr. Dynamically, the system was still somewhat excited, having recently undergone a major collision. The system consisted of two clearly distinguishable, disturbed ellipsoids with extended disk debris.

Camera 1 was placed along a line of sight with a moderate degree of dust attenuation, 24° from the collision axis. Camera 2 was placed along a line of sight perpendicular to the collision axis with moderate attenuation. Camera 3 was placed approximately 5° from the collision axis.

Figure 4.2: GSNAP-generated renderings of Snapshot 1, viewed along the three camera directions that were examined. Each image represents a 100 × 100 kpc region. Green cross-hairs indicate the position of the center of the slits. The size and orientation of the slits is shown in the upper-left corner, for reference. The first column shows the system with all stars and dust dust attenuation included. The second column shows the system without dust attenuation. The third column shows only the stars that formed during the simulation, attenuated by dust. The fourth column shows the image in the third column in the absence of dust attenuation. The brightness scaling in all images is identical.

Figure 4.3: The same as Figure 4.2, but for Snapshot 2.

Attenuation was somewhat more significant in the Camera 3 observation than in the other two. A significant number of stars from both spheroids appeared in all slits of Cameras 1 and 3, whereas the slits used in the Camera 2 measurements primarily included stars belonging to only one of the ellipsoids. See Figure 4.3 for renderings.

Snapshot 3

This snapshot was recorded at $t = 2.181$ Gyr, approximately midway between the second and third passes of the merger process. The system consisted of two disturbed ellipsoidal galaxies. Both ellipsoids had nearly reached a dynamically stable state at this point. Enhanced star-formation, which was triggered during the second pass, was recently quenched by periods of quasar activity.

Figure 4.4: The same as Figure 4.2, but for Snapshot 3.

Cameras 1 and 2 were placed along lines of sight with moderate dust attenuation. Both sub-systems were clearly distinguishable from these camera positions. Camera 3 was placed along the line of sight connecting the two systems. Attenuation was more significant along this camera direction than along the first two camera directions. See Figure 4.4 for renderings.

Snapshot 4

This snapshot was recorded at $t = 2.299$ Gyr—the climax of the third pass. The two progenitor systems were fully superimposed; only one nucleus could be identified. Like Snapshot 1, this snapshot represented a highly unusual system, partially due to its elevated velocity dispersion but also because the system hosted a weak nuclear starburst with a star formation rate of $\sim 5\ \mathrm{M}_\odot\ \mathrm{yr}^{-1}$.

Figure 4.5: The same as Figure 4.2, but for Snapshot 4.

Cameras 1, 2, and 3 were positioned 29°, 38°, and 40° from the collision axis. Dust attenuation was moderate in all three cases. See Figure 4.5 for renderings.

Snapshot 5

This snapshot was recorded at $t = 2.401$ Gyr—the moment of nuclear coalescence. The majority of the merger's dynamical evolution was complete at this point. A nuclear starburst with a star formation rate of ~ 13 $M_\odot$ yr^{-1} was present. Major quasar activity began $\lesssim$5 Myr after this snapshot was recorded, causing a sharp decrease in the star formation rate. Therefore, this system was likely similar to some quasar host galaxies.

Since the system was nearly isotropic dynamically as well as in terms of its dust distribution, the camera positions were chosen essentially at random. We used a large angular separation

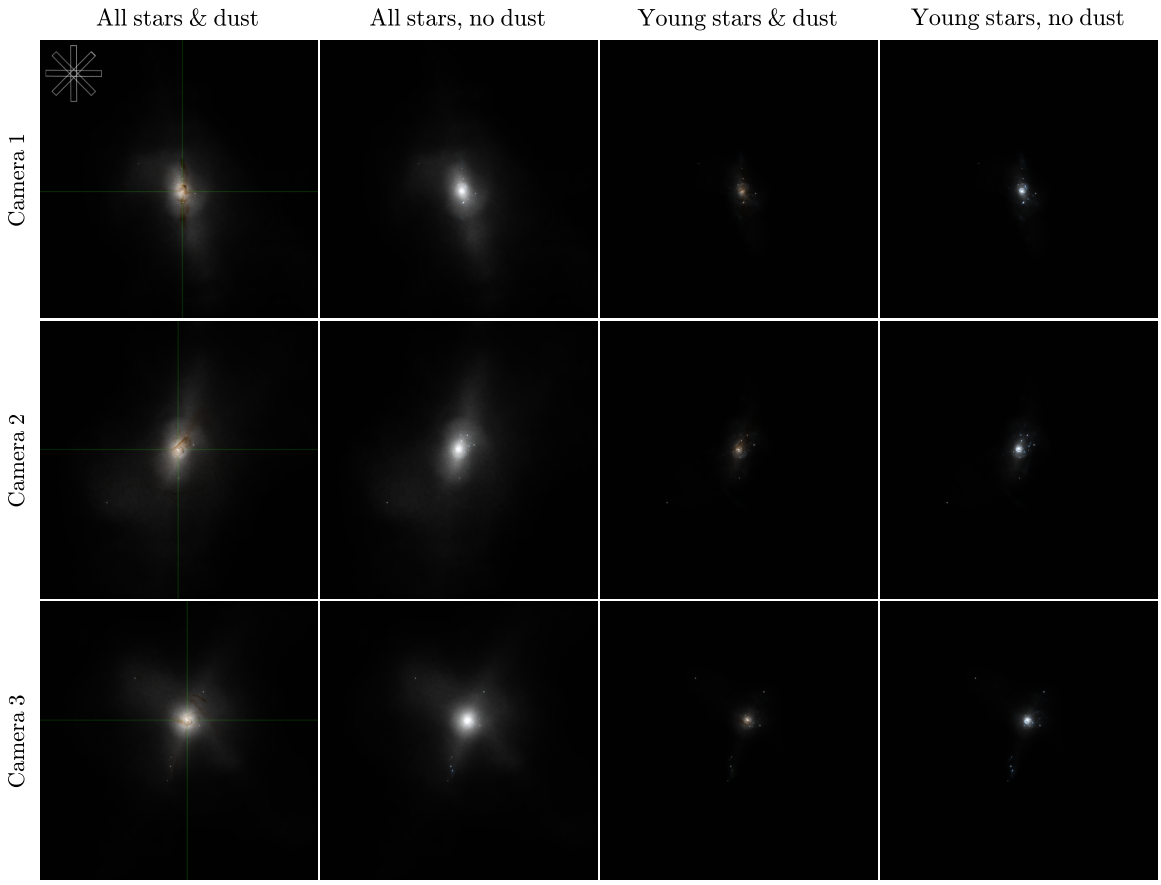

Figure 4.6: The same as Figure 4.2, but for Snapshot 5.

between viewing directions in order to prevent us from sampling the same regions of the simulation more than once. See Figure 4.6 for renderings of Snapshot 5.

Snapshot 6

This snapshot was recorded at $t = 2.690$ Gyr. The system exhibited shells and tidal debris in its outer regions. It also contained two non-coaxial, concentric nuclear disks with diameters of 0.3 kpc and 1.3 kpc. The inner disk was inclined 67° with respect to the outer disk.

Camera 1 was placed along a line of sight inclined $\sim 40°$ with respect to the direction defined by the intersection of the planes containing the two disks. This inclination angle was measured along a third plane that symmetrically bisected the system. In other words, the two disks were viewed from equal inclination angles. Camera 2 was placed such that both disks

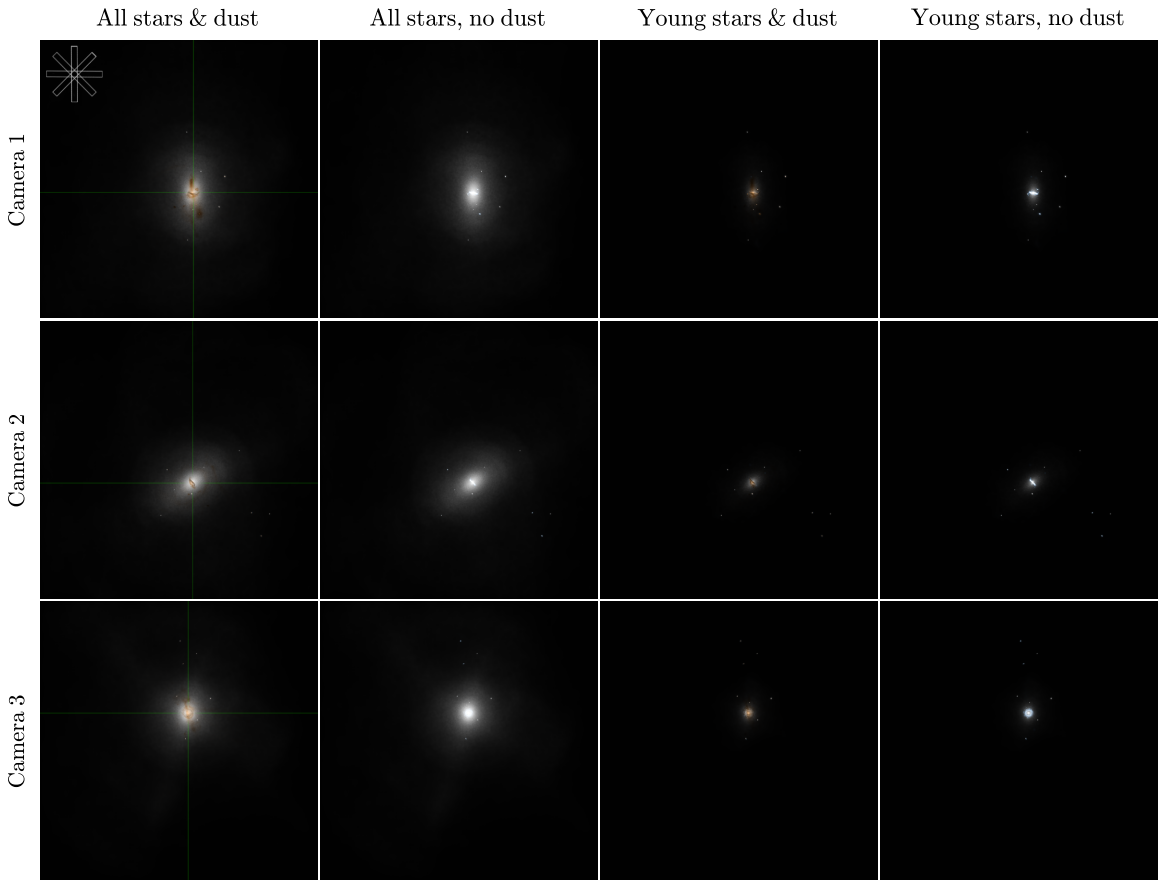

Figure 4.7: The same as Figure 4.2, but for Snapshot 6.

were viewed edge-on. Camera 3 was placed such that the larger disk was viewed edge-on. See Figure 4.7 for renderings.

Snapshot 7

This snapshot was recorded at $t = 3.62$ Gyr—the end of the simulation. This system consisted of an ellipsoidal galaxy containing three nuclear disks with diameters of 9.0 kpc, 1.5 kpc, and 0.3 kpc. It may be more appropriate to refer to the largest disk, as a "ring," considering its ring-like appearance in Figure 4.8.

Camera 1 viewed the large ring face-on; the intermediate disk was inclined $\sim 20°$ with respect to this line of sight. Camera 2 viewed the small inner disk edge-on. Camera 3 viewed the intermediate disk face-on. Cameras 2 and 3 respectively fell along lines of sight inclined

Figure 4.8: The same as Figure 4.2, but for Snapshot 7.

$\sim 20°$ and $\sim 23°$ with respect to the edge of the large ring.

4.3 Results

4.3.1 Overview

Figure 4.9 summarizes all of the velocity dispersion measurements performed on snapshots 1–7. Measurements of $m\sigma_*$ are shown as black boxes. Measurements of $f\sigma_*$ that assumed a pure Gaussian LOSVD, are plotted as blue circles. Measurements of $f\sigma_*$ that used the more general Gauss-Hermite series to model the LOSVD are plotted as red diamonds. Filled circles and diamonds indicate that the flux-weighted measurement was based on a spectrum that included dust attenuation. Open circles and diamonds indicate that dust was ignored when computing

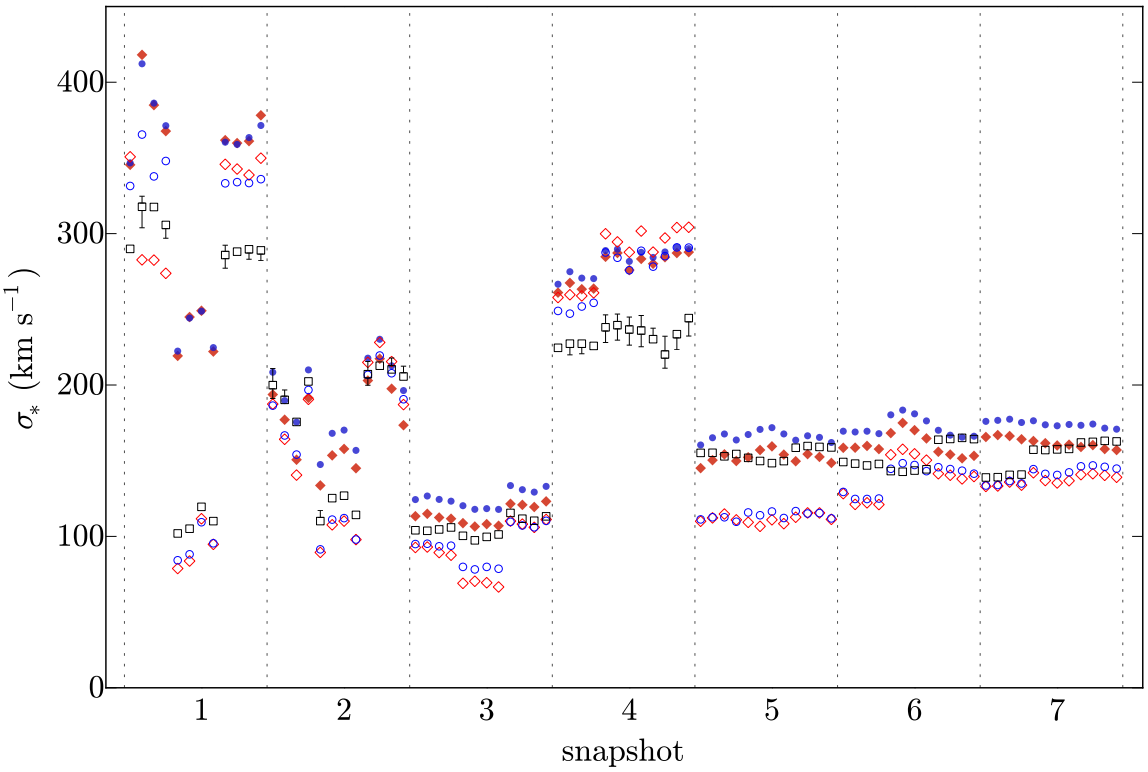

Figure 4.9: An overview of all velocity dispersion measurements performed on snapshots 1–7. Refer to Section 4.3.1 for the meanings of the symbols used in the plot.

the spectrum. Error bars are only included in the plot when the measurement uncertainty is larger than the plotted symbol (this plotting convention is used throughout this chapter). The horizontal axis indicates the snapshot number. Within each snapshot bin, there are three groups of four measurements. Counting from left to right, the first four measurements were made along the direction of Camera 1. The second four represent Camera 2 measurements, and the final four represent Camera 3 measurements.

In general, all measurement methods indicated that the velocity dispersion of the dynamically excited system in Snapshot 4 was elevated with respect to snapshots 3, 5, 6, and 7. It was also clear that the systems in snapshots 5–7 were very similar to one another. This was expected, since the merger remnant was passively evolving when the final three snapshots were obtained. In Figure 4.9, Snapshots 1 and 2 appear more complicated than the other snapshots. We discuss the reasons for this later in the chapter.

Several trends were apparent in the data. For instance, most flux-weighted measurements that assumed a Gaussian LOSVD fell above the corresponding measurement that used a Gauss-Hermite series to model the LOSVD. It was also clear that, in most cases, the $f\sigma_*$ measurements that included dust attenuation fell above $m\sigma_*$, while the non-attenuated $f\sigma_*$ typically fell below $m\sigma_*$. These trends are examined in the following sections.

4.3.2 Gaussian versus Gauss-Hermite Fitting Methods

Since researchers use different methods to extract the value of $f\sigma_*$ from real spectral data, we consider the differences between the two most common flux-based methods. As discussed previously, these two methods differ due to the assumed functional form of the LOSVD. On one extreme, a Gaussian LOSVD is assumed, on the other, a Gauss-Hermite series is used to model the LOSVD. We will use the symbol, $\hat{f}\sigma_*$ to denote the Gaussian method and $\tilde{f}\sigma_*$ to denote the Gauss-Hermite method.

In Figure 4.10, we plot the fractional offset between $\hat{f}\sigma_*$ and $\tilde{f}\sigma_*$. When dust attenuation was not included in the spectra, there was no measurable, systematic offset between the two methods. However, when dust attenuation was included, $\hat{f}\sigma_*$ exceeded $\tilde{f}\sigma_*$ by 9.8%, on average. This offset was not seen in Snapshot 1 and it was very small in Snapshot 4. Recall that both of these snapshots represented dynamically extreme systems in the midst of major collisions.

4.3.3 Mass-weighted versus Flux-weighted Measurements

Due to the inclusion of star formation in the simulation from which our snapshots were selected, the metallicities and ages of the stars in our snapshots varied significantly. This meant that the value of Υ varied. In order to identify the intrinsic differences between our flux-weighted and mass-weighted measurement techniques, we created simplified snapshots containing identical stars (i.e., stars with one specific value of Υ). If the two measurement methods were compatible with one another, then measurements of $f\sigma_*$ and $m\sigma_*$ in such systems should have agreed perfectly (within the measurement uncertainty) when dust attenuation is not included.

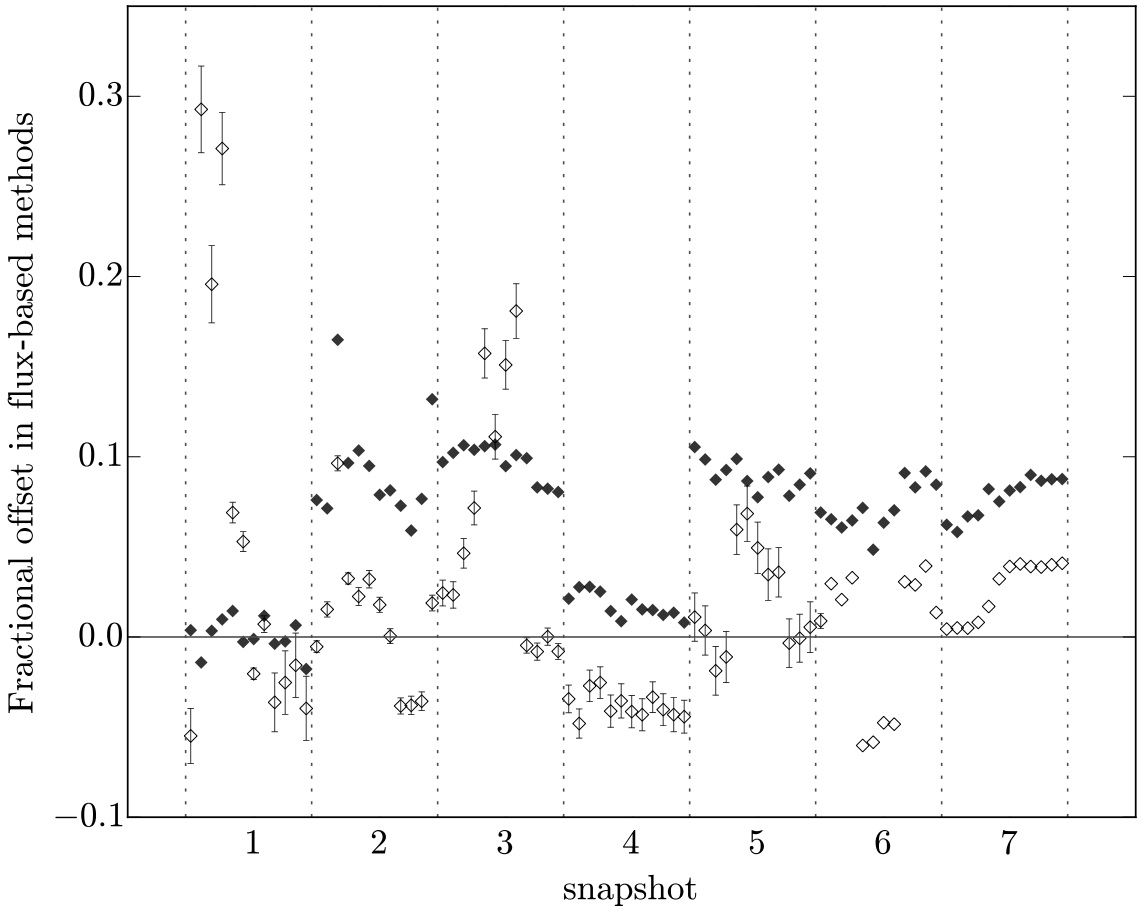

Figure 4.10: The quantity $(\hat{f}\sigma_* - \tilde{f}\sigma_*)/\tilde{f}\sigma_*$ for each measurement slit. This is the fractional offset between flux-weighted velocity dispersions measured under the assumption of a Gaussian LOSVD ($\hat{f}\sigma_*$) relative to those assuming a Gauss-Hermite LOSVD ($\tilde{f}\sigma_*$). When dust attenuation was included in the synthetic spectra (solid diamonds), the Gaussian model yielded larger velocity dispersions in all snapshots except for Snapshot 1. When dust attenuation was not included (open diamonds), there was no clear trend in the offset.

Upon comparing the two methods, we found that the flux-weighted measurement technique yielded values that were elevated with respect to the fiducial mass-weighted value by an average of 3.3% when a Gauss-Hermite LOSVD was used and 3.9% when a Gaussian LOSVD was used. After accounting for measurement uncertainty due to slit mismatch, these offsets fell by 1.3% to 2.0% and 2.6%, respectively. The maximum offset measured from the fiducial mass-weighted value was 6.0% (Gauss-Hermite) and 6.4% (Gaussian). No negative offsets were observed; flux-weighted measurements always agreed with or slightly exceeded the mass-weighted measurements. Given these findings, it appears that any positive offset greater than 6.4% in our observations is likely to be due to the effects of dust or non-uniform Υ. Any negative offset larger than the slit mismatch uncertainty is also likely due to these effects, rather than the intrinsic discrepancy between the two measurement methods.

In Figures 4.11 and 4.12, we compare $f\sigma_*$ with $m\sigma_*$ in our virtual observations. For the measurements that included dust, the mean fractional offset between flux-weighted and mass-weighted velocity dispersions, $(f\sigma_* - m\sigma_*)/m\sigma_*$, were respectively 0.21 and 0.14 for $\hat{f}\sigma_*$ and $\tilde{f}\sigma_*$. The offset was largest along the direction of Camera 2 in Snapshot 1. Interestingly, this particular camera direction was chosen, in part, because of the small amount of intervening dust. The strong offset is likely related to the dynamically extreme nature of this snapshot. For measurements that neglected dust attenuation, the mean offset was respectively -0.06 and -0.07 for $\hat{f}\sigma_*$ and $\tilde{f}\sigma_*$.

The mean fractional offsets presented in the previous paragraph were computed using a very broad variety of snapshots. If we limit the sample to dynamically passive (i.e., non-merging) systems by removing snapshots 1–4 from the analysis, the fractional offsets of $\hat{f}\sigma_*$ become 0.12 and -0.14 for dusty and dustless systems, respectively. The corresponding fractional offsets of $\tilde{f}\sigma_*$ become 0.04 and -0.15.

Many of the individual offsets exceeded the threshold set by the intrinsic measurement discrepancy. The mean offsets typically exceeded the threshold as well. Two general trends were observed:

- Dust attenuation often caused $f\sigma_*$ to be elevated with respect to $m\sigma_*$.
- When dust attenuation was neglected, $f\sigma_*$ tended to be smaller than $m\sigma_*$.

Note that many more snapshots from a larger variety of simulations would be needed in order to compute robust values for these offsets. Also note that these offsets were observed in a set of galaxies with ongoing star formation. Consequently, the trends in the offset only strictly apply to systems with ongoing or recent star formation. The trends are discussed further in the following sections.

The reader may have noticed that the positive offset due to the presence of dust was smaller, on average, than the negative offset present when dust was ignored. This occurred even though the flux-weighted measurement technique had an intrinsic positive offset. We do not consider this to be a robustly-determined trend because the magnitude of the offset due to dust could easily depend upon the amount of gas and dust present in the simulation snapshot. The magnitude may also depend upon the type of dust present in the system or upon the resolution of the underlying simulation. Using our limited sample, we can only determine very general trends, such as the sign of the offsets, with confidence.

4.3.4 Dust Attenuation

There were exceptions to the two general trends described in Section 4.3.3. Some measurements of $f\sigma_*$ that included dust attenuation were negatively offset with respect to $m\sigma_*$ and some dust-free measurements of $f\sigma_*$ were positively offset with respect to $m\sigma_*$. These exceptions are clearly evident in Figure 4.12. In this section, we discuss the first type of exception. The second type is discussed in Section 4.3.5.

From the results of Chapter 3, we know that young stars in our simulations had lower $m\sigma_*$ than the older stars, on average. We also know that the presence of dust generally increased $f\sigma_*$, relative to $m\sigma_*$. Since (1) interstellar dust attenuates light, and (2) stars tend to be born in dusty environments, we conclude that dust preferentially obscured the dynamically cooler young stars. By reducing the flux received from young stars, dust caused $f\sigma_*$ to be positively

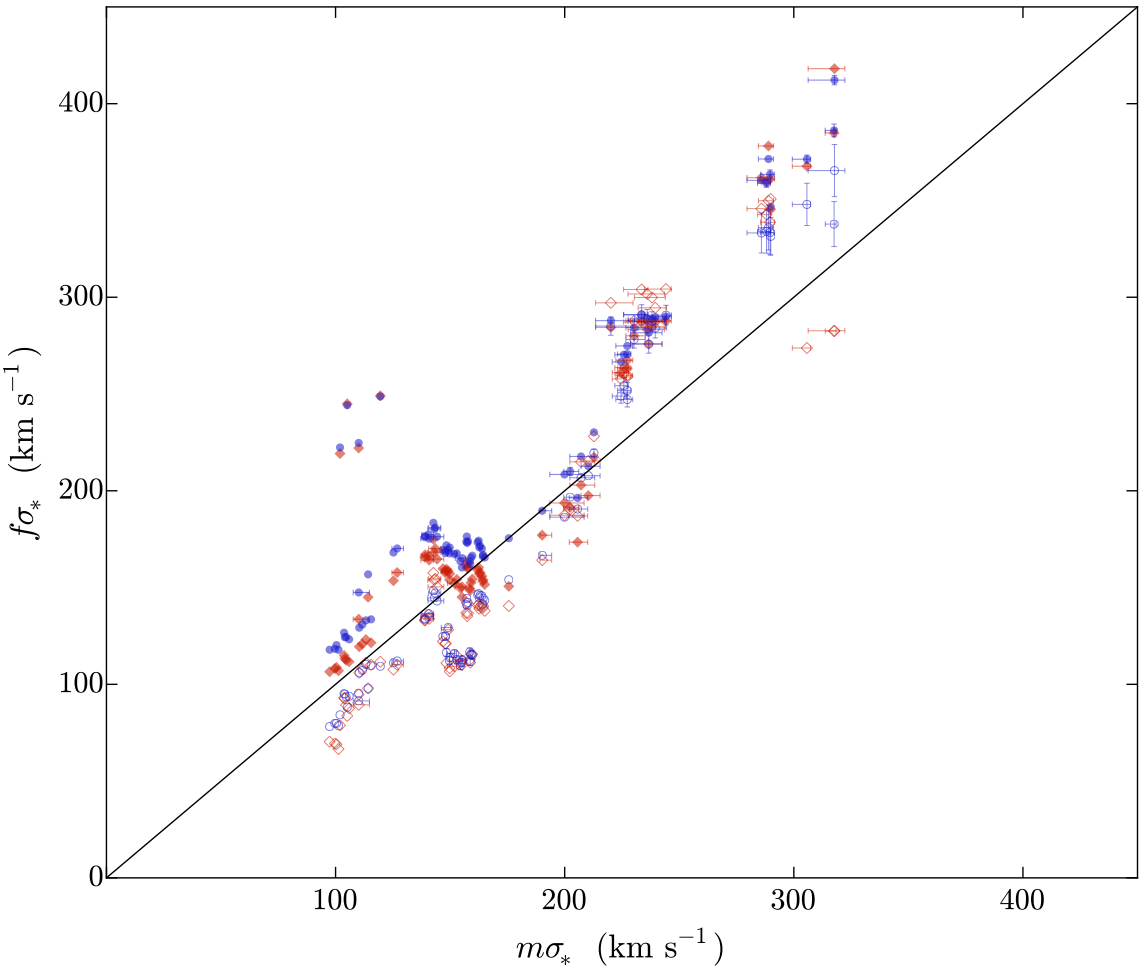

Figure 4.11: Flux-weighted versus mass-weighted velocity dispersion. The flux-weighted quantity tends to be positively offset with respect to the mass-weighted quantity when dust is included (solid circles and diamonds). The positive offset is accentuated when the LOSVD is assumed to be Gaussian (blue circles). On the other hand, when dust attenuation is not taken into account (open diamonds and circles), the flux-weighted quantity is negatively offset with respect to the mass-weighted quantity.

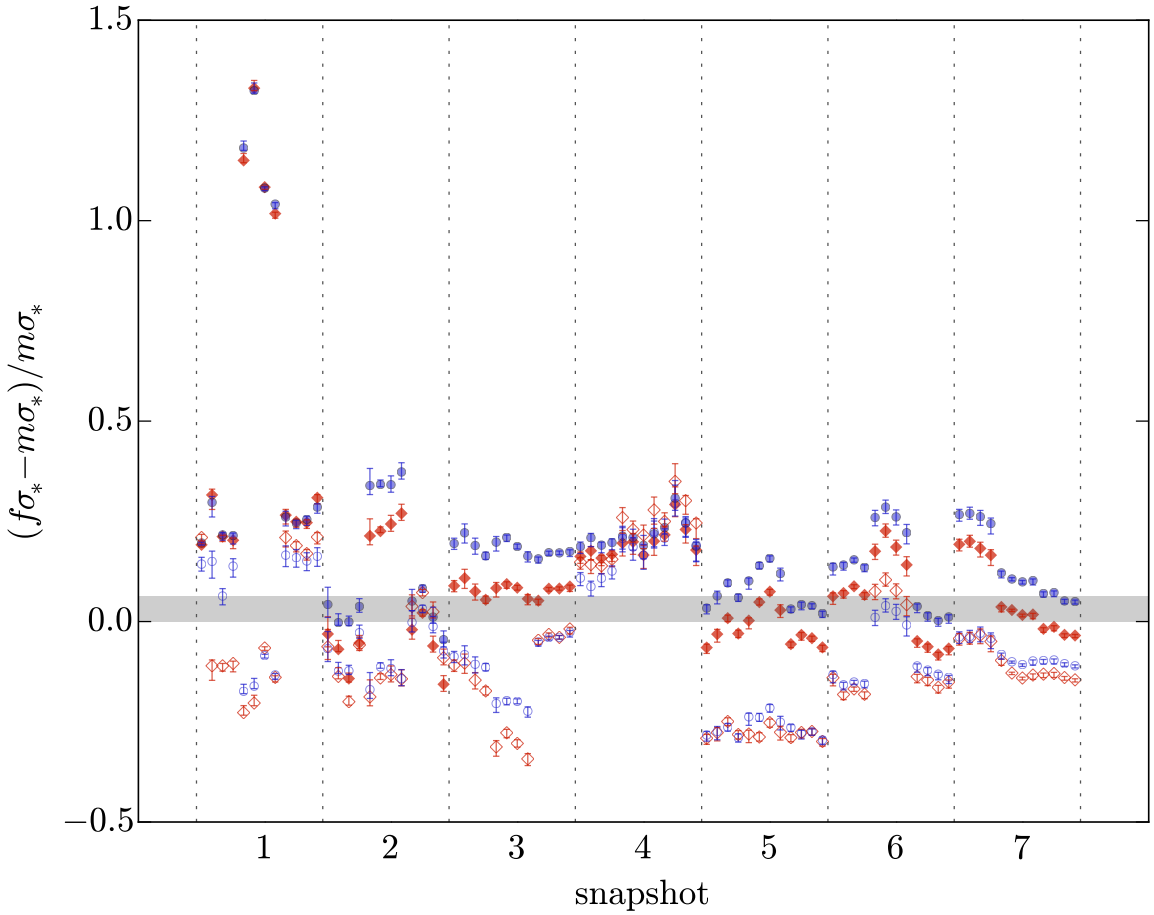

Figure 4.12: The fractional offset between flux-weighted and mass-weighted velocity dispersions. The shaded region indicates the range of offset values that may have been caused by the intrinsic discrepancy between the flux-weighted and mass-weighted measurement techniques. Only offsets falling outside of this region were considered significant. When dust was included, a significant positive offset was observed in a majority of the 84 measurement slits (62 $\hat{f}\sigma_*$ measurements and 45 $\tilde{f}\sigma_*$ measurements). A significant negative offset was seen in 1 measurement of $\hat{f}\sigma_*$ and 21 measurements of $\tilde{f}\sigma_*$. In the absence of dust, the offset was negative in the majority of measurements (58 $\hat{f}\sigma_*$ measurements and 60 $\tilde{f}\sigma_*$ measurements). The offset was positive for 18 of the dust-free measurements of $\hat{f}\sigma_*$ and 18 measurements of $\tilde{f}\sigma_*$.

offset with respect to $m\sigma_*$. In this scenario, outliers likely correspond to situations in which dust the dust did not strongly attenuate the light of young stars. There are three reasons this may have happened:

1. The overall degree of dust attenuation was low because the total amount of dust was small.

2. The dust was distributed in a thin sheet or disk; lines of sight nearly perpendicular to the disk experienced less attenuation because the optical depth was relatively shallow.

3. The dust became decoupled from the young stars due to a collision, heating, or winds.

In the first case, the *total* degree of dust attenuation would be low. In the second and third cases, the degree of attenuation may have been significant, but the light of young stars was not *preferentially* attenuated.

Since we obtained dust-attenuated and dust-free images for each camera direction, we were able to determine the level of attenuation in each slit. We define attenuation as,

$$\mathscr{A} = \log\left(\frac{F_{\rm tot}}{F_{\rm dust}}\right), \tag{4.7}$$

where $F_{\rm tot}$ is the total flux passing through the measurement slit when dust was ignored and $F_{\rm dust}$ is the flux received when dust was included in the SUNRISE analysis. The value of $\mathscr{A}$ for all measurement slits is presented in Figure 4.13. By comparing this figure with Figure 4.12, one can easily see that the total attenuation was not unusually low in situations for which dust-attenuated measurement of $f\sigma_*$ was negatively offset, relative to $m\sigma_*$. Furthermore, when the fractional offset is plotted as a function of attenuation, as in Figure 4.14, no clear relationship is evident; higher attenuation did not correlate with the fractional offset.

We are left to conclude that the distribution of dust with respect to the young stars was more important than the total amount of dust present in the simulations. This appears to be the case when comparing attenuated and unattenuated renderings of the systems. In Figures 4.2–4.8, it

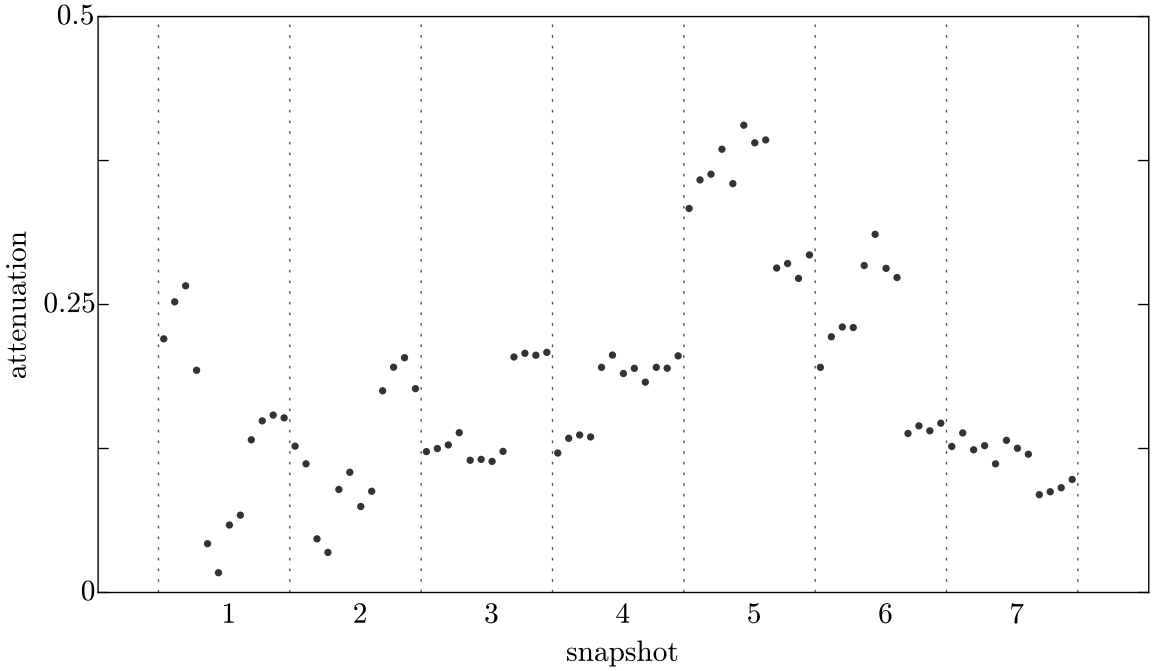

Figure 4.13: The attenuation, $\mathscr{A}$, for each measurement slit.

is clear that in most cases, dust and young stars occurred together (i.e., in the same region of the galaxy).

4.3.5 The $m\sigma_*$ of Young Stars

In this section, we investigate the exceptions to the second trend observed in Section 4.3.3. Specifically, these were cases in which the dust-free $f\sigma_*$ was positively offset with respect to $m\sigma_*$. In principle, the lower Υ (i.e., higher luminosity per unit mass) of the young stellar populations should cause any flux-weighted quantity to shift toward the characteristic value exhibited by the young populations (when dust attenuation is neglected). It is then reasonable to assume that the offsets observed in the dust-free $f\sigma_*$ measurements were due to offsets present in the population of young stars. Therefore, we measured the mass-weighted velocity dispersion using only the relatively young stellar populations in order to determine whether the observed offsets were due to the dynamics of the young stars.

In Figure 4.15, we show the fractional offset between the $m\sigma_*$ of stars less than 200 Myr

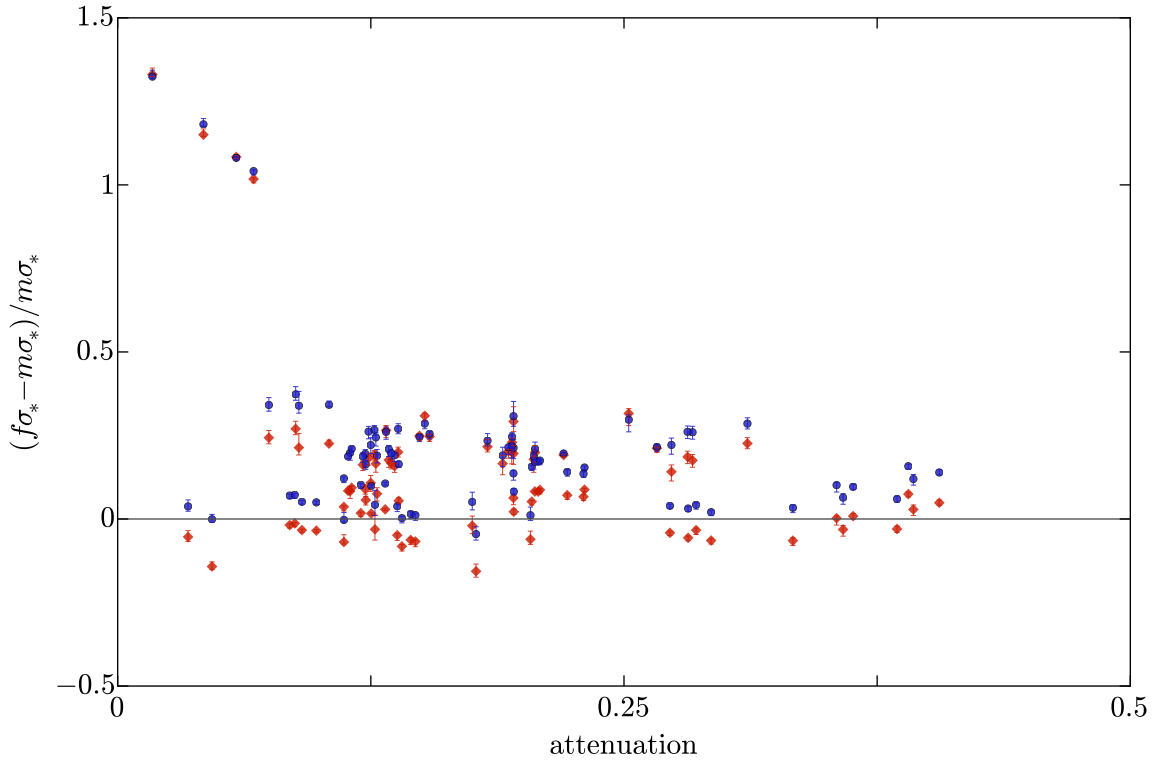

Figure 4.14: The fractional offset of $f\sigma_*$ with respect to $m\sigma_*$ versus attenuation, $\mathscr{A}$. It is clear that higher attenuation does not correlate with the offset.

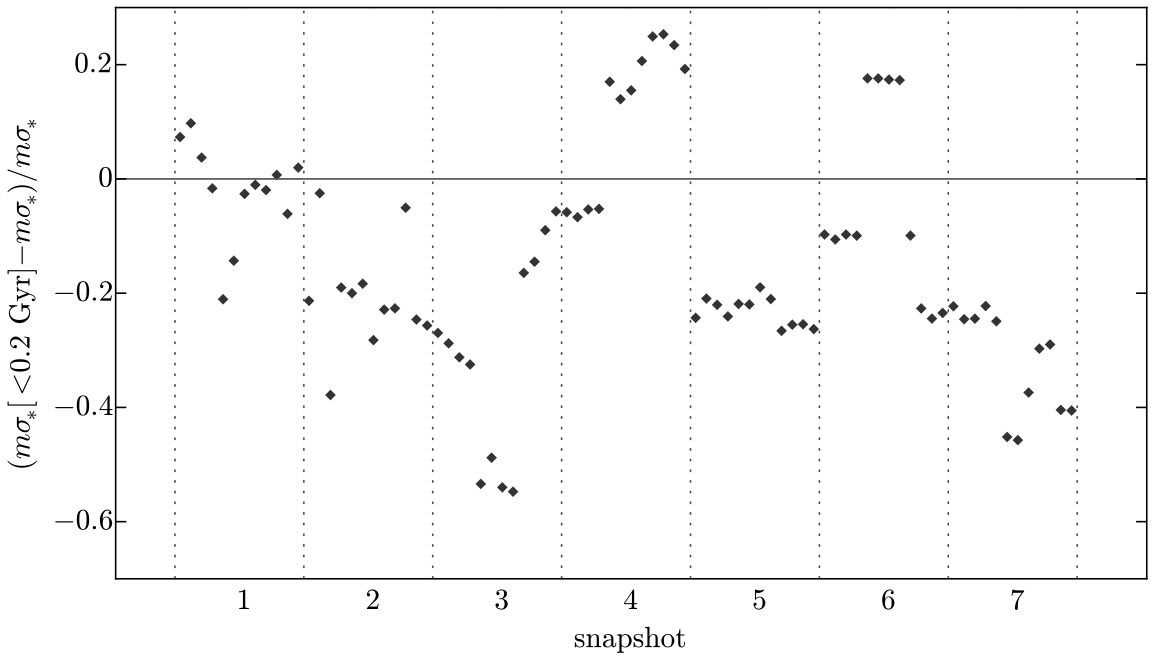

Figure 4.15: The fractional offset between $m\sigma_*$ of stars younger than 200 Myr, relative to the $m\sigma_*$ of all stars. The offset is positive in five of the observation directions (17 individual measurements).

old, relative to the global population. A positive offset was measured is 17 of the individual measurements. Comparing this plot with Figure 4.12, we see that most of the positively offset dust-free $f\sigma_*$ measurements can be easily explained; the measurements of $f\sigma_*$ were positively offset because the σ_* of young stars was elevated. Computing velocity $m\sigma_*$ in an appropriate stellar age bin (i.e., something other than 0–200 Myr) would likely explain the remaining positive offsets.

While young stars were dynamically cooler than the global population, *on average*, individual measurements of $m\sigma_*$ in the young population were able to exceed the global value. This occurred in dynamically peculiar situations (e.g., in snapshots 1 and 4, which were galactic collisions) and also when young stars were in a rotating disk, viewed edge-on (as in the case of Camera 2 of snapshot 6).

4.4 Discussion

We compared mass-weighted velocity dispersion measurements ($m\sigma_*$) with flux-weighted velocity dispersion measurements ($f\sigma_*$). The measurements of $f\sigma_*$ were performed by analyzing simulated spectra using the pPXF code of Cappellari (2012)—a code which is commonly used to measure velocity dispersions from real (i.e., observationally-obtained) spectra. Two spectra were obtained for each observation slit—one that included the effect of dust attenuation and one that ignored the presence of dust. All of our simulated spectra included the effect of stellar evolution. Our primary findings were:

1. Dust preferentially obscured the light of young stars because young stars were often found in dusty environments. Therefore, dust partially removed the dynamically cool young stars from the measurement of $f\sigma_*$, while stars of all ages contributed equally to the $m\sigma_*$ measurement. This caused measurements of $f\sigma_*$ to be elevated with respect to $m\sigma_*$ in most cases.

2. When dust was ignored, measurements of $f\sigma_*$ tended to fall below their $m\sigma_*$ counterparts. This was due to the higher luminosity-to-mass ratio (i.e., smaller Υ) of the young stellar populations, which weighted $f\sigma_*$ toward the velocity dispersion of the dynamically cooler young stars.

In exceptional cases, the dust-free measurements of $f\sigma_*$ exceeded $m\sigma_*$ and the dust-attenuated measurements of $f\sigma_*$ fell below $m\sigma_*$. The first type of exception occurred when the dynamics of the young stars were peculiar and also when the system was observed along a fortuitous line of sight that caused the velocity dispersion of the young population to appear elevated. The second type of exception occurred when the dust did not obscure the young stellar population more significantly than it obscured the older population. *We intentionally chose snapshots and viewing directions that we knew would increase the likelihood of finding such exceptional cases.*

We also found that the total degree of attenuation due to dust was not a good predictor of the offset between $f\sigma_*$ and $m\sigma_*$. Observations with significant dust attenuation often exhibited

a smaller offset due to dust than observations that suffered less attenuation. In other words, the distribution of the dust was more important than the total amount of dust present. Furthermore, recall that in Chapter 2, we found that the presence of a large attenuating slab resulted in measurements of $f\sigma_*$ that were lower than $m\sigma_*$ because the stars of highest dispersion (in the center of the galaxy) were the ones that were most attenuated. It is plausible that diffusely distributed dust has this effect, but we were unable to test the effect with the simulated observations described in this chapter. If this result from Chapter 2 is robust, then it would mean that the presence of dust simultaneously has opposing effects on measurements of $f\sigma_*$.

When comparing spectral modeling methods, we found that using a Gauss-Hermite series to model the LOSVD yielded lower values of $f\sigma_*$, on average, compared with a pure Gaussian LOSVD when dust was included in the measurement. There was no offset between the two methods when dust was ignored.

Finally, we note some important caveats to these findings:

- The numerical simulations that were used to create the galaxy snapshots were not perfect. Notably, the resolution limit was 25 pc, which means that the structure of the ISM was not resolved on scales of $\lesssim$25 pc. This also means that the particles in the simulation and the subsequent SUNRISE radiative transfer scheme represented entire stellar populations, with no sub-structure.

- We only simulated one small region of the spectrum (5040 Å to 5430 Å). The results may differ somewhat in different regions of the spectrum. On the other hand, this region is commonly used in real observations of velocity dispersion, so it is a useful choice.

- Changing the dust grain model, dust-to-metal ratio, or total gas dust in the systems would have likely effected the details of the results. The magnitudes of the offsets would likely be different if any of these parameters were changed, however the direction of each offset is likely insensitive to to these variables.

- Our observational sample was quite small and it was not randomly chosen. It included some snapshots with highly unusual dynamics and we chose several extreme viewing

directions. The extreme nature of the sample allowed us to identify exceptional cases which might not have been observed if the snapshots and viewing directions were chosen at random. However, one cannot compute robust statistics from this sample.

Chapter 5

Summary and Conclusions

Summary of Merger Evolution

I found that σ_* increases whenever two systems collide (i.e., pass though one another). The increase is most significant when the density of the system is maximized. This happens precisely at the moment during the collision when the nuclei of the progenitor systems are minimally separated. Furthermore, σ_* increases in *all* directions during collisions. The increase is most significant along the collision axis and least significant perpendicular to the collision axis. Upon receding from one another, σ_* in each progenitor quickly decreases and nearly returns to its pre-collision value. After passing through one another several times, the progenitor nuclei coalesce and σ_* fluctuates slightly around its final equilibrium value as the stars of the progenitor systems become more thoroughly mixed. These fluctuations occur less frequently and ultimately vanish as the system reaches dynamical equilibrium.

Dissipationless versus Dissipative Mergers

In Chapter 2, the evolution of velocity dispersion was analyzed in mergers of extremely simple spherically symmetric systems consisting only of stellar particles. The simulations of Chapter 3 consisted of much more realistic systems that contained gas, dark matter, star formation,

AGN feedback, and rotating disks. Despite the increase in complexity, I found that σ_* evolved similarly in both types of simulations.

Given these results, the question arises: why was the evolution of σ_* so similar in the dissipative and dissipationless mergers even though the simulations apparently differed significantly? The most likely answer is that the two sets of simulations *did not actually differ significantly*. A close inspection reveals that the the additional complexity in the simulations of Chapter 3 only directly effected the baryonic matter in the simulations. Baryonic matter (i.e., gas and stars) made up only 5% of the total mass in these simulations. The remainder of the mass was in the form of dark matter. The dark matter halos, in which the progenitor galaxies of Chapter 3 were embedded, consisted of dissipationless spherical distributions of particles that were quite similar to the systems examined in Chapter 2. Thus, the density and gravitational potential evolved similarly in both sets of simulations. Since σ_* responds to changes in gravitational potential, σ_* also evolved similarly in both types of simulations.

The primary difference between the two sets of simulations involved the formation of tidal dwarf galaxies. These small systems caused small periodic increases in σ_* as they passed through the nuclear region of their parent galaxy. Adding more gas to the progenitor galaxies generally increased the number of tidal dwarf systems, which added additional structure to the σ_* evolution time series.

Stellar Evolution and Flux-Weighted Velocity Dispersion

The stars in my dissipative simulations were born in a dynamically cool state, relative to the system as a whole, and gradually became heated with time. Upon comparing mass-weighted and flux-weighted measurements of σ_* in a diverse set of simulation snapshots, I found that the presence of dust tended to cause the flux-weighted σ_* to be elevated with respect to the mass-weighted σ_*. This happened because the dust preferentially obscured the dynamically cool young stars. I also found that the total degree of dust attenuation was not a good indicator of the discrepancy between the mass-weighted and flux-weighted measurements of σ_*. The distribution of the dust was far more important than the total amount of dust present.

Diagnostics and Scatter Statistics

I was able to identify general features that distinguish dynamically excited ongoing mergers from passively evolving systems. In Section 3.4.2, I provide statistical estimates for the scatter of σ_* in each of theses cases. The diagnostics and statistics are discussed further in Section 3.5.

Several of the diagnostic features were somewhat surprising. For instance, the presence of shells and other tidal debris in the outskirts of a system that has only one nucleus indicated that σ_* in the system had reached a stable value. The value of σ_* was also not unusually large in merging galaxies containing large tidal tails and bridges whenever the progenitor spheroids were significantly separated. The only situations for which measurements of σ_* yielded unusually large values, relative to the value of σ_* in the progenitors or the final remnant, occurred when two spheroids were significantly superimposed. In most of these cases, two (or more) distinct nuclei could be identified.

Limitations

The primary limitations of the work described in this dissertation are related to the small sample sizes used in the analyses and the coarse resolution of the simulations. Performing a larger set of simulations with a broader variety of initial conditions would have allowed me to compute more meaningful and robust statistics. By performing simulations with sub-parsec resolution, I could have examined the relationship between flux-weighted and mass-weighted velocity dispersion measurements with more realism, since the gas and stellar distributions would have been captured in more detail. The fact that the GADGET-3 evolves hydrodynamics using SPH, rather than a mesh-based method, also introduced uncertainty into the dust and young star distributions (see Hayward et al., 2013).

References

Barbanis, B. and Woltjer, L.: 1967, *ApJ* **150**, 461

Barnes, J. E.: 2002, *MNRAS* **333**, 481

Barnes, J. E. and Hernquist, L.: 1996, *ApJ* **471**, 115

Bender, R., Burstein, D., and Faber, S. M.: 1992, *ApJ* **399**, 462

Canalizo, G. and Stockton, A.: 2001, *ApJ* **555**, 719

Canalizo, G. and Stockton, A.: 2013, *ApJ* **772**, 132

Canalizo, G., Wold, M., Hiner, K. D., Lazarova, M., Lacy, M., and Aylor, K.: 2012, *ApJ* **760**, 38

Cappellari, M.: 2012, *pPXF: Penalized Pixel-Fitting stellar kinematics extraction*, Astrophysics Source Code Library

Cappellari, M. and Emsellem, E.: 2004, *Publications of the Astronomical Society of the Pacific* **116**, 138

Cox, T. J., Dutta, S. N., Di Matteo, T., Hernquist, L., Hopkins, P. F., Robertson, B., and Springel, V.: 2006a, *ApJ* **650**, 791

Cox, T. J., Jonsson, P., Primack, J. R., and Somerville, R. S.: 2006b, *MNRAS* **373**, 1013

Dabringhausen, J. and Kroupa, P.: 2013, *MNRAS* **429**, 1858

Dasyra, K. M., Tacconi, L. J., Davies, R. I., Naab, T., Genzel, R., Lutz, D., Sturm, E., Baker, A. J., Veilleux, S., Sanders, D. B., and Burkert, A.: 2006, *ApJ* **651**, 835

Davies, R. L., Burstein, D., Dressler, A., Faber, S. M., Lynden-Bell, D., Terlevich, R. J., and Wegner, G.: 1987, *ApJl Supp.* **64**, 581

Djorgovski, S. and Davis, M.: 1987, *ApJ* **313**, 59

Dopita, M. A., Groves, B. A., Fischera, J., Sutherland, R. S., Tuffs, R. J., Popescu, C. C., Kewley, L. J., Reuland, M., and Leitherer, C.: 2005, *ApJ* **619**, 755

Dressler, A., Lynden-Bell, D., Burstein, D., Davies, R. L., Faber, S. M., Terlevich, R., and Wegner, G.: 1987, *ApJ* **313**, 42

Elmegreen, B. G., Kaufman, M., and Thomasson, M.: 1993, *ApJ* **412**, 90

Engel, H., Davies, R. I., Genzel, R., Tacconi, L. J., Hicks, E. K. S., Sturm, E., Naab, T., Johansson, P. H., Karl, S. J., Max, C. E., Medling, A., and van der Werf, P. P.: 2010, *Astronomy and Astrophysics* **524**, A56

Escala, A., Larson, R. B., Coppi, P. S., and Mardones, D.: 2005, *ApJ* **630**, 152

Ferrarese, L. and Merritt, D.: 2000, *ApJl* **539**, L9

Funato, Y., Makino, J., and Ebisuzaki, T.: 1992a, *PASJ* **44**, 291

Funato, Y., Makino, J., and Ebisuzaki, T.: 1992b, *PASJ* **44**, 613

Gebhardt, K., Bender, R., Bower, G., Dressler, A., Faber, S. M., Filippenko, A. V., Green, R., Grillmair, C., Ho, L. C., Kormendy, J., Lauer, T. R., Magorrian, J., Pinkney, J., Richstone, D., and Tremaine, S.: 2000, *ApJl* **539**, L13

Genzel, R., Tacconi, L. J., Rigopoulou, D., Lutz, D., and Tecza, M.: 2001, *ApJ* **563**, 527

González-García, A. C. and van Albada, T. S.: 2005, *MNRAS* **361**, 1030

Gould, A. and Rix, H.-W.: 2000, *ApJl* **532**, L29

Groves, B., Dopita, M. A., Sutherland, R. S., Kewley, L. J., Fischera, J., Leitherer, C., Brandl, B., and van Breugel, W.: 2008, *ApJl Supp.* **176**, 438

Gültekin, K., Richstone, D. O., Gebhardt, K., Lauer, T. R., Tremaine, S., Aller, M. C., Bender, R., Dressler, A., Faber, S. M., Filippenko, A. V., Green, R., Ho, L. C., Kormendy, J., Magorrian, J., Pinkney, J., and Siopis, C.: 2009, *ApJ* **698**, 198

Hänninen, J. and Flynn, C.: 2002, *MNRAS* **337**, 731

Hayward, C. C., Torrey, P., Springel, V., Hernquist, L., and Vogelsberger, M.: 2013, *ArXiv e-prints*

Hernquist, L.: 1990, *ApJ* **356**, 359

Hiner, K. D., Canalizo, G., Wold, M., Brotherton, M. S., and Cales, S. L.: 2012, *ApJ* **756**, 162

Hopkins, P. F. and Hernquist, L.: 2009, *ApJ* **698**, 1550

Hopkins, P. F., Hernquist, L., Cox, T. J., Di Matteo, T., Robertson, B., and Springel, V.: 2006, *ApJl Supp.* **163**, 1

Jeans, J. H.: 1915, *MNRAS* **76**, 70

Johansson, P. H., Burkert, A., and Naab, T.: 2009, *ApJl* **707**, L184

Jonsson, P.: 2006, *MNRAS* **372**, 2

Jonsson, P., Groves, B. A., and Cox, T. J.: 2010, *MNRAS* **403**, 17

Jonsson, P. and Primack, J. R.: 2010, *Nature* **15**, 509

Kennicutt, Jr., R. C.: 1998, *ApJ* **498**, 541

Kroupa, P.: 2001, *MNRAS* **322**, 231

Leitherer, C., Schaerer, D., Goldader, J. D., González Delgado, R. M., Robert, C., Kune, D. F., de Mello, D. F., Devost, D., and Heckman, T. M.: 1999, *ApJl Supp.* **123**, 3

Lynden-Bell, D.: 1967, *MNRAS* **136**, 101

McConnell, N. J. and Ma, C.-P.: 2013, *ApJ* **764**, 184

Medling, A. M., Ammons, S. M., Max, C. E., Davies, R. I., Engel, H., and Canalizo, G.: 2011, *ApJ* **743**, 32

Merrall, T. E. C. and Henriksen, R. N.: 2003, *ApJ* **595**, 43

Nordström, B., Mayor, M., Andersen, J., Holmberg, J., Pont, F., Jørgensen, B. R., Olsen, E. H., Udry, S., and Mowlavi, N.: 2004, *Astronomy and Astrophysics* **418**, 989

Oliva, E., Origlia, L., Maiolino, R., and Moorwood, A. F. M.: 1999, *Astronomy and Astrophysics* **350**, 9

Quinn, T., Katz, N., Stadel, J., and Lake, G.: 1997, *ArXiv Astrophysics e-prints*

Robertson, B., Cox, T. J., Hernquist, L., Franx, M., Hopkins, P. F., Martini, P., and Springel, V.: 2006a, *ApJ* **641**, 21

Robertson, B., Hernquist, L., Cox, T. J., Di Matteo, T., Hopkins, P. F., Martini, P., and Springel, V.: 2006b, *ApJ* **641**, 90

Rothberg, B. and Fischer, J.: 2010, *ApJ* **712**, 318

Rothberg, B., Fischer, J., Rodrigues, M., and Sanders, D. B.: 2013, *ApJ* **767**, 72

Rothberg, B. and Joseph, R. D.: 2006, *The Astronomical Journal* **131**, 185

Salaris, M. and Cassisi, S.: 2006, *Evolution of Stars and Stellar Populations*, (Chichester: Wiley)

Saulder, C., Mieske, S., Zeilinger, W. W., and Chilingarian, I.: 2013, *Astronomy and Astrophysics* **557**, A21

Shier, L. M. and Fischer, J.: 1998, *ApJ* **497**, 163

Spitzer, Jr., L. and Schwarzschild, M.: 1951, *ApJ* **114**, 385

Spitzer, Jr., L. and Schwarzschild, M.: 1953, *ApJ* **118**, 106

Springel, V.: 2005, *MNRAS* **364**, 1105

Springel, V., Di Matteo, T., and Hernquist, L.: 2005, *MNRAS* **361**, 776

Springel, V. and Hernquist, L.: 2002, *MNRAS* **333**, 649

Springel, V. and Hernquist, L.: 2003, *MNRAS* **339**, 289

Tecza, M., Genzel, R., Tacconi, L. J., Anders, S., Tacconi-Garman, L. E., and Thatte, N.: 2000, *ApJ* **537**, 178

Tremaine, S., Gebhardt, K., Bender, R., Bower, G., Dressler, A., Faber, S. M., Filippenko, A. V., Green, R., Grillmair, C., Ho, L. C., Kormendy, J., Lauer, T. R., Magorrian, J., Pinkney, J., and Richstone, D.: 2002, *ApJ* **574**, 740

Treu, T., Malkan, M. A., and Blandford, R. D.: 2004, *ApJl* **615**, L97

Treu, T., Woo, J.-H., Malkan, M. A., and Blandford, R. D.: 2007, *ApJ* **667**, 117

Van Wassenhove, S., Volonteri, M., Mayer, L., Dotti, M., Bellovary, J., and Callegari, S.: 2012, *ApJl* **748**, L7

Villumsen, J. V.: 1982, *MNRAS* **199**, 493

Weingartner, J. C. and Draine, B. T.: 2001, *ApJ* **548**, 296

Wetzstein, M., Naab, T., and Burkert, A.: 2007, *MNRAS* **375**, 805

White, S. D. M. and Rees, M. J.: 1978, *MNRAS* **183**, 341

Woo, J., Treu, T., Malkan, M. A., and Blandford, R. D.: 2006, *ApJ* **645**, 900

Woo, J., Treu, T., Malkan, M. A., and Blandford, R. D.: 2008, *ApJ* **681**, 925

Woo, J.-H., Schulze, A., Park, D., Kang, W.-R., Kim, S. C., and Riechers, D. A.: 2013, *ApJ* **772**, 49

Woo, J.-H., Urry, C. M., Lira, P., van der Marel, R. P., and Maza, J.: 2004, *ApJ* **617**, 903

Appendix

A1 Analytic Results

The mass-weighted mean value of the radial velocity dispersion in a region of volume V is given by

$$m\sigma_* = \sqrt{m\sigma_{\rm r}^2} \tag{5.1}$$

with

$$m\sigma_{\rm r}^2 = \frac{1}{M_V}\int_V \langle v_{\rm r}^2\rangle \rho \, dV \tag{5.2}$$

where M_V is the mass within the volume V, ρ is the mass density, and $\langle v_{\rm r}^2\rangle = \langle(\hat{\mathbf{r}}\cdot\mathbf{v}_{\rm cm})^2\rangle$ is the mean squared radial component of the velocity with respect to the center of mass of the system (i.e., the velocity in the zero momentum frame). For a spherically symmetric system, this can be written in terms of r, as

$$\sigma_{\rm r}^2(r) = \frac{4\pi}{M(r)}\int_0^r \langle v_{\rm r}^2\rangle \rho(r') r'^2 \, dr' \tag{5.3}$$

where $M(r)$ is the mass enclosed within radius r. A system having an isotropic velocity dispersion tensor throughout will, by definition, have the same velocity dispersion in all directions at any arbitrary position $\mathbf{r}$ within the system. Thus, for an *isotropic* system, we could measure the velocity dispersion along *any* direction, compute the mass-weighted mean, and arrive at the same result for $m\sigma_*$. In particular, if we choose the line-of-sight direction, $\hat{\mathbf{n}}$, then $\langle v_{\rm n}^2\rangle = \langle(\hat{\mathbf{n}}\cdot\mathbf{v}_{\rm cm})^2\rangle = \langle(\hat{\mathbf{r}}\cdot\mathbf{v}_{\rm cm})^2\rangle = \langle v_{\rm r}^2\rangle$. An expression for $\langle v_{\rm r}^2\rangle$ in an isotropic, non-rotating

Hernquist profile is given in Hernquist (1990) and reproduced below:

$$\langle v_{\rm r}^2 \rangle = \frac{GM}{12D} \left\{ \frac{12r(r+D)^3}{D^4} \ln\left(\frac{r+D}{r}\right) - \frac{r}{r+D}\left[25 + 52\frac{r}{D} + 42\left(\frac{r}{D}\right)^2 + 12\left(\frac{r}{D}\right)^3\right]\right\} \quad (5.4)$$

Adopting a system of units in which $G = D = M = 1$, (5.4) becomes

$$\langle v_{\rm r}^2 \rangle = r(r+1)^3 \left[\ln\left(1 + r^{-1}\right) - \frac{25 + 52r + 42r^2 + 12r^3}{12(r+1)^4}\right] \quad (5.5)$$

In these units, $1\, r_{\rm h} = 1 + \sqrt{2}$ and

$$1\, \frac{r_{\rm h}}{t_{\rm dyn}} = \sqrt{\frac{2}{\pi^2(1+\sqrt{2})}} \quad (5.6)$$

Upon substituting (5.5) into (5.3) with $r = r_{\rm h}$, evaluating the integral, computing the square root, and using (5.6) to express the result in terms of $r_{\rm h}$ and $t_{\rm dyn}$, we arrive at the result,

$$m\sigma_* \approx 1.0035 \frac{r_{\rm h}}{t_{\rm dyn}} \quad (5.7)$$

Substituting $r = r_{\rm h}/2$ yields

$$m\sigma_* \approx 1.0693 \frac{r_{\rm h}}{t_{\rm dyn}} \quad (5.8)$$

A2 Computer Hardware

In order to perform the SUNRISE analysis, I needed a computer with a large amount of shared memory—in excess of 32 GB. At the time that the project began (December, 2010), the only affordable computer motherboards that supported more than 32 GB of random access memory were server motherboards, built for Intel and AMD x86-64 CPUs. I built a machine using the following hardware.

Motherboard: Asus KGPE-D16 Dual Socket G34 AMD SR5690 SSI EEB 3.61

Processors: 2x AMD Opteron 6172 Magny-Cours 2.1 GHz (24 cores total)

Memory: 16x 4 GB DDR3 1333 unregistered DRAM (64 GB total)

Graphics: EVGA Nvidia GeForce GTX 580 (containing 512 CUDA cores and 1.5 GB GDDR5)

System disk: 64 GB Crucial RealSSD C300

Data disks: 2x 1.0 TB Western Digital Caviar Black WD1002FAEX

Chassis: Intel 5U Server Chassis SC5650WSNA, with 1000W PSU

These particular CPUs from Advanced Micro Devices (AMD) were chosen because they were more affordable than the equivalent Intel Xeons that were available at the time. The CPUs also allowed me to use a large quantity inexpensive unregistered DRAM modules, rather than registered modules. The GeForce GTX 580 graphics processing unit was used to accelerate SUNRISE runs that computed dust emission. These runs were not included in the final analysis of Chapter 2 because thermal emission was ultimately not needed.

In addition to running the SUNRISE analysis, the simulations of Chapter 2 were performed on this machine. The machine was also used to perform a small portion of the GADGET-3 simulations as well as most of the velocity dispersion analysis of Chapter 3.